Department of Physics and Astronomy

Concentrating Solar Thermal storage using metal hydride: Study of destabilised calcium hydrides

Arnaud Camille Maurice GRIFFOND

This thesis is presented for the Degree of Doctor of Philosophy of Curtin University

July 2019

To the best of my knowledge and belief this thesis contains no material previously published by any other person except where due acknowledgement has been made. This thesis contains no material which has been accepted for the award of any other degree.

Arnaud Camille Maurice GRIFFOND

Abstract

In order to solve the impending energy crisis, Concentrating Solar Thermal (CST) is fast becoming a prominent method to generate renewable energy.[1] Energy storage is the "Achilles' heel" for the development of renewable energy. Indeed, to counteract the existing mismatch between the discontinuous solar energy supply and electricity consumption, the implementation of thermal energy storage (TES) systems into CST plants has become essential. Cost competitive energy storage solutions are required to overcome the problem due to the intermittence of energy production.

Thermal Energy Storage for CST is a technology using heat as a medium to store solar energy. The heat is then used to generate electricity via a turbine during the night time or during low energy production periods. The cost of solar thermal heat storage is a critical factor in its future deployment and there are two strategies for reducing its costs:[2]

- Utilising higher energy density storage materials to reduce the volume and mass of the material required.
- Utilising higher energy storage temperature to increase the overall heat to electricity conversion efficiency.

Molten salts as TES are used for the first generation of heat storage medium, but their low heat storage capacity result in a large volume and cost of material required. Research into improving CST continues to focus heavily on the improvement of TES systems. Molten salt systems are in commercial use in Spain and the United States by utilising the sensible heat storage of these materials. Alternatives solutions to molten salt storage are under development such as latent heat storage materials through taking advantage of phase change enthalpy of materials. Furthermore, a more promising technology is to utilise the reversible thermochemical reaction of metal hydride materials. Theoretically, the gravimetric heat capacity of a metal hydride TES may be up to 55 times higher than molten salts.

Reversible thermochemical reactions involve the use of the reaction enthalpy between two materials by changing the temperature or pressure of the system. Metal hydrides are of particular interest as thermochemical materials for their high reaction enthalpy during hydrogen absorption and desorption. During the daytime, a thermochemical release of hydrogen from the material occurs by absorption of heat (endothermic reaction). At night the reversible absorption of hydrogen releases heat (exothermic reaction) that is available for power generation.

Calcium hydride has a favourable energy density i.e. has a good potential for TES application. Its abundance and the relatively low cost to synthesise calcium hydride makes it an interesting candidate. Unfortunately, its desorption temperature is too high, and calcium is corrosive at high temperature for both current and proposed next-generation CST plants.

By adding metallic elements or alloys (*M*) to calcium hydride, the pathway of desorption may be altered from eq. 1 to eq. 2. In this situation, the Gibbs free energy of reaction decreases with a concomitant decrease in the temperature of desorption. This process is known as **thermodynamic destabilisation**.[3] This idea and the purpose of this solution is developed in Chapter 1. Through a combination of manual and computer assisted thermodynamic calculations, several low-cost candidates with the most promising CaH_2 destabilisation reactions and operating temperatures for the next generation of CST have been identified.

$$CaH_2 \rightleftarrows Ca + H_2 \qquad (1)$$

$$xCaH_2 + yM \rightleftarrows Ca_xM_y + xH_2 \qquad (2)$$

This research project aims to develop the knowledge base of energy storage, leading to a state of art of renewable energy research portfolio based on destabilised calcium hydride-based systems. Heat storage using metal hydrides has been explored since the 1970's, but was generally applied to temperature below 200 °C due to the nature of the hydrides developed at that time.

The second generation of TES for CST recommended by the Sunshot vision[2] aims a working temperature between 600 °C and 800 °C, and a cost of energy store of 15 US$.kg^{-1}. Chapter 1 highlights the objectives of this project and present the thesis outlines.

All the equipment and the technology used for this study are described in chapter 2. In order to analyse the desorption process, thermal analysis (Differential Scanning Calorimetry (DSC), Thermo-Gravimetric Analysis (TGA), Mass Spectrometry (MS) and Simultaneous Thermal Analysis (STA)), *ex-situ* and *in-situ* synchrotron X-ray powder analysis and sorption analysis (Temperature Pressure Decomposition (TPD), Pressure Composition Isothermal (PCI)) were used. Thermal analysis helped to analyse the heat exchange during the reactions. The path of reaction and the different phases formed during the reaction process is detected using *in-situ* synchrotron X-ray analysis. In order to conduct a sorption analysis, a sample cell reactor was adapted to the specific high temperature, and the details of this are also described in chapter 2.

This thesis consists of a systematic study of the destabilisation of calcium hydride with different potential elements or alloys using thermodynamic calculations. The costs are analysed in order to make CST energy competitive in the short and/or medium term. Gravimetric energy storage capacity

associated with the cost of the raw material for the High Temperature Metal Hydride (HTMH) are the key factors for competitiveness. Via thermodynamic calculation and costs analysis, three systems have been selected for an in-depth study of different desorption reaction analyses. The details of these calculations and results are exposed in chapter 3.

Three systems have been selected for experimental analysis and are xCaH$_2$ + ySi (Chapter 4), CaH$_2$ + 2C (Chapter 5) and CaH$_2$ + MgO (Chapter 6). Sorption analysis associated with thermal analysis have been done to identify the different steps of reactions. These results have been compared with the desorption process of a pure CaH$_2$ sample. Different samples of these compositions have been analysed by *in-situ* synchrotron X-ray analysis. The path of reaction has been determined by this analysis.

For example, on the xCaH$_2$ + ySi (Chapter 4), it has been observed that for a stoichiometry with a ratio of CaH$_2$/Si > 1, the desorption occurred in two specific steps (the first step is also divided into several steps). Below 600 °C, CaH$_2$ and Si reacts to form a mixture of CaSi, an unknown Ca$_x$Si$_y$, and CaH$_2$ left over. Then CaSi and CaH$_2$ reacts in a reversible process to form a Ca$_5$Si$_3$ phase releasing a minimum of 1.2 wt % of hydrogen at ≈ 700 °C Using a PCI experiment, an experimental enthalpy for this reaction could be estimated. This system shows similar results in gravimetric heat storage capacity to the CaH$_2$ + Al system; a gravimetric heat storage capacity between 660 kJ·kg^{-1} and 807 kJ·kg-^{1}, and a cost of energy store has been calculated which approach the Sunshot vision target.

The CaH$_2$ + 2C (Chapter 5) system has been studied using expanded natural graphite. Thermodynamics calculations showed promising energy storage capacity, but it has not been confirmed experimentally at this stage of the analysis. Using mass spectrometry analysis associated with TGA and DSC in a simultaneous thermal analysis showed the release of acetylene gas during the desorption process. Further investigations are required and specifics solutions are proposed.

The reaction between CaH$_2$ + MgO (Chapter 6) is the most interesting system at this stage. The literature has shown that CaO and MgH$_2$ can be use as starting material. Using CaO instead of CaH$_2$ lowers the price by a factor 20 (see chapter 3). This system requires extra care for the container due the volatility of magnesium gas at high temperature.[4] On the other hand, the sorption analysis shows promising results. A gravimetric heat capacity of 1910 KJ.kg^{-1} has been measured and a price of 1.6 US$.kWh^{-1} thermal stored has been estimated. The price does not include the engineering cost but is promising for TES applications. The Hydrogen Storage Research Group (HSRG) is working on the conception of a scaled-up system allowing to test up to 2 kg of the most promising candidate of metal hydride for TES. The point is to test hydrogen storage at a representative scale of a CST storage system using metal hydride.

Acknowledgment

First and foremost, my humble gratitude goes to my principal supervisor, Professor Craig Buckley for offering this great opportunity. I am grateful to Professor Craig Buckley and his wife, Mrs Jocelyn Buckley, for their warm welcome.

I wish to thank my co-supervisor, Dr Drew Sheppard for his guidance throughout the duration of this thesis. Thanks for his patience, motivation, immense knowledge and scientific ethic. You have taught me how to be a true scientist; questioning all results from all angles.

I would also like to thank the members of the Hydrogen Storage Research Group at Curtin University, my associate supervisor Dr. Terry Humphries, Dr. Mark Paskevicius, Dr. Vernonica Sofianos, Dr. Kevin Jarrett, Dr. Kasper Moeller, Dr. Dehua Dong for all the discussions both scientific and otherwise.

Thanks to all the Ph.D. student who I had the chance to share the office with. Enrico Ianni, you were a pleasant office mate. Mariana Tortoza, it was a pleasure to meet you, you are not only a nice office mate but also a great friend. Thanks to Marcela Montserrat Landero Figueroa, Arti Verma, Bec Wellard, Lucas Poupin, Tam T. Nguyen, Ali Alamri and all the Ph. D. students I had the pleasure to spend time with.

I would also like to acknowledge the facilities, scientific and technical assistance of the Australian Synchrotron and specifically Dr. Helen Brand and the Australian Microscopy & Microanalysis Research Facility at the Centre for Microscopy, Characterisation & Analysis at John de Laeter Research Center. I am specifically grateful to Veronica Avery for her assistance and Matthew Rowles for his expertise on X-ray analysis and crystallography.

I'd also like to thank all the staff in the Department of Physics and Astronomy who have helped me over the years. All my thoughts go to the families of Melat Habtemariam and Bruce Stansby.

I would like to acknowledge Prof. Kondo-Francois Aguey-Zinsou for his thermal analysis in an inert atmosphere at the University of New South Wales.

I also had the chance to visit the Helmhlotz-Zentrum Geesthacht thanks to Dr. Martin Dornheim and Dr. Anna-Lisa Chaudhary. I would like to thank Anna-Lisa Chaudhary for her welcome and professionalism during this visit.

A special thanks to Sophie Rivoirard. You gave me the passion to persevere in the field of science. I would also like to acknowledge Patricia De Rango for informing me of the existence of this project. I previously lived four wonderful years at the Neel institute at Grenoble in your company.

To my family; you have all been extremely supportive throughout this experience. A special mention goes to my wife, Andra-Ioana Griffond and, of course, my son, Bastian and my future little one; Emil. I love you all. Thank you for being who you are, encouraging me when I needed it most and being so adorable.

Finally, I would like to acknowledge the financial support of the Faculty of Science and Engineering for a Ph.D. scholarship to conduct this research, and the Australian Research Council (ARC) for ARC Linkage LP150100730: “Metal hydride reactors for high temperature thermochemical heat storage”, Chief Investigators: Buckley, Professor Craig E; Chandratilleke, Professor Tilak, Sheppard, Dr Drew, Davies, Dr Ian, Allen, Kenneth. LP150100730 provided funding for the consumables and equipment to conduct this research.

Statement of contribution of others

The content of Chapter 3, data collection and analysis, are my own work. The cost estimations have been done using the model developed by Dr. Drew Sheppard in D. A. Sheppard, C. Corgnale, B. Hardy, T. Motyka, R. Zidan, M. Paskevicius and C. E. Buckley, "Hydriding characteristics of $NaMgH_2F$ with preliminary technical and cost evaluation of magnesium-based metal hydride materials for concentrating solar power thermal storage", *RSC Advances*, 2014, **4**, 26552-26562. All the results of thermodynamic calculations and cost estimations have been crossed check and discussed with Drew Sheppard.

The content of Chapter 4, 5 and 6 are as yet unpublished. It is my own work. The sorption analyses and the *ex-situ* X-ray diffraction were carried out by me. The reactors for sorption experimentation at high temperature were designed, built and tested by me with the assistance of Drew Sheppard and Terry Humphries. The beam time project proposal, highlighting the scientific purpose of the experiment and its potential benefits and outcomes was prepared by me and submitted by Dr. Terry Humphries (Proposal 11988 – Humphries, Griffond, Rowles, Sheppard, Buckley, Sofianos). The proposal was awarded and these experiments and others were performed at the Australian Synchrotron Facility in Melbourne at the Powder Diffraction beamline by members of the Hydrogen Storage Research Group; Dr. Terry Humphries, Dr. Mark Paskevicius, Dr. Veronica Sofianos, Dr. Matthew Rowles, Lucas Poupin, Julianne Bird with the assistance of Dr. Helen Brand. Thermal characterisations were done at the Institute of Materials Research at Helmholtz-Zentrum Geesthacht (HZG) in Germany. The analysis was completed by Dr. Veronica Sofianos and I during a trip to Germany with the assistance of Dr. Anna-Lisa Chaudhary. For complementary experiments, samples were sent to the University of New South Wales (UNSW) for simultaneous thermal analysis. DSC-TGA and Mass Spectrometry were run at the same time by Prof. Kondo-Francois Aguey-Zinsou. The analysis and discussion of the results were conducted under the supervision of Drew Sheppard, in particular, the sorption analysis using the permeability and solubility corrections model developed in D. A. Sheppard, M. Paskevicius, P. Javadian, I. J. Davies and C. E. Buckley, Methods for accurate high-temperature Sieverts-type hydrogen measurements of metal hydrides, Journal of Alloys and Compounds, 2019, 787, 1225-1237.

Arnaud Camille Maurice GRIFFOND Professor Craig Buckley

Table of content

List of figures

List of tables

1. Introduction

1.1. Energy in the world

The world has enjoyed significant economic development for more than a century.[1] Industrial development, the increase in the number of cars and the proliferation of domestic equipment have led to significant growth in energy demand. Unfortunately, this growth in demand has been largely covered using fossil fuels, motivated by economic considerations. Other factors such as CO_2 emissions, the limited nature of our fossil reserves, and national energy independence came in second place. However, CO_2 emissions have been factored by several countries within their environmental policies over the past few years.

According to the IEA Global Energy & CO_2 Status Report 2017[5], global energy demand increased by 2.1 % in 2017, compared to 0.9% the previous year and 0.9% on average over the previous five years. 72 % of the rise was met by fossil fuels, a quarter by renewables and the remainder by nuclear energy. Last year's growth came after three years of flat emissions and contrasts with the sharp reduction needed to meet the goals of the Paris Agreement on climate change.[1]

An energy mix of fossil fuel, nuclear power with an increasing amount of renewable energy and reducing the fossil fuel is the predominant short-term solution to face the 2 °C limit of global warming fixed by the COP 21 Paris summit. Renewable energy has grown rapidly in recent years and is expected to increase by more than one third by 2022. According to Abbot,[1] the solar-hydrogen economy is the most scalable long term solution. Notably, Concentrating Solar Thermal (CST) energy is promising because of its high efficiency. To counteract the existing mismatch between the discontinuous solar energy supply and electricity consumption, the implementation of energy storage systems has become compulsory. But energy storage has always been the weakness for renewable energy development. The solution being pursued within the Hydrogen Storage Research Group (HSRG) is to use metal hydrides to store and release on demand the energy produced by a CST plant. In fact, hydrogen has already proven its potential for mobile application due to its high energy density.[6] The high storage density of hydrides associated with favourable sorption thermodynamics and kinetics as well as prolonged cyclability make hydrides ideal candidates for practical storage applications.

1.3. Solar energy & energy storage

The sunlight incidence on Earth, excluding the sunlight reflection back into space and the absorption by clouds, provides an average value of 85 PW. This value represents more than 5,000 times the actual annual energy power demand of the entire planet. That explains why solar is the top source of new power generating capacity, especially with photovoltaic supply.[7] There are two main techniques of converting solar energy into electricity: photovoltaic solar cells and concentrating solar thermal collectors.

1.3.1. Photovoltaic

Solar photovoltaic (PV) converts solar energy into electricity using photovoltaic cells. This technology is the one that has grown most rapidly in recent years. In the next few years PV will play an important role in the energy mix. Global market expansion has been due largely to the increasing competitiveness of solar PV combined with the rising demand for electricity in developing countries, as well as to the increasing awareness of solar PV's potential to alleviate pollution, reduce CO_2 emissions and provide energy access. The year 2017 was a landmark for solar photovoltaics (PV): it has been added more capacity from solar PV than from any other type of power generating technology in the world. More solar PV was installed than the net capacity additions of fossil fuels and nuclear power combined.[8] Furthermore, PV is a modular technology. It can be helpful in developing and emerging economies, as well as in isolated areas such as islands or isolated rural communities. However this technology shows sustainability weakness in the long term and at a large scale.[1]

Firstly, investigation to reduce the high quantity of energy required and the large water consumption during the manufacturing are essential for a bump in its deployment at a large scale.

Secondly, the efficiency of PV is by definition limited at 33 % efficiency.[9] Eventually it can be improved using a concentrator, but this technology is based on semi-conductor materials that are limited in terms of temperature range. Hence, a cooling system would be required. Thermodynamically, this solution will always be less efficient compared to a direct solar thermal solution.[10]

Finally, at the present time there is no suitable and sustainable large-scale solution to store electric energy. Rare earth materials or limited resource materials such as Lithium are needed to make batteries. Other storage options have been studied as pumped hydro storage with renewable energy[11]

or as flow batteries.[12] Each technology has some inherent limitations or disadvantages that make it practical or economical for only a limited range of applications. Thermal storage systems that utilise solar energy are thermodynamically the most efficient and effective means of storage as they use heat to produce electricity via a thermal energy conversion process similar to those used in conventional power plants.[13] Thermal energy storage (TES) is the most scalable solution because there are solutions using abundant materials that exclude limited resource materials such as as organic or rare earth elements.

1.3.2. Concentrating Solar Thermal & Thermal Energy Storage

On the other hand, Concentrating Solar Thermal or Power (CST or CSP) saw 100 MW of capacity come online in 2017 (2 GW of new plants are under construction[5]). It brings the global capacity to approximately 4.9 GW accompanied by an estimated 13 GWh of thermal energy storage (TES) across the world at the end of 2017 (Figure 1-1). 20 projects – including parabolic trough, tower and Fresnel facilities – with a combined capacity of 1 GW aiming for completion before the end of 2020. For example, two of the largest of these plants are in Morocco, where the 200 MW Noor II facility (7 hours; 1,400 MWh) commenced commissioning in 2018. The adjacent 150 MW Noor III plant (7 hours; 1,200 MWh) is at an advanced stage of construction. Once both plants are operational, Morocco's total capacity will exceed 0.5 GW. CSP developers have focused on TES as a key competitive advantage of CSP for providing competitively priced, dispatchable power. This focus has been driven by the increasing cost-competitiveness of solar PV compared to CSP without TES, but also by the emerging role of CSP with TES as a viable competitor with traditional (gas, coal and nuclear) thermal power plants. The principle of CST is to focus the sunlight with curved or oriented mirrors to a heat receiver target. Then, using a heat transfer fluid (HTF) the thermal energy is driven to run a steam turbine, which generates electricity. Due to the high temperatures, the steam is superheated and can efficiently run a turbine connected to a generator to produce electricity. [14,15, 16]

There are four main types of CST design:

Parabolic Trough consists of a line of concave mirrors that due to their parabolic shape focus the sun's rays onto a line in the centre of the parabola. Then, a HTF drives the energy to a power system.

Linear Fresnel lines are based on the same idea, but instead use a line of flat mirrors oriented to focus on an external line.

Power Tower is the system that shows the highest potential efficiency due to a higher operating temperature. A series of rotating flat mirrors are oriented to reflect the sunlight onto a receiver target placed on the tower. Focusing all the sun's beams onto one point produces a high operating temperature.

A Solar Dish Engine has the advantage of being the most modular technology. Using a parabolic mirror, the sunlight is focused on a target point to power an engine, like the Brayton engine, for example.

This technology, being a direct heat supply, has a higher potential efficiency than PV and is considered to be less sensitive to weather changes because of its superior capability of handling cloud transients. This drive to a higher capacity of generating power on a daily basis. Employing thermal energy storage (TES) can help smooth the energy production to fit with the energy demand. The idea of storing thermal energy offers a sustainable solution. Associating TES with CST is a recent technology that has only recently been introduced on the market. The current state of the art technology shows that the only other technology in use, the molten salt, can only store up to 7 hours when fully loaded.

Figure 1-1: CST Thermal Storage Global Capacity and Annual Addition, 2007-2017.[17]

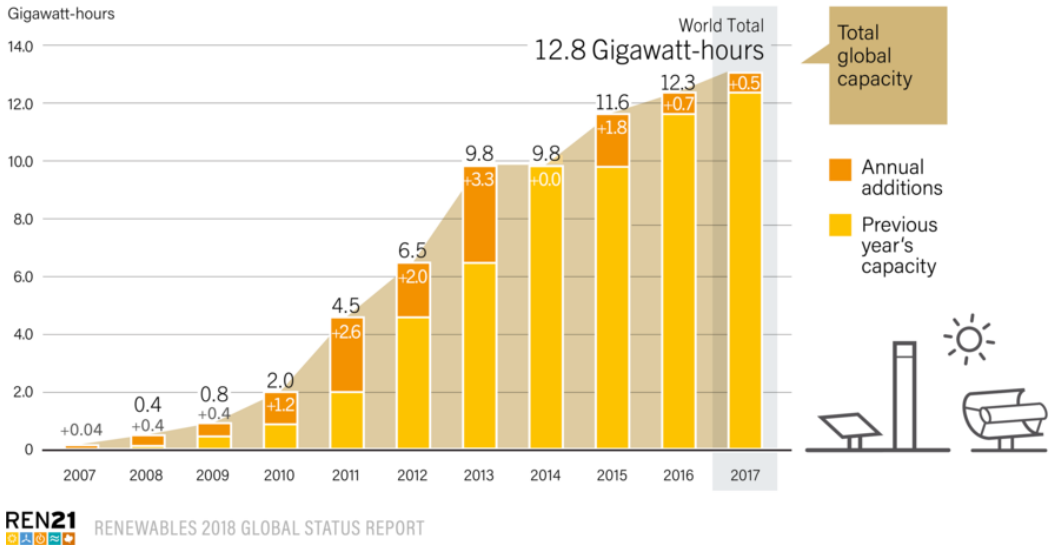

Based on the conclusion of the U.S. Department of Energy SunShot vision study[2], goals were set for the future research and applications of solar energy. For next generation of CST, an operating temperature between 600 °C and 800 °C is recommended. Indeed, Wentworth *et al.*[18] showed that the ideal thermochemical reaction extraction temperatures needed to be approximately 500 °C for a

conventional power plant, but closer to 800 °C if a Stirling cycle or Brayton cycle device is consider to be used. This infers that molten salt technology for HTF and TES application may become obsolete. Indeed, molten salts degrade above a temperature of approximately 595 °C.

The three methods of TES most documented are: (1) sensible heat of materials; (2) latent heat of melting and (3) reversible chemical reactions. The predominant one presently used is the sensible heat of materials (molten salts). These materials resist to temperature changes and can maintain a high operating temperature when the temperature falls. Heat is stored/released through a heat transfer medium. The two fundamental problems with this technology are the large quantity, volume and cost of molten salts required to store enough heat and the limited operating temperature. Alternatives are under development such as exploiting the phase transition energy of a material ("latent" heat). At isothermal conditions, the change of a substance from one phase to another involves energy consumption or energy release. The issue with this solution is low thermal conductivity, leading to inadequate heat transfer and the disadvantage of slow charging and discharging rates.[19]

A more promising technology is to use a reversible thermochemical reaction. A thermochemical reaction is energy demanding or, if reversible, energy producing. Several classes of materials are available including hydrides, carbonates, hydroxides and oxides. Thermochemical energy storage, especially metal hydrides, have high potential gravimetric capacity. Most metals can combine with hydrogen to form stable metal hydrides with favourably high dissociation temperatures. A comparison of the heat storage capacity in $kJ \cdot kg^{-1}$ (Figure 1-2) shows that metal hydrides have the highest storage capacity per kilogram. Some metal hydrides, such as CaH_2 have the potential to store 28 times the energy stored by molten salts. A key point to improve the competitiveness of CST technology is to reduce the price of the TES. Indeed, TES represent ≈ 10 % of the total price of a CST plant. The high gravimetric storage capacity of thermochemical energy results in the potential for cost reduction because it maximises the quantity of material needed to store a large quantity of energy. A study lead by Sheppard *et al.*[8] conducted a cost analysis to confirm this point.

Figure 1-2: Gravimetric heat storage capacity of metal hydrides compared to molten salts and Thermochemical reactions.[20]

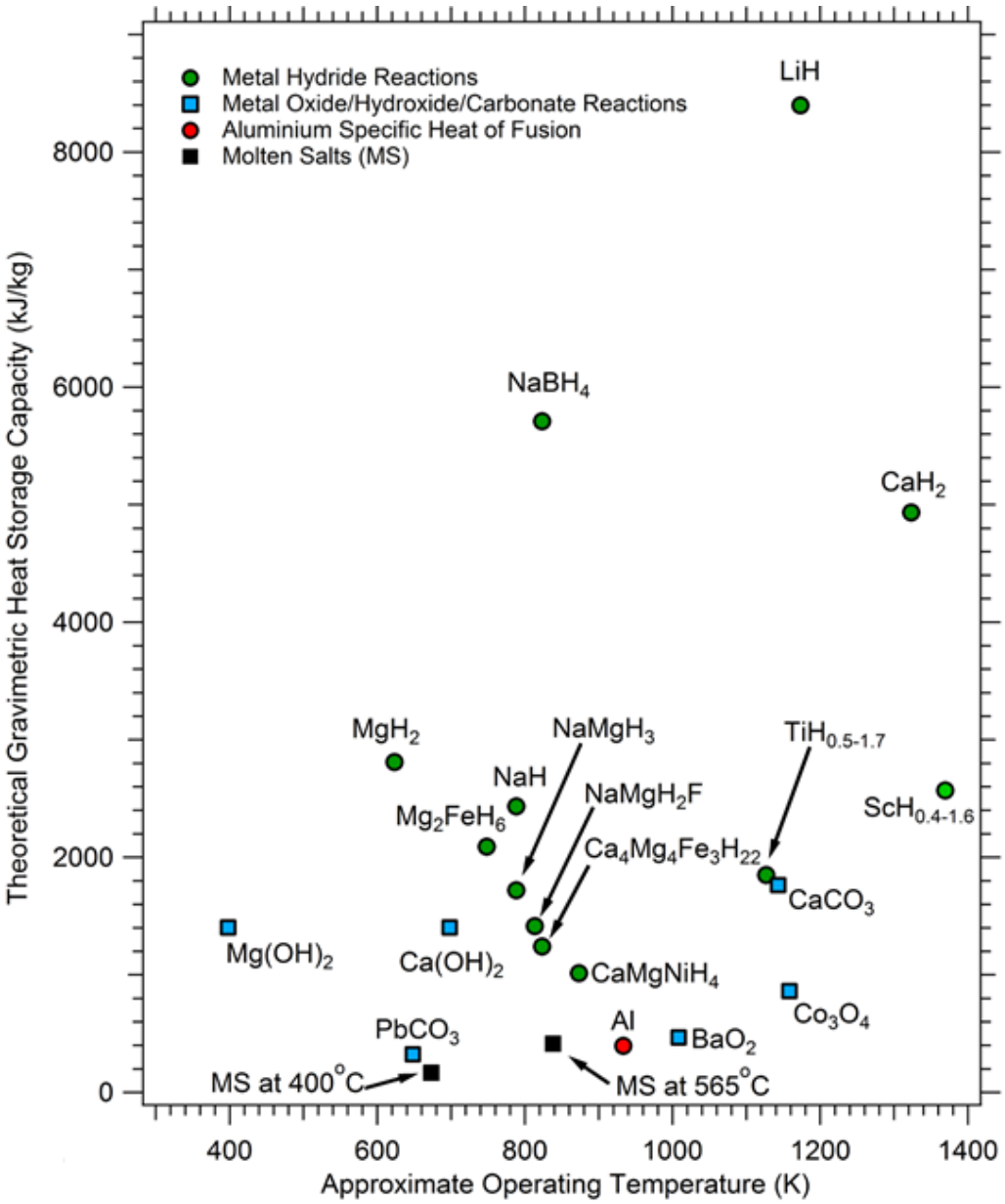

1.4. Thermal Energy storage using metal hydrides

The idea behind the solution being pursued within the Hydrogen Storage Research Group (HSRG) is to use high-temperature metal hydrides (HTMH) for the thermochemical reaction combined with a hydrogen storage container to store energy and release it on demand. Two options are considered for the hydrogen storage container; a Low-Temperature Metal Hydride (LTMH)[21, 22] or a gas tank

container. The HSRG works in collaboration with Savannah's River National Laboratories (SRNL) on cost calculation on paired HTMH-LTMH technology to decide on the favourable technology to adopt.[23]

The temperature change can make HTMH to either absorb hydrogen, releasing heat (exothermic reaction) or desorb, absorbing heat (endothermic reaction).The principle is schematically shown in Figure 1-3-a. It can be described in 2 steps:

a) Day Time: during sun light, as the temperature of the high-temperature reactor increases, the HTMH starts to dissociate and the hydrogen pressure increases. This causes hydrogen gas to move out of the reactor vessel and into the hydrogen storage container (Figure 1-3-a). This hydrogen desorption reaction is endothermic.

b) Night time: the HTMH temperature drops below the equilibrium temperature. Hydrogen moves back into the high-temperature hydride, where the exothermic hydrogen absorption occurs releasing heat (Figure 1-3-b).

Figure 1-3: Schematic day & night cycle of a Concentrating Solar Power coupled with a Thermal Energy storage using metal hydrides.

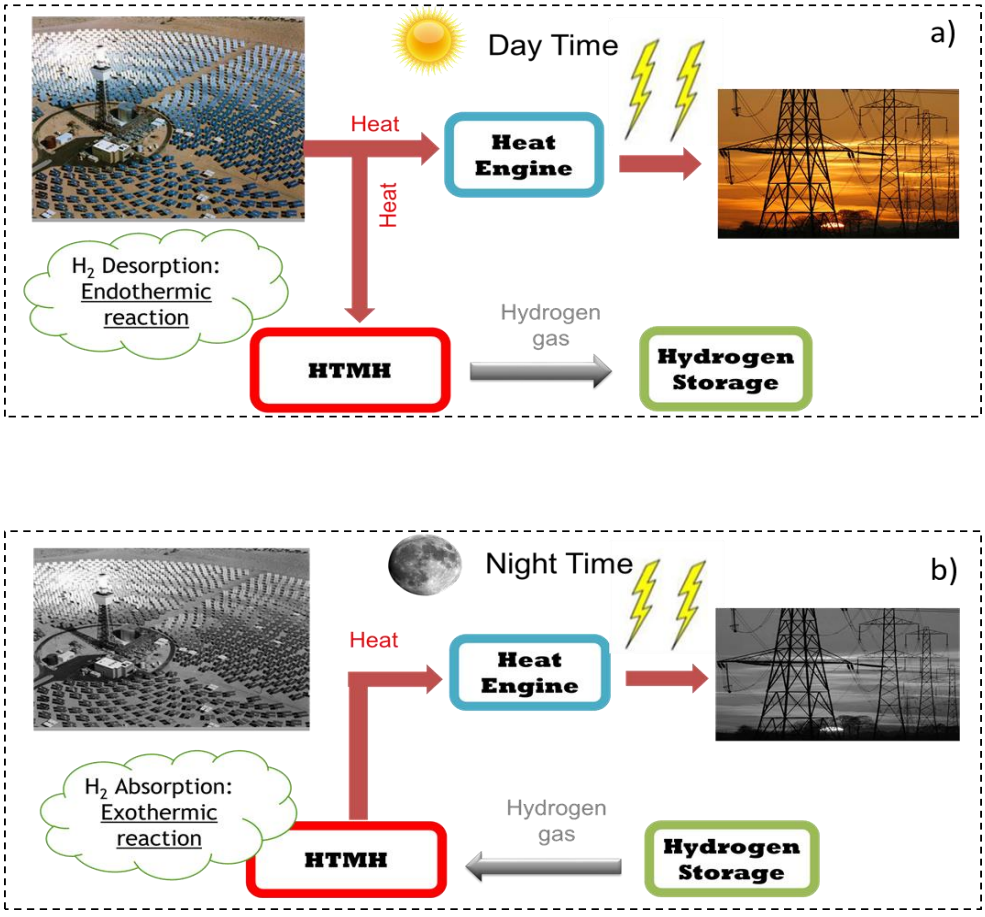

As showed on Figure 1-2, several metal hydrides have been studied for application as TES materials. Contrary to usual research for metal hydrides, the most interesting candidates are the ones that have a high temperature of reaction and hence a high enthalpy of reaction. Several research studies show interesting potential candidates.[24,25]

Actually, several transition metals and their intermetallic alloys can react with hydrogen to form hydrides. Molecular hydrogen is dissociated at the surface of a metal with the subsequent hydrogen ions diffusing into the bulk of the material. The absorption/desorption process can be described by Pressure-Composition-Temperature (PCT) graphs (see Figure 1-4). Upon entering the metal, the resulting hydrogen atoms occupy one or more of the available interstitial's sites in the metal lattice. Hydrogen is absorbed by the metal and forms a solid solution, known as the α-phase (linear part between point (a) and (b)), with an associated expansion of the metal lattice. The PCT graph plots the amount of hydrogen absorbed (hydrogen to metal ratio, H/M) at a given pressure and temperature. As the hydrogen to metal ratio increases, the metal hydride phase begins to form a hydrided metal phase (β-phase). While the α−phase and β-phase co-exist (between point (b) and (c)), there is a plateau in the isotherm and the length of this plateau determines the quantity of hydrogen stored. The absorption process is exothermic whereas the desorption process is endothermic. Completion of the β-phase is associated with a steep rise in the equilibrium pressure (beyond point (c)). The formation of the metal hydride phase is a thermochemical reaction. Thermodynamic properties (ΔH and ΔS, see chapter 3) of this reaction can be experimentally determined from hydrogen sorption measurements. If the hydrogen equilibrium pressure (between point (a) and (b)) is measured for a given material at various temperatures, then ΔH and ΔS can be determined. . This calculation is undertaken by means of a van't Hoff equation (equation 2-4 in section 2.5.1).Then, the gravimetric heat storage capacity can be calculated.

Figure 1-4: Example of Pressure Composition Temperature (PCT) Isotherm. Point (a) represents the beginning of the hydrogen absorption and the α-phase. Point (b) represents the beginning of formation of the β-phase The plateau represents the co-existence of the α and β-phase. Point (c) represents the beginning of pure β-phase.

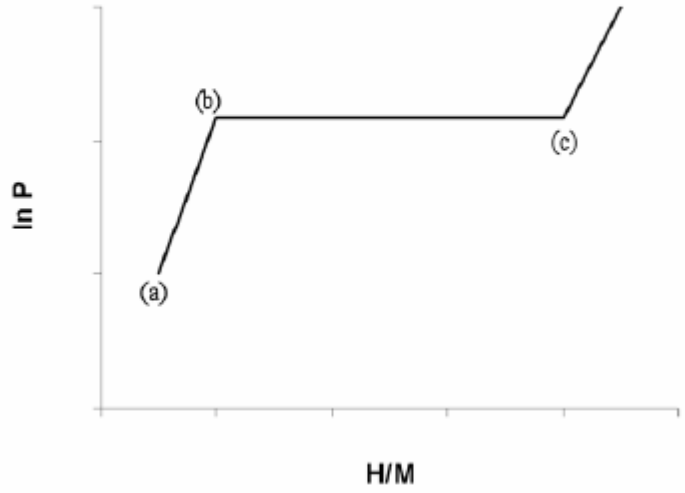

It is shown in Figure 1-2 that CaH_2 has the potential to be a TES material. Compared to other candidates such as LiH and $NaBH_4$, its price is lower by a factor of 5 to 25 times.[26, 27] The HSRG in collaboration with SRNL conducted a comparative cost calculation for different pairs of HTMH and LTMH for TES applications, where it was shown that CaH_2 paired with a TiFe LTMH was an excellent candidate.[23]

1.5. Destabilised CaH_2

CaH_2 is a stable hydride[27] with a 1 bar H_2 equilibrium pressure of ~1000 °C, due to its high reaction enthalpy (see section 3.3). The reaction between hydrogen and calcium has been known since the 1930's.[28] Since then, knowledge on the CaH_2 system has been gathered through several breakthroughs like the phase diagram of the Ca-CaH_2 system construction by Peterson *et al.*[29] and the thermodynamic enthalpy of decomposition calculation by Wang *et al*.[30]

$$Ca + H_2 \rightleftarrows CaH_2 + \Delta H_{abs}$$

Theoretical ΔH_{abs}= - 176 kJ.mol^{-1}. H_2

The CaH_2 theoretical hydrogen storage capacity is: H_2 wt % $= \frac{MM_{H_2}}{MM_{CaH_2}} = \frac{2.016}{42.096} = 4.8\ wt\ \%$

This results in a gravimetric heat storage capacity of 4180 kJ·kg^{-1}. However, the temperature of desorption is too high for CST applications. The Sunshot vision perceived an operating temperature higher than 600 °C but lower than 800 °C. Higher than 800 °C, engineering investment may be necessary for the containment materials. Furthermore, the melting point of pure Ca is 842 °C and CaH_2 is 890 °C[29, 31] and it has been shown that a calcium hydride mixture is corrosive above 800 °C, which may cause further engineering issues.[1]

By adding metallic elements or compounds to calcium hydrides, the reaction Gibbs free energy i.e. the operating temperature may decrease. Vajo *et al.*[3] has theorised on the destabilisation for metal hydrides. Thermodynamical destabilisation was initially determined to decrease the temperature at which H_2 is released from metal borohydrides with the goal of using them for hydrogen storage in cars. Destabilisation for metal hydrides (Figure 1-5) involves adding a second element or compound to a metal hydride to change the reaction pathway associated with H_2 release. Adding a well-chosen element to a HTMH reduces the hydrogen release reaction enthalpy and therefore the operating temperature.

Figure 1-5: Generalised enthalpy diagram illustrating destabilisation for calcium hydrides compounds.

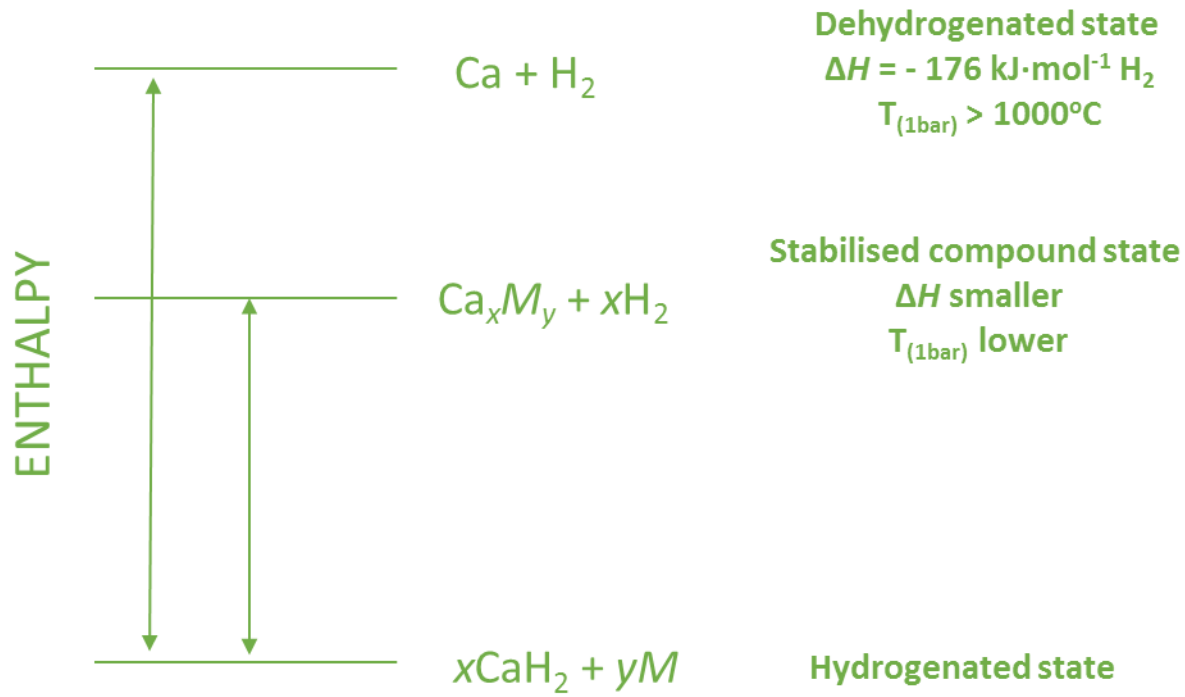

Efficiency of calcium hydride destabilisation has been proven by Veleckis *et al*. in 1980 for CaH_2 mixed with Al: [32]

$$CaH_2 + 4Al \rightleftarrows Al_4Ca + H_2;\ \Delta H \approx 83\ kJ{\cdot}mol^{-1}{\cdot}H_2,\ T_{1bar} \approx 414°C$$

$$2CaH_2 + Al_4Ca \rightleftarrows 2\ Al_2Ca + 2H_2;\ \Delta H \approx 90\ kJ{\cdot}mol^{-1}{\cdot}H_2,\ T_{1bar} \approx 481°C$$

In the Al-Ca case, destabilisation is "too efficient". The operating temperature at 1 bar equilibrium pressure is lower than the target range and the enthalpy of reaction is divided by 2. Using thermodynamic calculation program (HSC®), Dr. Drew Sheppard has identified several low cost candidates for destabilisation reactions of CaH_2 that have a 1 bar equilibrium temperature between 475 °C and 825 °C.[32-36] However, all these reactions have not been considered in the context of hydrogen storage in general or in the context of using the metal hydride reactions for thermal storage, as in all cases the reactions were merely a by-product of other research directions.

Knowing the high potential of CaH_2 and its low price, the idea of this project is to do a comprehensive literature review (binary phase diagrams of Ca-*M* systems) for potential destabilised calcium compounds and, with the assistance of a thermodynamic calculation, select candidates that have an operating temperature in the required temperature range.

1.6. Thesis outlines

The purpose of this research is to develop new TES systems for future CST plants, based on destabilised calcium hydride systems. The costs are analysed in order to make CST energy competitive in the short and/or medium term.

Gravimetric energy storage capacity associated with the cost of the raw material of the HTMH are the key factors for competitiveness. It is noted that the cost assessment from Sheppard *et al*.[24] stipulates that the hydrogen weight percent absorbed/desorbed by a reversible reaction has a large impact on the TES system cost. Indeed, the higher the quantity of hydrogen required, the higher the low-temperature hydrogen storage content required. Sheppard *et al*. demonstrated that in a paired HTMH-LTMH, the cost of the LTMH represents more than half of the total TES system cost.[24] Using thermodynamic calculations and the cost analysis, potential systems have been selected for operating in a temperature range between 600 °C and 800 °C at low pressure, and for an estimated total energy storage cost < 15US$·kWh^{-1}.

Three systems have been selected for experimental analysis. A brief introduction to the chapters and their contents are presented below. This thesis project is divided into the following steps and will be presented in this document as:

- Chapter 1: Introduction

- Chapter 2: Experimentations

  The different techniques used to synthesise and characterise the promising CaH_2 + *M* mixtures are presented. This includes ball-milling of reagents, X-ray diffraction (XRD) analysis on each sample to determine the phases and obtain their proportions. For each candidate mixture, measurement of their hydrogen properties such as thermodynamics and kinetics via pressure-composition-isotherms (PCI) and temperature programmed desorption (TPD) at temperatures between 600 °C and 800 °C are presented. For this type of measurement, a new reactor made of silicon carbide for high-temperature measurements was designed. The conception and the characteristics of this new reactor are described. Also, to have a comprehensive understanding of the path of reaction, thermal analysis was conducted in collaborative laboratories. Finally, in *situ* synchrotron measurements resulted in the full picture of the phase created during the desorption process throughout a temperature ramp.

- Chapter 3: Thermodynamic calculations and cost assessments

  Chronologically, the first step of this project research has been to conduct a literature review and thermodynamic study of the potential candidate for calcium hydride destabilisation. In order to select the promising candidates, the theoretical operating temperature, the enthalpy of reaction and the H_2 wt % released by the reaction were calculated. With these values an estimation of the economic viability of each system resulted and the most promising were selected. Three different systems were selected and are presented in the next 3 chapters.

- Chapter 4: The *x*CaH_2 + *y*Si system

  The *x*CaH_2 + *y*Si system. This system has the potential for sustainability and low-cost, since calcium and silicon are two of the most abundant elements in the earth's crust. This chapter shows that this is a complex system with a multistep reaction, which results in interesting characteristics for HTMH applications.

- Chapter 5: The CaH_2 + 2C system

  The CaH_2 + 2C system. This system has the highest gravimetric heat storage capacity. This system has one of the highest gravimetric heat storage capacity. The formation of CaC_2 based on the reaction between CaH_2 and C is known since the 1954.[37] The releasing of parasite gas as acetylene has been observed. This chapter illustrates a pre-study of this system using expanded natural graphite as reactant.

- Chapter 6: The CaH_2 + MgO system

  The interest for this system is that MgH_2 is well-known and well-studied in the hydrogen storage community, and the price of raw MgH_2 is low. The starting composition of CaO + MgH_2 must be a good option and may reduce the price of the calcium part by a factor of a least 25. On the other hand, Mg vaporise at high temperature due to its low vapour pressure.[4] A specific sealed container magnesium gas proof but hydrogen permeable was researched built and used.

A brief conclusion highlights the contribution of this thesis to the evolution of knowledge concerning destabilised calcium hydride system and describe the future development on the promising results obtain during those experiments in the perspective of application on the field.

2. Experimentation

2.1. Hydrogen Storage Research Group laboratory

The Hydrogen Storage Research Group (HSRG) constructed a new Hydrogen laboratory in 2015 in order to develop research on hydrogen storage under high pressure gas and high temperature conditions. These conditions require safety equipment such as adequate ventilation, gas detection, and storage with a limited access for highly flammable gas cylinders etc. Considering these elements, the laboratory has been designed using the following standards:

- *AS/NZS 2982 laboratory design and construction*
- *AS/NZS 2243 Safety in laboratories*
- *AS4332-2004 The storage and handling of gases in cylinders*
- *AS/NZS3000:2007 Electrical installations*
- *AS/NZS 60079 Part 10.1: Classification of areas — Explosive gas atmospheres*

Specific components of the laboratory abiding by these standards include:

- *ISO/DIS 15399 Gaseous hydrogen – Cylinders and tubes for stationary storage*
- *ISO/TR 15916 Basic considerations for the safety of hydrogen systems*

The HSRG laboratory is equipped with:

- 2 Gloveboxes furnished with vacuum pumps and Argon gas bottles supply in order to maintain a neutral atmosphere.
- 3 manual rigs including 1 high pressure (600 bar) rig. The rigs are composed of a platform with multiple valves, enclosing a calibrated reference volume and connecting it to a hydrogen gas bottle supply at one end and to a Sample Cell Reactor (SCR) at the other end. One of the rigs is equipped with a titanium-based AB_2-type metal hydride.[38] Using a hot air blower, the temperature of this metal hydride can be elevated up to its desorption conditions. This results in the possibility of supplying a higher pressure (up to 600 bar) than the hydrogen gas bottle (150 bar) line.
- 4 Computer-controlled rigs, 1 developed by PCT pro® company and 3 with a homemade LabVIEW® program developed by our team. This program operates the automatic temperature programmed desorption (TPD) and pressure composition isotherm (PCI) measurements (see section 2.5).

- Several furnaces capable of operating at up to 1100 °C with a programmable ramp and setting temperature.
- A Fritsch planetary ball milling machine with a ceramic, tungsten carbide or stainless-steel milling media, up to 500 rpm.

2.2. Sample preparation

According to theoretical predictions (see chapter 3), the promising stoichiometry of $x\mathrm{CaH_2} + yM$ (where M is destabilising additive) were synthesised by mechanical synthesis. This involves ball-milling of reagents. All handling of chemicals and sealable milling canisters was undertaken in an argon glovebox (mBraun, Germany) at less than 1 ppm H_2O and O_2. All samples were ball milled inside an Across International Planetary Ball Mill (PQ-N04) employing tempered steel vials and balls in an Ar atmosphere with a ratio 20:1 (6 mm Ø and 10 mm Ø ball size) for 3 h at 400 rpm with 35 cycles of 5 min clockwise followed by 5 min anticlockwise. Calcium was either hydrogenated to CaH_2 in the HSRG laboratory following the Bulanov *et al*.[39] synthesis method from Ca (99 %, Sigma Aldrich), or CaH_2 was purchased from Sigma Aldrich® (95 % pure). X-Ray Diffraction (XRD) analysis was conducted on each sample to determine the phases and their proportions.

2.3. *Ex situ* & *In situ* synchrotron Powder Diffraction

2.3.1. *Ex situ* X-Ray Diffraction

Ex situ X-ray diffraction was performed on a Bruker® D8 Advance using a diffractometer (Cu Kα radiation) utilising a 2θ range of 20 - 70° using a 0.02° step with a 1.45 s of count time per step. This diffractometer detailed on Figure 2-1 is composed of an X-ray source (on the left size), a series of slits and/or monochromators to constrain the beam light, a sample platform and a detector (right corner).

X-ray diffraction is used to determine the atomic and molecular structure of the phases within the samples before and after experiment. As our experiments are based on a powder sample, the different phases could be qualified and quantified using the powder method[40] with a good peak count statistic and no negative orientation effect. In an X-ray diffraction pattern, the peak positions and intensities give information about the structures of the different phases that are present in the sample and can also determine the crystal structure of unknown phases. As it can be seen for example on Figure 2-3,

a diffraction pattern is the representation of a sample diffraction intensity as function of the angle between the beam source and detector, designated as 2θ. By a preliminary qualitative analysis, the different phases in the sample can be identified. Then, with the Rietveld refinement method, using the fundamental approach (see below), the proportion of each phase and their crystal properties can be determined by fitting the profile intensity of the measured data against database references phases via the least squares method.

Figure 2-1: Scheme of Bragg Brentano geometry.[41].

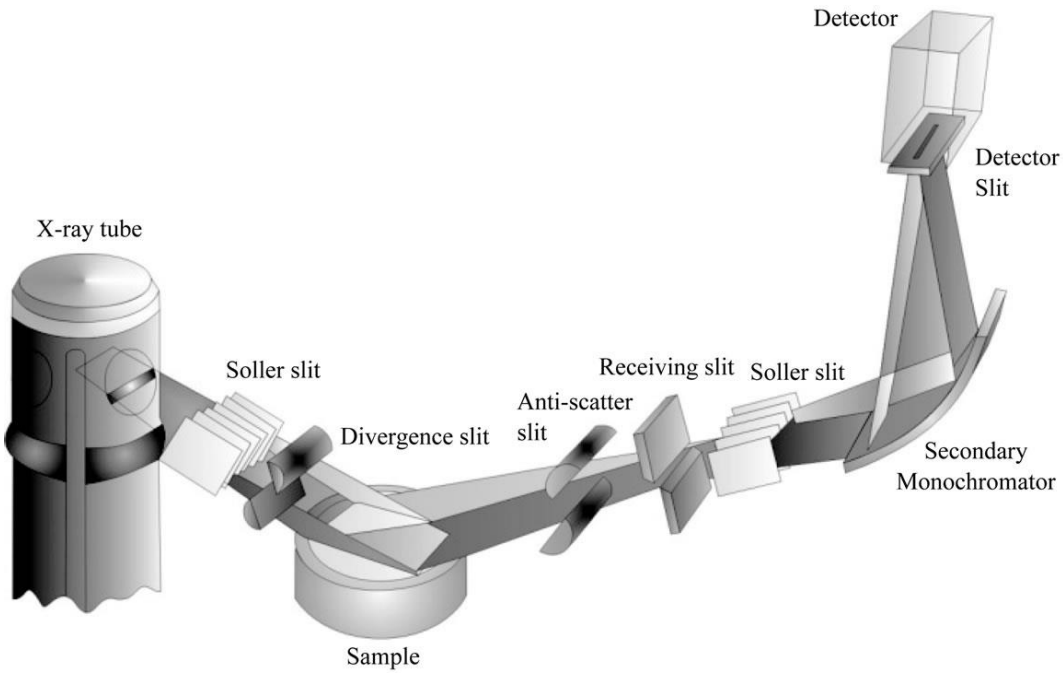

Samples were prepared in an air tight X-ray sample holder covered with a poly (methyl methacrylate) (PMMA) airtight bubble (insert on Figure 2-2) to prevent oxygen/moisture contamination during data collection. The PMMA bubble results in a broad hump in XRD patterns centred at ~20° 2θ (See Figure 2-2 at angles < 25°) characteristic of an amorphous structure.[41] In order to minimise this hump and maximize the diffraction peaks' intensity, the variable divergence slit (VDS) was set to 6 mm. It means that the divergent slits move in order to maintain a beam size equal to a diameter of 6 mm, independent of the angle (Figure 2-1). Thus, all signal is maintained focussed on the same sample area for better counting statistics, even for small amounts of material.

In practice, peaks were initially identified using Diffract EVA® thanks to International Centre for Diffraction Data (ICDD) database (PDF4+® 2016 and 2018 edition) by comparing the measured

diffracted peaks with the diffraction pattern of every phase structure existing in the database. Afterwards, the different datasheets of these phases are collected as a structure file (.str or .cif file). Then, Rietveld analysis[42] using the fundamental approach, by means of the TOPAS® software (Bruker®-AXS) is employed to quantify those phases. The fundamental parameter approach is to refine the instrument parameters (beam light wavelength or the beam line geometry) in combination with the intrinsic parameters of the present phases within the material (crystal size, preferred orientation, lattice parameter etc.) to create a calculated X-ray pattern. The objective is to fit the calculated model (red line on Figure 2-2) to the whole measured XRD pattern (black data points on Figure 2-2) in order to minimise the difference between these two (green line on Figure 2-2). The method uses the least squares refinement to fit the calculated pattern with the observed pattern. A typical level of fit achieved is with relative errors < 2 wt%.

Figure 2-2: Example of X-Ray analysis via TOPAS® software on an $xCaH_2 + ySi$ ball milled sample.

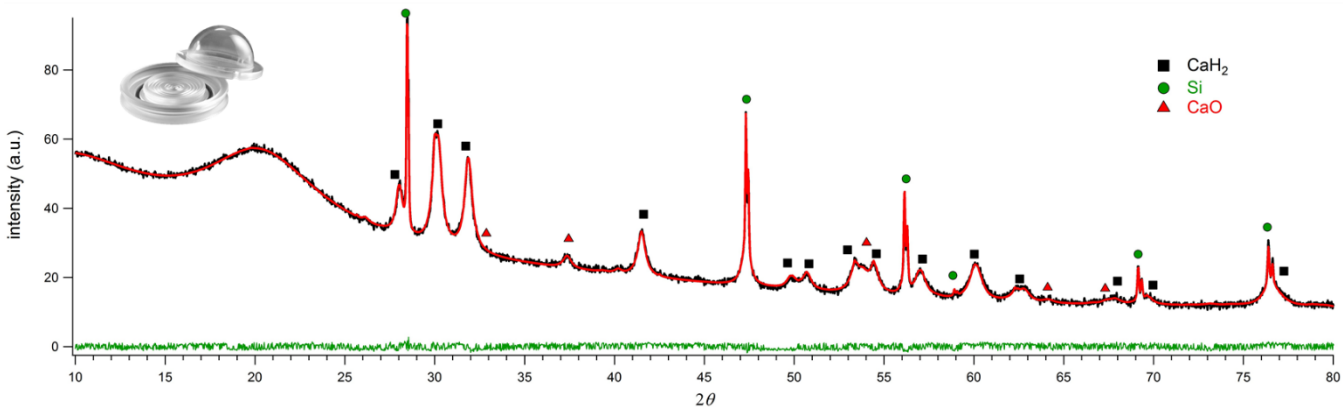

Ex situ XRD was employed before and after sorption experiments and quantitative analysis were used to identify if the material reacted, and in which proportion, so as to confirm the hydrogen wt % calculated for PCI or TPD (see section 2.5). Nonetheless, this measurement is, by definition, at room temperature after the temperature ramp. In order to observe the path of reaction i.e. to observe the diffraction pattern live during transformation, *in-situ* beam time was applied for on the Powder Diffraction Beamline at the Australian Synchrotron Facility in Melbourne.

2.3.2. *In situ* synchrotron Powder Diffraction

A beam time project proposal, highlighting the scientific purpose of the experiment and its potential benefits and outcomes was applied for and awarded. Experiments were performed at the Australian Synchrotron Facility in Melbourne at the Powder Diffraction beamline.

The samples, being air sensitive, were densely pre-packed in quartz capillaries and pre-mounted in a glovebox either at Curtin laboratory or at the synchrotron facilities. Each capillary was pre-mounted in a Swagelok 1/16" and 1/8 tube fitting using a graphite ferrule. The tubing (1/8" PEEK) connects the capillary-to-goniometer mount to the gas-handling manifold via a miniature quick-connect fitting in order to pre-define the H_2 pressured or vacuum atmosphere. To minimise the risk related to experimentation with hydrogen at high temperature, the following procedures were incorporated:

1. During experiments performed under H_2 pressure, the sample capillary couldn't be directly open to the H_2 supply during data collection. This implies that measurements involve only a small, fixed quantity of H_2. The quantity of H_2 is determined by the volume of gas handling reservoir (< 10 cm^3). Even if there is a capillary failure above the hydrogen auto-ignition temperature, < 10 mg of H_2 are available for ignition assuming 5 bar of H_2 pressure in the reservoir.
2. Furthermore, the low H_2 pressures and narrow dimensions of the capillaries (1 mm O.D.), places limits on the rate of H_2 release. The capillary-to-goniometer mount are 1/16" and 1/8 " O.D. Swagelok tube fittings and tubing are 1/8" O.D. This limit should be there in case of a leak or failure of the capillary (all other components had been pressure tested prior to the beam time).
3. Thick wall (> 0.02 mm for same external diameter: 1/8") quartz capillaries were used with H_2 backpressure below 5 bar and at a maximum temperature of 850 °C.

The experiments were performed using the high-resolution Mythen detector to follow decomposition pathways and, if required, provide data with high statistics that allowed the observation of all phases formed during the decomposition. This beamline delivers monochromatic synchrotron X-rays in the energy range of 5 to 30 keV from a bending magnet source. During the first round of experiment performed in the first semester of 2017, it was observed that the capillaries leaked due to cracking during the experiment, hence their wall thickness was increased to 0.05 mm.

2.4. Thermal analysis

Since 2016, Curtin University (CU) and Helmholtz-Zentrum Geesthacht (HZG) have built a collaboration based on the DAAD (Deutscher Akademischer Austauschdienst) project, led by Professor Craig Buckley and members of the HSRG from Curtin University, and by Dr. Martin Dornheim and Dr. Anna-Lisa Chaudhary from HZG.

Researchers from each organisation travelled between the two research groups for varying periods of time. During these visits a range of experimental activities, conference presentations and coordination of publications took place centred on different research topics.

In March-April 2017, Dr. Sofianos, a postdoctoral fellow, and I travelled to HZG for a total of two weeks. During this time, several samples were synthesised and characterised on site, with the helpful assistance of Dr A-L. Chaudhary. The synthesis, as previously described, included ball milling calcium hydride with either silicon or carbon additives in different stoichiometric ratios under inert atmosphere. The samples were transported in a sealed vial and canister to the different instruments. They underwent thermal analysis in an inert atmosphere (each machine in a dedicated glovebox) using Differential Scanning Calorimetry (DSC), (204 DSC HP Netzsch, Germany), Differential Thermal Analysis (DTA), Thermal Gravimetric Analysis (TGA) (STA-409 C Netzsch, Germany) and Mass Spectrometry (MS) (Hiden Isochema, UK). After each experiment, the present phases were identified using X-ray diffraction (D8 Discover, Bruker, Germany).

Simultaneous Thermal Analysis (STA) was used to observe the temperature onset point of each temperature up to 800 °C. STA is a combination of TGA and either DTA or DSC. In the HZG laboratory, TGA, DTA and MS are combined on the same instrument. Thermogravimetric Analysis (TGA) measures the change in mass of a sample as a function of temperature, using a high precision balance. The atmosphere is analysed using mass spectrometry during the experiment. The gas released at a specific temperature is detected and identified by its atomic masses.

Differential Thermal Analysis (DTA) measures thermal events occurring during a controlled heating program by measuring the temperature. A calibrated Differential Scanning Calorimetry (DSC) enables thermal events and heat capacity changes to be measured quantitatively by measuring the heat flow during a temperature ramp.

The HSRG also collaborates with The University of New South Wales, specifically Prof. Kondo-Francois Aguey-Zinsou for DSC measurement under inert atmospheres up to high temperature. Neither Curtin

nor HZG is equipped with a DSC instrument with the capability to measure DSC data at a temperature > 500 °C. Indeed, The Netzsch DSC equipment of HZG is limited to 500 °C for safety reason.

2.5. Sorption analysis

Facilities for sorption analysis are available within the Department of Physics and Astronomy at Curtin University. The HSRG have established and developed a suite of facilities for the characterisation of hydrogen storage materials. These facilities include volumetric H_2 gas rigs for testing the thermodynamic, kinetic and cyclic capacity stability of metal hydrides, Temperature Programmed Decomposition-Mass Spectrometry (TPD-MS), for testing the purity of H_2 evolved from the samples, two argon-filled glove boxes for handling the air sensitive metal hydrides and X-ray Diffraction instruments for phase identification of samples.

Figure 2-3: Schematic of the Sievert's apparatus. Image courtesy of HSRG staff.

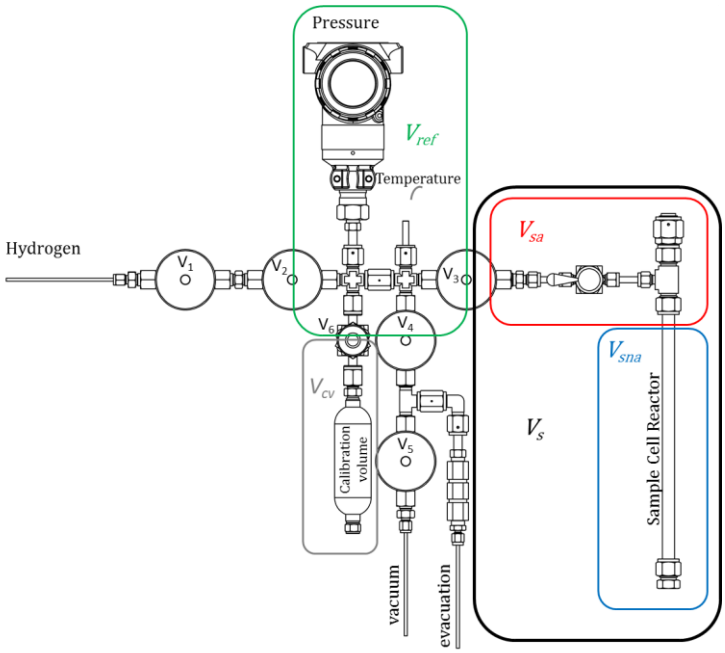

The Sievert's apparatus used either for PCI or TPD measurements are composed of a calibrated reference volume, which is filled with gas to a measured pressure and then opened to the sample side volume. The gas uptake by the sample is being calculated from the change in the gas pressure in the system.[43]

The sorption instrument (see Figure 2-3) is equipped with a hydrogen supply line (on the left of valve 1), a reference volume $\boldsymbol{V_{ref}}$ enclosed by Valve 2, Valve 3, Valve 4 and Valve 6, a pressure gauge consisting of a pressure transducer (precision of 0.02 %) and a sample volume $\boldsymbol{V_s}$. Part of the sample volume is heated by a furnace and is therefore divided into two parts: an ambient temperature sample volume $\boldsymbol{V_{sa}}$ equipped with a 4-wire platinum resistance temperature detector (RTD) that monitors the room temperature, and a non-ambient sample volume $\boldsymbol{V_{sna}}$, where the temperature is measured by a K-type thermocouple inside or outside the volume (as developed in section 2.5.3).

In order to calculate the change of pressure, a modified version of the ideal gas law (Equation 2-1) is required using the compressibility factor of hydrogen: *Z*. This factor is defined as the deviation ratio from the ideal gas law at a given temperature and pressure for high pressure (if P ≈ 1 bar, *Z*=1).

$$n = \frac{P \cdot V}{Z \cdot \mathrm{R} \cdot T} \qquad \text{Equation 2-1}$$

Where:

n = the number of moles of gas

P = the pressure of the gas in a specific volume (Pa)

V = the volume that the gas occupies (m^3)

T = the temperature of the gas in Kelvin

R = the universal gas constant (8.3145 $J \cdot K^{-1} \cdot mol^{-1}$)

Z = the compressibility factor.

The quantity of moles desorbed or absorbed during a step $\boldsymbol{i}$ is determined from the following equation (Equation 2-2):

$$n_{sor}^{i} = \frac{P_{ref}^{i} \cdot V_{ref}}{Z_{ref}^{i} \cdot \mathrm{R} \cdot T_{ref}^{i}} + \frac{P_{sa}^{i} \cdot V_{sa}}{Z_{sa}^{i} \cdot \mathrm{R} \cdot T_{sa}^{i}} + \frac{P_{sna}^{i} \cdot V_{na}}{Z_{sna}^{i} \cdot \mathrm{R} \cdot T_{sna}^{i}} \qquad Equation\ 1\text{-}2$$

All the volumes are calibrated before an experiment. V_{ref} was calibrated using a calibration volume V_{cv} after valve 2. This volume is calibrated using ethanol. The idea is to weigh the empty calibration volume, fill it up carefully with ethanol to avoid trapping air bubbles in the dead volume and weigh the calibration volume when it is full of ethanol. Knowing the temperature and using a temperature-

dependent formula for the density of ethanol, the calibration volume can be determined. Using the modified ideal gas law, V_{ref}. is calibrated. 1) V_{cv} is filled with hydrogen at pressure P_1. 2) Open valve 6 between V_{ref} and V_{cv} and wait for equilibrium to stabilise P_2. V_{ref} is calculated using equation 2-3:

$$\frac{P_1.V_{ref}}{Z_1.\mathrm{R}\cdot T_1} = \frac{P_2\cdot(V_{ref}+V_{cv})}{Z_2\cdot\mathrm{R}\cdot T_2} \qquad \text{Equation 2-3}$$

Using the same method, the sample volume side can be calibrated, V_s at room temperature knowing V_{ref}. Then, this measurement was repeated at high temperature. Using equation 2-2, a V_{sna} can be defined which is virtually the volume in the furnace at the desired temperature. This results in V_{sa}, which is the difference between V_s and V_{sna}.

Notes:

- Because of the configuration of the rig, a part of the sample ambient volume is at the temperature of the reference volume because it is in the rig box and is called $V_{s\ in\ the\ box}$. V_s is indeed the sum of $V_{s\ in\ the\ box}$ and $V_{s\ out\ the\ box}$.
  In order to reduce the error on pressure measurement, the dead volume must be reduced to a minimum. As seen on Figure 2-3, the reactor is filled with a sample cell* and alumina rods to occupy the dead space.

2.5.1. Principle of sorption measurement

The principle of TPD (Temperature Programmed Desorption) is trivial. A sample is placed in a furnace and, during the temperature ramp, the pressure evolved is measured in order to observe any sorption behaviour. When a sample is desorbing, the pressure should increase and when absorbing the pressure should decrease.

The principle of PCI (Pressure Composition Isotherm) measurement is based on the idea of Blach and Gray.[43] It's a stepwise method to determine the thermodynamic conditions of pressure at a stable temperature of a sorption reaction. For example, for a desorption measurement a sample is heated

* The sample powder is placed in a cell composed of a tube closed on one end and on the top a screw cap with a filter to stop the powder flying out.

in the sample cell reactor (SCR) under a predetermined pressure. Then the valve between the reference side and the sample side, V_3 is opened and the change of pressure is measured. After a predetermined duration step that considers the sorption kinetics, the pressure in the reference volume is reduced by a predetermined pressure step. After waiting for the pressure to reach equilibrium, V_3 is reopened to measure the pressure change at this new pressure. This sequence is then repeated. When the pressure goes underneath the equilibrium point, the metal hydride sample releases hydrogen and the pressure go back up to equilibrium. Given that the duration step and the pressure step increment have been well determined, the kinetic factor could be overlooked. This allowed the thermodynamics of the chemical reaction to be calculated. Using several PCI measurements at different isotherm temperatures, a van't Hoff plot (example on figure 4-26 in section 4.2.6) can be constructed. From eq. 2-4 (van't Hoff equation) the enthalpy $\Delta H_{reaction}$ and entropy $\Delta S_{reaction}$ of the chemical reaction can be calculated.

$$\ln\left(\frac{P_{\mathrm{H_2}}}{1\ bar}\right) = -\frac{\Delta H_{reaction}(P,T)}{\mathrm{R}\cdot T} + \frac{\Delta S_{reaction}(P,T)}{\mathrm{R}} \qquad \text{Equation 2-4}$$

2.5.2. Permeability and solubility corrections

When using a stainless-steel reactor, corrections in the hydrogen release weight percent are necessary at temperatures > 400 °C due to permeation of hydrogen through the reactor wall. Indeed, both PCI and TPD techniques are based on the pressure measurement to determine the hydrogen gas released by the material, but the pressure change can be due to other factors such as:

Hydrogen permeability of the stainless-steel reactor: depending on the permeability Φ of the sample cell reactor (SCR), a quantity of hydrogen may diffuse through the SCR walls during the measurement. Based on the diffusivity and permeability equations of San Marchi *et al.*[44], the number of moles lost per steps can be calculated as (equation 2-5):

$$n(\mathrm{H_2})_{\Phi}^{\mathrm{SCR\ calc.}} = SA \cdot J_{\infty} \cdot s \qquad \text{Equation 2-5}$$

Where $n(\mathrm{H_2})_{\Phi}^{\mathrm{SCR\ calc}}$ = calculated moles of hydrogen permeated through stainless steel SCR (mol H_2)

J_{∞} = the steady state diffusional flux of hydrogen per surface unit area (mol $H_2 \cdot m^{-2} \cdot s^{-1}$)

SA = the internal surface area of stainless steel exposed to gaseous hydrogen (m^2)

s = the measurement duration (s)

$$J_\infty = \frac{\Phi}{t} \cdot f^{\frac{1}{2}}$$ Equation 2-6

$$\Phi = \Phi_0 \cdot e^{\left(\frac{-H_0}{R \cdot T}\right)}$$ Equation 2-7

With Φ = the temperature dependent permeability of hydrogen (mol $H_2 \cdot m^{-1} \cdot s^{-1} \cdot MPa^{-1/2}$)

t = the thickness of stainless steel (m)

f = the fugacity of hydrogen (MPa)

H_Φ = the permeability activation energy ($kJ \cdot mol^{-1}$)

By combining equations 2-5, 2-6 & 2-7, the number of moles lost per steps can be calculated as:

$$n(\mathrm{H_2})_\Phi^{\mathrm{SCR\ calc.}} = \left(\frac{SA}{t}\right)_{\mathrm{eff}} \cdot \Phi_o \cdot e^{\left(-H_\Phi / R \cdot T\right)} \cdot f^{\frac{1}{2}} \cdot s$$ Equation 2-8

Where $(\frac{SA}{T})_{\mathrm{eff}}$ is a variable dependent on the geometry of the SCR. As the geometry can be complex to identify this value, it can be determined experimentally by measuring the pressure loss of an empty SCR over a long period (Eq. 2-9):

$$\left(\frac{SA}{t}\right)_{\mathrm{eff}} = \frac{n(\mathrm{H_2})_\Phi^{\mathrm{SCR.}}}{\Phi \cdot f^{\frac{1}{2}} \cdot s}$$ Equation 2-9

The lower this value is, the smaller the quantity of hydrogen loss through the SCR.

Hydrogen solubility of the stainless-steel reactor: at each pressure step, a quantity of hydrogen is absorbed in the stainless-steel reactor. When the pressure is lowered, some hydrogen is released within the reactor walls. It is necessary to correct for this quantity of hydrogen release between each step using the following expressions(equations 2-10 and 2-11).[44]

$$C_l = K \cdot f^{1/2}$$ Equation 2-10

$$K = K^0 \cdot e^{\left(\frac{-\Delta H_S}{R \cdot T}\right)}$$ Equation 2-11

Where C_l is the equilibrium concentration of hydrogen dissolved in the metal lattice ($mol.m^{-3}$), depending on the operating temperature and pressure (or fugacity):

K is the solubility, which is independent of pressure, but dependent on temperature, as shown in Equation 2-11, (mol $H_2 \cdot m^{-3} \cdot MPa^{-1/2}$)

K^0 is the standard state solubility coefficient (mol $H_2 \cdot m^{-3} \cdot MPa^{-1/2}$)

ΔH_s= enthalpy of formation of H-atoms bond in the metal ($kJ \cdot mol^{-1}$)

In order to calculate the number of moles of hydrogen released during each step by SCR due to its solubility, the difference in moles of hydrogen dissolved between the final pressure and starting pressure is calculated (Equation 2-12).

$$n(H_2)_K^{SCR} = C_l^{final} \cdot V^{SCR} - C_l^{beginning} \cdot V^{SCR} \qquad \text{Equation 2-12}$$

2.5.3. Sample Cell Reactor

There are two basics approaches to creating a permeation barrier to limit the need for the above corrections. One is creating an oxide layer directly on a stainless-steel SCR and the other is the use of a silicon carbide SCR because of its low intrinsic permeability. Both techniques have their pros and cons. Aluminised stainless steel SCR have a higher possible operating pressure but the aluminium coating degrades at temperatures > 650°C. On the other hand, an α-SiC ceramic SCR is not limited in temperature but is limited in pressure due to its brittleness. Figure 2-4 is from references[45-47] and the internal measurement shows that an aluminised stainless steel and an α-SiC ceramic SCR have a permeability lower than a stainless steel SS316 SCR by a factor of 10.

The two techniques are complementary, the aluminised stainless-steel SCR is used for high pressure whereas a α-SiC ceramic SCR is used for high temperature measurement under limited pressure.

Figure 2-4: Comparison of Hydrogen permeability of common materials as function of temperature. Figure made by HSRG staff using reference data.[45, 46]

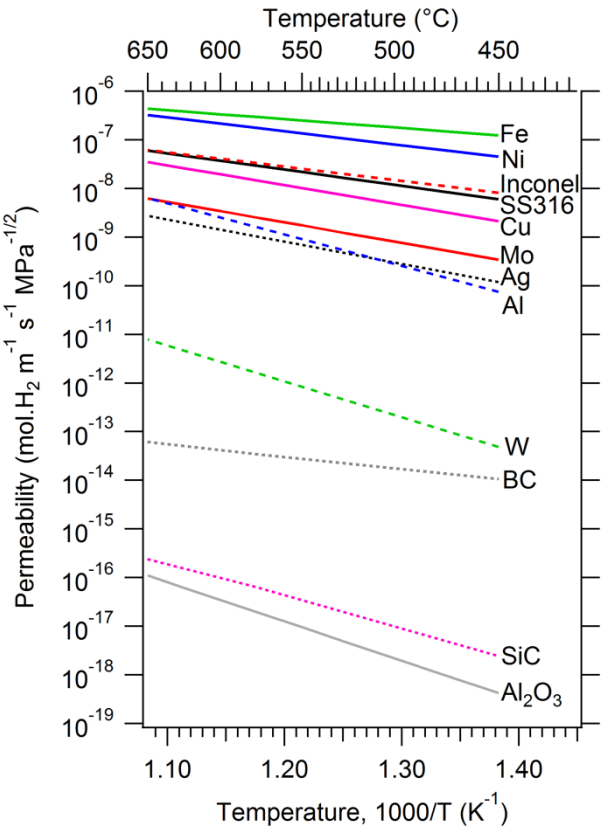

Aluminised stainless steel SCR:

In our case, an aluminised stainless-steel tube was built from 300 mm lengths of ½" stainless steel 316L tubing (OD = 12.7 mm, ID = 8.5 mm, Swagelok). The tube was aluminised via a packed-bed cementation technique, where the tube to be coated was surrounded by blended aluminium powders and heated to initiate a reaction between the aluminium powder and the steel surface.[47] It was processed by Endurance Technologies Inc. Canada® resulting in an external aluminium oxide layer being formed. This layer forms an impermeable barrier to hydrogen. It has been observed that the Al_2O_3 layer improves the permeability of coated stainless steel by up to four orders of magnitude.[46]

Note: As seen on Figure 2-5, the upper part was attached to a T-shaped tube union while the bottom part was sealed with an uncoated ½" stainless steel 316L tube endcap fitting and a ferrule. A correction on the hydrogen ratio was required due to the flux diffused through the endcap and the hydrogen dissolved in the endcap steel volume during each step of the measurement.

Figure 2-5: Picture of a SCR with aluminised tube used for sorption measurement at T ≤ 700°C.

α-SiC SCR:

For High temperature measurement, a SCR based on an α-SiC ceramic tubing has been designed, optimised and tested. This tube, purchased from Saint Gobain tubes (Hexoloy® SA SiC) (length of 450 mm, outer diameter (O.D.) of ~16.2 mm, wall thicknesses of ~2.9 mm and inner diameter (I.D.) of ~10.4 mm) was connected to the Sieverts equipment using a Swagelok® tube fitting. In practice, several ferrules were tested including (Figure 2-6):

- Brass ferrules: brass material is resistant to high temperature. Due to the fragility of the silicon carbide ceramic tube, it is a difficult task to tide the nut around the ferrule without breaking the tube. At room temperature the reactor was sealed i.e. no pressure loss for 24 hours, but due to the difference of thermal expansion between the three materials, the connection leaks at high temperature.

- Graphite ferrule: The ferrule is soft and in theory could adapt to thermal expansion. In practice, the ferrule delaminates during the building of the reactor. A large quantity of this expensive ferrule is thus wasted during this process.

- Teflon ferrule: These ferrules are soft and hence are the easiest to manipulate. At room temperature, leak testing revealed no loss of pressure after 24 hours. The ferrules lose their sealing capacity over 100 °C, due to the glass transition effect of the polytetrafluoroethylene (PTFE) material. The ferrules are affordable and easy to adapt, and a well-sealed connection is possible without applying an excessive torque on the α-SiC ceramic tube.

Figure 2-6: Pictures of the different ferrules tested to connect the α-SiC tube to the Swagelok stainless steel connections.

Using the Teflon ferrules for the reasons explained above, a SCR (Figure 2-6) was build, and a cooling system at the top of the furnace was settled. This system was composed by a heat sink, a thermal isolation and a fan to maintain the ferrule under 100 °C. Burst tests with water at 25 °C according to Australian Standards AS1180.5 were undertaken (Maximator®, Australia) to establish safe operating conditions of pressure. It was shown that the burst pressure was 387 bar. After discussion with the tube supplier, an arbitrary safety factor of 10 was defined, in case the ceramic had an invisible point of weakness. As can be seen on Figure 2-7, to avoid an over pressure, a blow-off valve regulated to ≈ 15 bar was installed on the SCR.

Figure 2-8 shows the temperature gradient along the silicon carbide tube. Because the upper part must be cooled for the ferrule, the temperature has to reduce from 700 °C on the sample side to less than 100 °C at the ferrule side. In order to have a good measure of the pressure, a K-type thermocouple is placed inside of the SCR directly in contact with the sample cell. It can be observed on Figure 2-8 insert that the sample cell has a specific design. Thanks to ergot at both ends (on the

bottom and on the top screwed endcap), the sample cell is slid into two alumina tubes at both ends. The purpose is to avoid contact between the stainless steel and α-SiC material of the SCR. The literature reports a possible reaction between these two materials at high temperature.[48-50] The bottom tube length has been minimised for the sample to stay in the quasi-isothermal part of the reactor.

Figure 2-7: Cooling and safety system on the α-SiC reactor using Teflon ferrule.

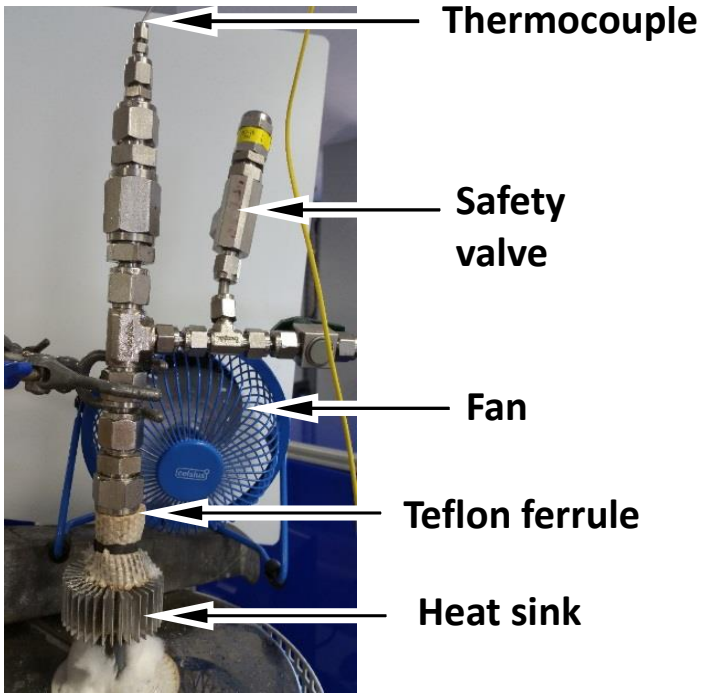

Figure 2-8: Picture of α-SiC SCR, temperature gradient along the tube and stainless-steel sample cell assembly.

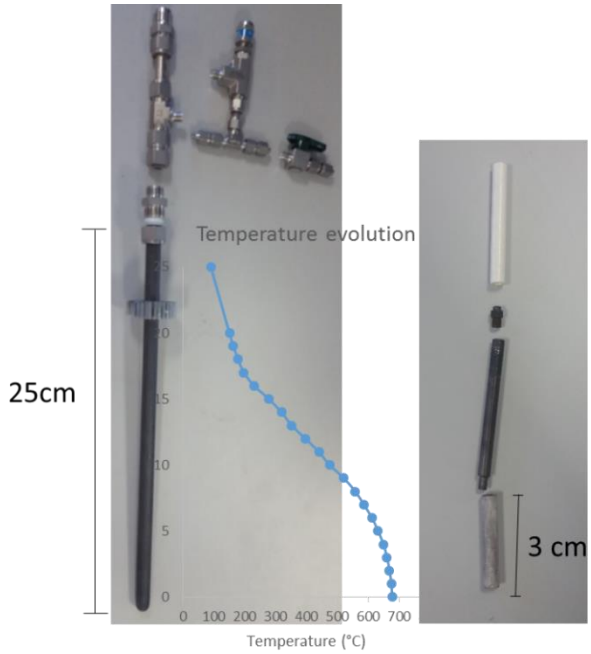

Examples of sorption measurement, using either aluminised stainless steel SCR or α-SiC SCR will be detailed in chapters 4, 5 and 6, as well as the detailed information provided by thermal analysis and X-ray diffraction analysis. The choice of temperatures for performing measurements was based on the predicted thermodynamics of the sample (see chapter 3).

3. Prediction and Thermodynamic calculation

3.1. Theory

The aim of this section is to explore new high temperature metal hydride systems with a good balance between cost and thermal energy storage capacity. To develop a new class of low-cost calcium-based metal hydrides systems that can act as thermochemical heat storage materials in the temperature range of 600 °C to 800 °C, the potential for reversible reactions between calcium hydrides with a second low-cost element or compound has been explored. This involved compiling a database of thermodynamic properties of each possible product in order to predict chemical reactions that can occur at high temperature.

3.1.1. Thermodynamic calculations

Utilising the HSC® software, thermodynamic calculations were performed to determine which elements or compounds (*M*) can be added to calcium hydride to destabilise it. The name of this software program is based on the thermochemical parameter used for calculations: enthalpy (*H*), entropy (*S*) and heat capacity (*Cp*). Thanks to these data, it is possible to calculate the temperature at which any reaction can occur for an initial mixture of different elements or alloys, to determine which reaction or reaction step is thermodynamically favourable.

Enthalpy H: is defined as the thermodynamic property of a system equal to the sum of its internal energy *U* and the product of its pressure *P* and volume *V*. If an outside pressure on a system is held constant, a change in enthalpy entails a change in the system's internal energy, plus a change in the system's volume. The system exchanges energy with the outside world. For example, in **endothermic** chemical reactions, the change in enthalpy ΔH_{RXN} ($\Delta H_{RXN} = \sum H_{product} - \sum H_{reactant}$) is the amount of energy absorbed by the reaction, while in **exothermic** reactions, it is the amount given off.

The absolute values of enthalpy *H* of substances cannot be measured, but the enthalpy change between two temperatures can be determined with a calorimeter. Elements in their standard state make no contribution to the enthalpy calculations for a reaction, as the enthalpy of an element in its standard state is zero. This is called the reference state. So H_f^0Ca, $H_f^0$$H_2$, H_f^0(Metals) are zero (this value is not null for a compound which is formed at high temperature). Enthalpy evolution with the

temperature is define as a function of the C_p variations integer. During a phase transformation of an element or an alloy (fusion, solid phase changes etc.), the system gives or absorbs spontaneously an amount of energy $\mathbf{H}_{tr}$ (Equation 3-1).

$$\boldsymbol{H^T} = \boldsymbol{H_f^0} + \int_{\mathbf{298.15}}^{\boldsymbol{T}} \mathbf{C_p}\ \mathbf{dT} + \sum \boldsymbol{H_{tr}} \quad \text{Equation 3-1}$$

In the case of the hydrogen storage system, the sorption reaction enthalpy $\Delta H_{\text{sorption}}$ per mole of hydrogen released (n_{H_2}) or taken defines the quantity of heat that can be stored by a thermochemical reaction.

Entropy S: is a measure of the amount of disorder in a system. Entropy increases as the system's temperature increases (Equation 3-2).

$$\boldsymbol{S^T} = \boldsymbol{S_f^{298.15}} + \int_{\mathbf{298.15}}^{\boldsymbol{T}} \frac{\boldsymbol{C_p}}{\boldsymbol{T}}\ \mathbf{dT} + \sum \frac{\boldsymbol{H_{tr}}}{\boldsymbol{T_{tr}}} \qquad \text{Equation 3-2}$$

Heat Capacity Cp: the heat capacity is the amount of heat required to raise the temperature of a phase by one degree Kelvin. C_p is defined as a polynomial expression of the temperature (see equation 3-13).

Gibbs Energy G: A reaction becomes spontaneous when the Gibbs free energy change between the reactants and products (ΔG) is zero or negative. The operating temperature can be estimated when ΔG equals zero.

The Gibbs free energy of the possible reaction determines which reactions occurs and at what temperature (and pressure) (Equation 3-3). The standard pressure is defined as 1 bar. The operating temperature of a desorption reaction is generally defined as $T_{1\text{bar}}$, which is the temperature of reaction under 1 bar of hydrogen back pressure (Equation 3-4).

$$\Delta G_{RXN}^{p,T} = \sum G_{product}^{p,T} - \sum G_{reactant}^{p,T} \qquad \text{Equation 3-3}$$

$$\Delta G_{RXN}^{0,T} = 0 = \Delta H_{RXN}^{0,T} - T_{1\ bar} \cdot \Delta S_{RXN}^{0,T} \qquad \text{Equation 3-4}$$

3.1. Model and source of data

An important part of this work has been to explore the published literature to find thermodynamic data on each compound of interest, such as the standard enthalpy of formation or standard entropy of different alloys. The enthalpy and entropy of formation evolution with temperature depends on the heat capacity of the materials.

3.1.1. Pure elements

In Dinsdale *et al*. review [51] the Gibbs free energy is defined as a function of the temperature for all the pure elements for each phase (solid *α* or *β* or *γ*, liquid and gas phases) at all ranges of temperature as for the calcium example:

Ca:

<u>Phase *α* or FCC</u>

- at 298.15 K < *T* < 1115 K range

$G_{\alpha-Ca}^{0,T}$ (J.mol^{-1}) = -4955.062 + 72.794266 *T* - 16.3138 T ln(*T*) -11.10455 x10^{-3} *T*^{2} - 133574 *T*$^{-1}$

- at 1115 K < *T* < 3000 K range

$G_{\alpha-Ca}^{0,FCC}$ (J·mol^{-1}) = 107304.428 + 799.982066 *T* – 114.2922467 *T* ln(*T*) +23.733814 x10^{-3} *T*^{2} - 1.2438 x10^{-6} *T*^{3} + 18245540 *T*$^{-1}$

<u>Phase *β* or BCC</u>

- at 298.15 K < *T* < 716 K

$\Delta G_{\beta-Ca}^{0,T}$ (J·mol^{-1}) = -7020.852 + 142.970155 *T* – 28.2541 T ln(*T*) + 7.2326 x10^{-3} *T*^{2} – 4.500217 x10^{-6} *T*^{3} + 60578 *T*$^{-1}$

- at 716 K < *T* < 1115 K

$G_{\beta-Ca}^{0,T}$ (J.mol^{-1}) = 1640.475 + 1.999694 *T* - 6.276 *T* ln(*T*) – 16.1921 x10^{-3} *T*^{2} – 523000 *T*$^{-1}$

- at 1115 K < *T* < 3000 K

$G^{0,T}_{\beta-Ca}$ (J·mol^{-1}) = -142331.096 + 1023.549046 T – 143.8726979 T ln(T) + 32.543127 x10^{-3} T^2 – 1.704079 x10^{-6} T^3 + 25353771 T^{-1}

Liquid phase

- 298.15 K < T < 500 K

$G^{0,T}_{l-Ca}$ (J·mol^{-1}) = 5844.846 + 62.4838 T – 16.3138 T ln (T) -11.10455 x10^{-3} T^2 -133574 T^{-1}

- 500 K < T < 1115 K

$G^{0,T}_{l-Ca}$ (J·mol^{-1}) = 7838.856+ 18.2979 T – 8.9874787 T ln (T) -22.66537 x10^{-3} T^2 +3.338303 x10^{-6} T^3 - 230193 T^{-1}

- 1115 K < T < 3000 K

$G^{0,T}_{l-Ca}$ (J·mol^{-1}) = -2654.938 + 188.9223 T – 35 T ln (T)

From the above formulas, Entropy S (J·mol^{-1}·K^{-1}), Enthalpy H (J·mol^{-1}) and Heat Capacity C_p (J·mol^{-1}·K^{-1}), can be calculated with the following equations:

$$S = -\left(\frac{dG}{dT}\right) \qquad \text{Equation 3-5}$$

$$H = G + T \cdot S \qquad \text{Equation 3-6}$$

$$C_p = -T \cdot \left(\frac{d^2G}{dT^2}\right) \qquad \text{Equation 3-7}$$

The Gibbs free energy of the different phases of the Ca element: α-Ca (FCC-A1), β-Ca (BCC_A2), γ-Ca (HCP_A3) and liquid phase is plotted on Figure 3-1 using α-Ca (FCC-A1) as reference. The most stable phase at any temperature is the one with the lowest Gibbs free energy. In a reaction where pure Ca is a reactant, Ca must be defined as α-Ca (FCC) from room temperature to up to 716 K, β-Ca (BCC) from 716 K to 1115 K and liquid phase above 1115 K to define $G^{0,T}_{Ca}$. It can be seen in the next section that the Gibbs free energy of some compounds is defined as a function of only one phase as α-Ca (FCC). So

both need to be calculated: $G_{\alpha-Ca}^{0,T}$ because it is in the definition of $G_{CaH_2}^{0,T}$ and $G_{Ca}^{0,T}$ because as a reactant it needs to be defined as the most favourable phase at each range of temperature.

Figure 3-1: Gibbs free energy of Ca in kJ·mol^{-1} (G_{Ca}) change with temperature at standard pressure.[3]

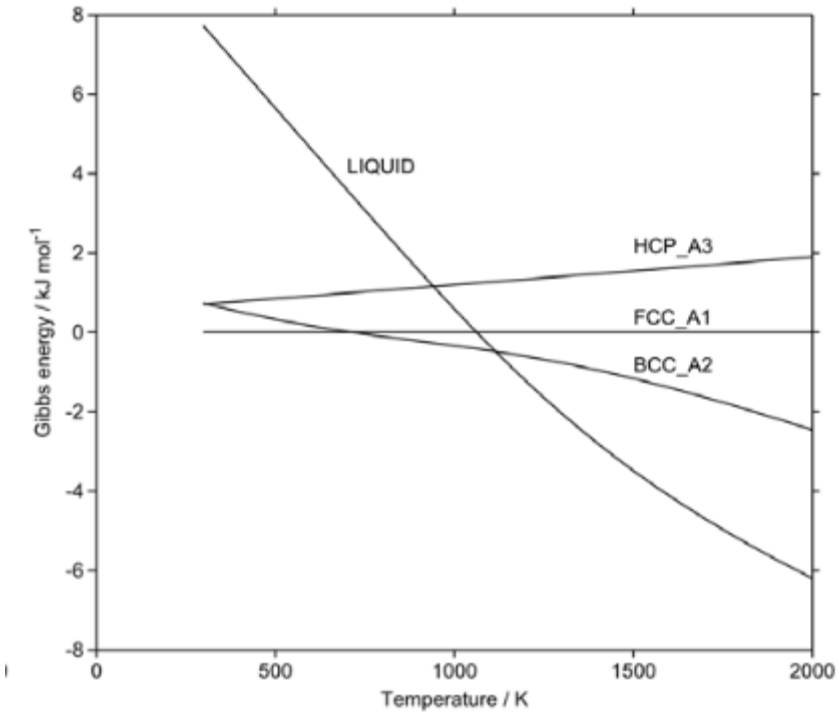

3.1.2. Compounds

To find thermodynamic data for compounds, literature had to be explored and the most recent and accurate values had to be selected. For example, in the case of CaH_2, the Gibbs free energy of the compound (equation 3-8) is a function of the Gibbs free energy of formation (equation 3-9) and a fraction of the Gibbs free energy for each element.

$$G_{CaH_2}^{0,T} = \Delta G_{f\ CaH_2} + G_{\alpha-Ca}^{0,T} + G_{H_2(gas)}^{0,T} \qquad \text{Equation 3-8}$$

$$\Delta G_{f\ CaH_2} = a + bT \qquad \text{Equation 3-9}$$

According to Wang *et al.* [30, 52], the calcium hydride phase is defined as the sum of the Gibbs free energy of formation plus the Gibbs free energy of α-Ca and H_2 (gas).

- Phase α-CaH_2 at 298.15 K < T < 1053 K

$$\boldsymbol{G^{0,T}_{\alpha-CaH_2}}\ (\mathrm{J\cdot mol^{-1}}) = -174380.22 + 127.25\ T + G^{0,T}_{\alpha-Ca} + G^{0,T}_{H_2(gas)} \quad \text{Equation 3-10}$$

- Phase *β*-CaH_2 at 1053 K < *T* < 1255 K

$$\boldsymbol{G^{0,T}_{\beta-CaH_2}}\ (\mathrm{J\cdot mol^{-1}}) = -167681.34 + 120.92\ T + G^{0,T}_{\alpha-Ca} + G^{0,T}_{H_2(gas)} \quad \text{Equation 3-11}$$

- Phase l-CaH_2 at *T* > 1255 K

$$\boldsymbol{G^{0,T}_{l-CaH_2}}\ (\mathrm{J\cdot mol^{-1}}) = x_{\mathrm{Ca}} \cdot \mathrm{G^{0,T}_{l-Ca}} + x_{Ca} \cdot \mathrm{G^{0,T}_{l-H}} + \mathrm{R} \cdot T \cdot (x_{Ca} \cdot \ln(x_{Ca}) + x_H \cdot \ln(x_H)) + x_{Ca} \cdot x_H \cdot \sum_{i=0}^{n} \mathrm{L^i} \cdot (x_{Ca} - x_H)^i \quad \text{Equation 3-12}$$

Where x_{Ca} and x_H are the molar ratio of the species, $\mathrm{G^{0,T}_{l-Ca}}$ and $\mathrm{G^{0,T}_{l-H}}$ are the Gibbs free energies of the element taken from Dinsdale *et al.*[51] and from Qui *et al.*[53], respectively. R is the gas constant. $\mathrm{L^i}$ are interaction parameters defined as a linear function of the temperature.

3.1.3. Source of data

The HSC database is composed of standard enthalpies in their most stable state at 25 °C and 1 bar, H^0 (kJ·mol^{-1}), S^0 the standard entropy of the substance and the different coefficients *A, B, C* and *D,* which define the temperature dependence of heat capacity C_p as described below (Equation 3-13):

$$C_p = A + B \cdot 10^{-3} \cdot T + C \cdot 10^5 \cdot T^{-2} + D \cdot 10^{-6} \cdot T^2 \quad \text{Equation 3-13}$$

"The data in the HSC Chemistry Main database is not critically evaluated or always internally consistent. However, the accuracy is usually good enough for most thermo-chemical calculations. HSC provides fast access to data and references found in literature".[54] The purpose here is not to criticise the data in HSC but because the available version is not the latest one (last update: 2006), thermodynamic information may have since been corrected or updated. Hence the HSC© thermodynamic database needs to be cross-checked with information in the literature. In other instances, the HSC database for Ca – metal binary systems is either absent or incomplete.

For the example of calcium hydride decomposition, the HSC databases refers to the book "Thermodynamic data of pure substance" (version 1993) from Barin *et.al*[55] for the thermodynamic values. Barin *et al*. refer in turn to Pankratz's *et al*. book[56] for the origin of the data. The standard heat capacity as the relative enthalpy and entropy is calculated here using a program subroutine to fit a

polynomial model to experimental data. On the other hand, using Equation 7 with Wang's formula (Equations 10 to 12) $C_{p_{\mathrm{CaH_2}}}$ is defined as a function of $C_{p_{Ca}}$ and $C_{p_{\mathrm{H_2}}}$. These formulas were obtained using the CALPHAD method. As shown on Figure 3-2-a, the C_p change is calculated for α-CaH_2 from room temperature up to 1053 K phase, but is estimated as constant for the β-CaH_2 and the liquid phase, with a jump at the melting point. These changes have an influence on the value of the Gibbs free energy at high temperature, but not on the profile curve (Figure 3-2-b).

Figure 3-2: Comparison of (a) Cp and (b) G between the HSC database and the manually calculated data from the Wang formulas.

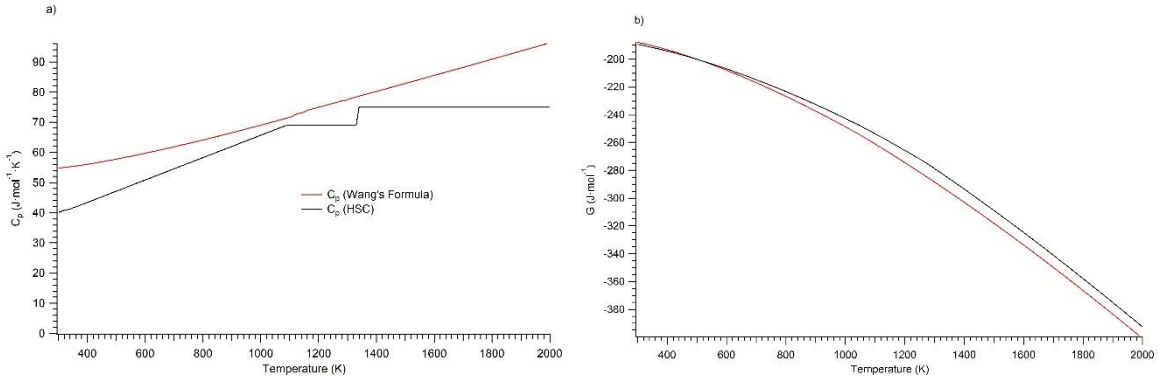

It is possible to create into HSC© one own updated database in order to be able to automatically calculate the thermodynamic properties with these data. For example, Table 3-1 compares the temperature of reaction at 1 bar of hydrogen back pressure, enthalpy ΔH and entropy ΔS of reaction at T_{1bar} for CaH_2 decomposition calculated with the initial HSC database and the updated data. A real change in value is observed. This work had to be done for every system. For every compound evaluated the database was double-checked and updated.

Table 3-1: Comparison of thermodynamic calculation of the reaction $CaH_2 \rightleftarrows Ca + H_2$ between the HSC initial database, using an updated set of data.

	$CaH_2 \rightleftarrows Ca + H_{2\,(g)}$	
	HSC[57]	HSC updated[30]
$T_{(1bar)}$	1018.4°C	1092°C
ΔH at T_{1bar}	162.4 kJ·mol^{-1}·H_2	174.9 kJ·mol^{-1}·H_2
ΔS at T_{1bar}	125.7 J· K^{-1}·mol^{-1}·H_2	128.1 J· K^{-1}·mol^{-1}·H_2

The value of C_p at room temperature seems to be estimated wrongly in the updated database. Indeed, the accuracy of the old HSC database might be poor in many cases, but the heat capacity at room temperature is generally based on experimental results. On the other hand, C_p is estimated by a theoretical formula. Despite this approximation, the HSC updated version for Ca, H_2 and mainly CaH_2 thermodynamics parameters has been used for all the thermodynamic calculations because the values calculated in Table 3-1 are closer to the experimental values measured by Curtis *et al.*[31] for calcium hydride decomposition.

3.1.4. Destabilisation principle

The Thermodynamic destabilisation was determined to decrease the temperature at which H_2 is released from metal hydrides with the goal of using these hydrides for hydrogen storage in cars.[3] Destabilisation involves adding a second element or compound to a metal hydride to change the reaction pathway associated with H_2 release. As shown on Figure 3-3, adding a well-chosen element to a HTMH reduces the hydrogen release reaction enthalpy and therefore the operating temperature.

Figure 3-3: Generalised enthalpy diagram illustrating destabilisation. [3]

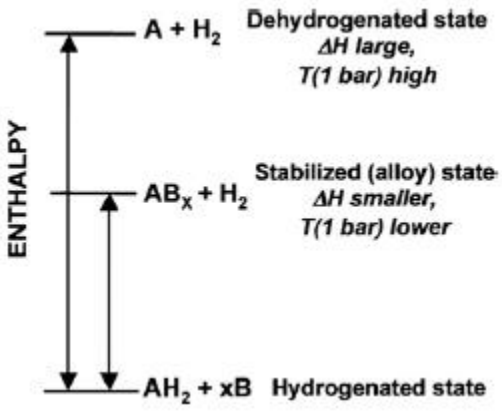

CaH_2 is a stable hydride[27] with a 1 bar H_2 equilibrium pressure over 1000 °C (reaction 3-1).[58] By adding metallic elements or compounds to calcium hydrides, the reaction Gibbs free energy may decrease (reaction 3-2).

$$Ca + H_2 \rightleftarrows CaH_2 \qquad \text{reaction 3-1}$$

$$Ca_xM_y + xH_2 \rightleftarrows xCaH_2 + yM \qquad \text{reaction 3-2}$$

M can be a metallic element or a metallic alloy. Equation 3-4 shows that in order to reduce the temperature of reaction, the enthalpy and/or entropy of reaction should be reduced. That's why destabilisation is always accompanied by a drop-in heat storage capacity due to the reduction of enthalpy of reaction. In order to compile the values of H_f^0Ca, S_f^0Ca ,$H_f^0H_2$, $S_f^0H_2$, H_f^0M, S_f^0M, H_f^0CaxMy ,and S_f^0CaxMy of every possible compound as well as the relative C_p parameter, the literature has to be explored and sources need to be compared.

3.2. Example: Al-Ca System

In order to confirm that the model of thermodynamic prediction applied to the destabilised calcium hydride system was working, it was decided to calculate the thermodynamic data, both manually and using the HSC software, for a system that had already been studied in the literature; the Al-Ca system.

The thermodynamic data of all compounds that can be formed from Al and Ca was collected from the most recent phase diagram of the Al-Ca system (Figure 3-4).[52] This thermodynamic data was then used to calculate possible reactions between CaH_2 and Al.

Figure 3-4: Phase diagram of Ca-Al system.[52]

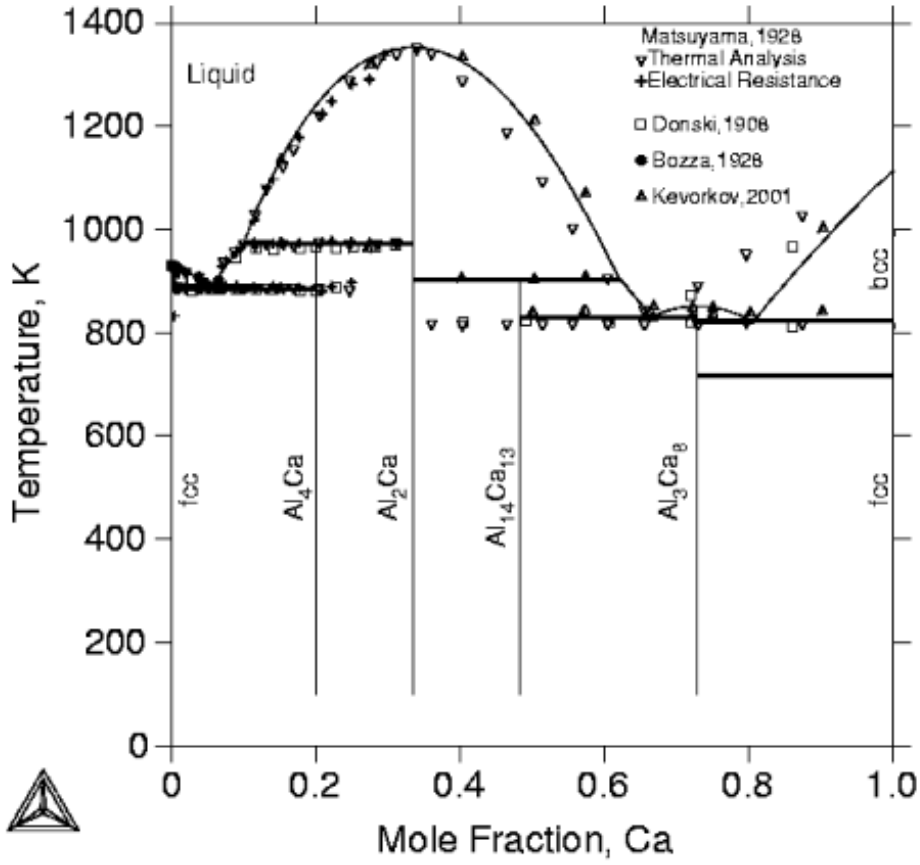

According to Veleckis *et al*.[59] and confirmed recently by Ward *et al*.[21], from their experimental results there are two reactions that occur in the CaH_2-Al system. Using PCI analysis in the ranges 400 - 630 °C and 0.2 - 11 bar and defining the enthalpy and entropy of reaction through the van't Hoff plot equation. Integration of these expressions has produced the standard free energies of formation, hence a temperature of reaction at 1 bar equilibrium pressure. The results are the following:

$$CaH_2 + 4Al \rightleftarrows Al_4Ca + H_2 \qquad \text{reaction 3-3}$$

- $\Delta H_{rxn} \approx 76$ kJ·mol^{-1} H_2
- $T_{1bar} \approx 414$ °C

$$CaH_2 + Al_4Ca \rightleftarrows 2Al_2Ca + H_2 \qquad \text{reaction 3-4}$$

- $\Delta H_{rxn} \approx 90.1$ kJ·mol^{-1} H_2
- $T_{1bar} \approx 481$ °C

On the other hand, all the possible reactions between calcium hydride, pure aluminium and all the calcium-aluminium phases that we can observe on the phase diagram (Figure 3-4) have to be calculated using the thermodynamic model, in order to cross-check that the reactions above are the preferable ones. These data are summarised in Table 3-2. Reaction 1 of Table 3-2 is the one predicted to occur at the lower temperature, releasing H_2 and forming Al_4Ca. Then, the Al_4Ca compound reacts with CaH_2 to form Al_2Ca (reaction 6 of Table 3-2).

In conclusion, the multistep reactions measured by Veleckis *et al*. are similar to the predictions calculated in this thesis. This result confirms that our calculation model is correct, with an error of ±5 °C for temperature and ± 8 kJ·mol^{-1} for enthalpy between the theoretical and the experimental values.

Table 3-2: Temperature of reaction and enthalpy per mole of hydrogen of every possible reaction for the CaH_2-Al system

	Possible reactions between CaH_2 &:	$T_{(1bar)}$ °C	ΔH (kJ·mol^{-1}·H_2)
	Al		
1	$CaH_2 + 4Al \rightleftarrows Al_4Ca + H_2$	417	74.21
2	$CaH_2 + 2Al \rightleftarrows Al_2Ca + H_2$	453	78.24
3	$8CaH_2 + 3Al \rightleftarrows Al_3Ca_8 + 8H_2$	961	143.02
4	$13CaH_2 + 14Al \rightleftarrows Al_{14}Ca_{13} + 13H_2$	736	116.27
	Al_2Ca		
5	$6CaH_2 + 7Al_2Ca \rightleftarrows Al_{14}Ca_{13} + 6H_2$	1122	187.04
	Al_4Ca		
6	$CaH_2 + Al_4Ca \rightleftarrows 2Al_2Ca + H_2$	486	82.26
7	$29CaH_2 + 3Al_4Ca \rightleftarrows 4Al_3Ca_8 + 29H_2$	1009	151.22
8	$9.5CaH_2 + 3.5Al_4Ca \rightleftarrows Al_{14}Ca_{13} + 9.5H_2$	840	132.75

This result is highlighted on Figure 3-5, which shows how Al_4Ca is formed first and is then consumed in a further reaction with CaH_2 to form Al_2Ca. This figure has been plotted using the equilibrium composition module of HSC®. Starting from an initial reactant mixture, this module is used to calculate the equilibrium composition at different temperatures and pressures. In this case, the pressure is configured at 1 bar equilibrium. The "pure substance in the last phase" option and Criss-Cobble extrapolation[60] have been chosen. Resulting from this parameter's choice, the temperature of reaction observed is the temperature of reaction at 1 bar. This product is created based on reactants that are consumed at the same temperature. Indeed, the compounds are considered as being ideal

solid solutions, which means that the activity coefficient has been estimated as binary 0 or 1. The intermediate solution with an element dissolved in it are excluded.

Figure 3-5: Equilibrium composition of the CaH_2 + Al system with an initial composition of 1 mole of CaH_2 and 2 moles of Al.

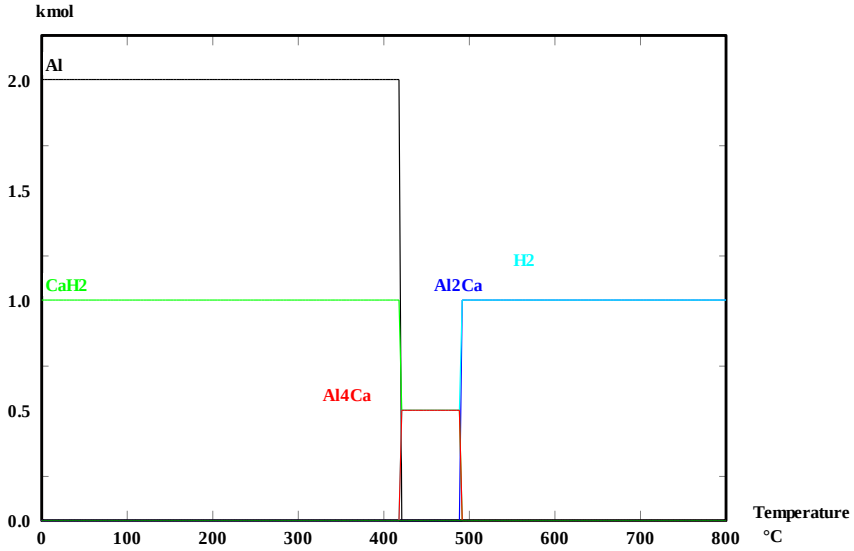

3.3. Study of different $xCaH_2$ + yM system

To develop new classes of low-cost metal hydride systems based on calcium, that can act as thermochemical heat storage materials in the temperature range of 600 °C to 800 °C, a comprehensive study of the calcium hydride/metal alloys system was undertaken. The process consisted of compiling a database of thermodynamic properties of each calcium hydride + metal system in order to predict chemical reactions that can occur at high temperature. Based on the published thermodynamic data ΔH_f^0, ΔS_f^0, *A, B, C* and *D* factors for various Ca-*M* systems, the preferential scheme of reactions between CaH_2 and different metals, *M* were determined.

A pre-review of the literature and/or cost and abundance study has been done in order to select several systems for a deeper study. In the next section, examples of CaH_2 + *M* systems with *M*: Zinc, Tin and Lead are used as examples of thermodynamic prediction due to their affordable price. Those systems are detailed below to explain the methodology. For further details concerning the theoretical study, please refer to the appendix.

3.3.1. xCaH$_2$ + yZn

According to The Mineral Resources Program (MRP) that supports data collection prices[61], the zinc price has an average price since 2013 of US$2.348 kg^{-1} and a world production of ≈13,000 tons per year, which make it an interesting candidate for our application. On the other hand, the melting point of Zn is ≈420 °C and molten materials can cause engineering issues for the container. Also, the molar mass of zinc (MM_{Zn} = 65.37 kg·mol^{-1}) is significant, which makes the maximum H_2 capacity in this case limited.

Thermodynamic values for the Ca-Zn phases were taken from Spencer *et al.*[16] and values for the elements, α-Ca (FCC), β-Ca (BCC) and Zn (HCP), where taken from Dinsdale *et al.*[51] The phase diagram (Figure A-1 in appendix) shows 8 different compounds between calcium and zinc.

Table 3-3 reports the possible reactions between xCaH$_2$ and yZn or Ca$_x$Zn$_y$ compound resulting in the formation of Ca$_x$Zn$_y$ and the release of hydrogen (equilibrium composition on figure A-2).

Table 3-3: Temperature of reaction, enthalpy per mole of hydrogen and H_2 wt % desorbed for every possible reaction for the CaH_2-Zn system.

	Possible reactions between CaH_2 &:	$T_{(1\ bar)}$ (°C)	ΔH (kJ·mol^{-1}·H_2)	H_2 wt %
	Zn			
1	$3CaH_2 + Zn \rightleftarrows Ca_3Zn + 3H_2$	1010	152.1	3.16
2	$5CaH_2 + 3Zn \rightleftarrows Ca_5Zn_3 + 5H_2$	940	148.0	2.48
3	$CaH_2 + Zn \rightleftarrows CaZn + H_2$	854	140.3	1.88
4	$CaH_2 + 2Zn \rightleftarrows CaZn_2 + H_2$	626	111.7	1.17
5	$CaH_2 + 3Zn \rightleftarrows CaZn_3 + H_2$	515	96	0.85
6	$CaH_2 + 5Zn \rightleftarrows CaZn_5 + H_2$	267	56.2	0.55
7	$CaH_2 + 11Zn \rightleftarrows CaZn_{11} + H_2$	-1006	-36.3[†]	0.26
8	$CaH_2 + 13Zn \rightleftarrows CaZn_{13} + H_2$	-906	-35.5	0.23
	$CaZn_5$			
9	$14CaH_2 + CaZn_5 \rightleftarrows 5Ca_3Zn + 14H_2$	1053	152.2	2.95
10	$22CaH_2 + 3CaZn_5 \rightleftarrows 5Ca_5Zn_3 + 22H_2$	1014	161.5	2.19
11	$4CaH_2 + CaZn_5 \rightleftarrows 5CaZn + 4H_2$	973	154.5	1.51

[†] Negative values of temperature and enthalpy are indicative of the impossibility of the reaction. This means that the products are always more stable than the reactors.

12	$3CaH_2 + 2CaZn_5 \rightleftarrows 5CaZn_2 + 3H_2$	814	143.2	0.70
13	$2CaH_2+3CaZn_5 \rightleftarrows 5CaZn_3 + 2H_2$	804	143.6	0.34
	$CaZn_{11}$			
14	$32CaH_2 + CaZn_{11} \rightleftarrows 11Ca_3Zn + 32H_2$	1034	151.2	3.06
15	$52CaH_2 + 3CaZn_{11} \rightleftarrows 11Ca_5Zn_3 + 52H_2$	982	158.6	2.35
16	$10CaH_2 + CaZn_{11} \rightleftarrows 11CaZn + 10H_2$	924	151.2	1.71
17	$9CaH_2 + 2CaZn_{11} \rightleftarrows 11CaZn_2 + 9H_2$	757	140.7	0.96
18	$8CaH_2 + 3CaZn_{11} \rightleftarrows 11CaZn_3 + 8H_2$	716	139.2	0.62
19	$6CaH_2+5CaZn_{11} \rightleftarrows 11CaZn_5 + 6H_2$	619	127.9	0.30
	$CaZn_{13}$			
20	$38CaH_2 + CaZn_{13} \rightleftarrows 13Ca_3Zn + 38H_2$	1032	150.3	3.08
21	$62CaH_2 + 3CaZn_{13} \rightleftarrows 13Ca_5Zn_3 + 62H_2$	979	157.1	2.37
22	$12CaH_2 + CaZn_{13} \rightleftarrows 13CaZn + 12H_2$	918	148.0	1.73
23	$11CaH2 + 2CaZn_{13} \rightleftarrows 13CaZn_2 + 11H_2$	744	134.8	0.99
24	$10CaH_2 + 3CaZn_{13} \rightleftarrows 13CaZn_3 + 10H_2$	695	129.5	0.65
25	$8CaH_2 + 5CaZn_{13} \rightleftarrows 13CaZn_5 + 8H_2$	576	114.1	0.34
26	$2CaH_2 + 11CaZn_{13} \rightleftarrows 13CaZn_{11} + 2H_2$	-3545	-40.2	0.04
	$CaZn_3$			
27	$8CaH_2 + CaZn_3 \rightleftarrows 3Ca_3Zn + 8H_2$	1066	153.0	2.81
28	$4CaH_2 + CaZn_3 \rightleftarrows Ca_5Zn_3 + 4H_2$	1035	164.2	0.02
29	$2CaH_2 + CaZn_3 \rightleftarrows 3CaZn + 2H_2$	1008	158.2	0.01
30	$CaH_2 + 2CaZn_3 \rightleftarrows 3CaZn_2 + H_2$	822	142.9	0.00
	$CaZn_2$			
31	$5CaH_2 + CaZn_2 \rightleftarrows 2Ca_3Zn + 5H_2$	1083	154.1	0.03
32	$7CaH_2 + 3CaZn_2 \rightleftarrows 2Ca_5Zn_3 + 7H_2$	1066	168.3	0.02
33	$CaH_2 + CaZn_2 \rightleftarrows 2CaZn + H_2$	1072	165.8	0.01
	CaZn			
34	$2CaH_2 + CaZn \rightleftarrows Ca_3Zn + 2H_2$	1086	158.0	0.02
35	$2CaH_2 + 3CaZn \rightleftarrows Ca_5Zn_3 + 2H_2$	1062	170.3	0.01
	Ca_5Zn_3			
36	$4CaH_2 + Ca_5Zn_3 \rightleftarrows 3Ca_3Zn + 4H_2$	1098	149.4	0.01

In Table 3-3, reactions 7, 8 and also 26 show that $CaZn_{11}$ is stable at room temperature. It means that its formation reaction is not reversible. In Table 3-3, the reaction between CaH_2 and $CaZn_{11}$ compound

that occurs at a temperature under 800 °C is highlighted in green. This reaction occurs between the Zn-richest compounds; $CaZn_{11}$ and $CaZn_5$ hence the H_2 wt % release is at its lowest. According to the phase diagram, $CaZn_5$ and $CaZn_{11}$ melting points are at 695 °C and 724 °C, respectively.[62] Local overheating can cause irreversible degradation in decomposition reactions.

To summarize, this system may be suitable for TES application, however issues such as melted calcium-zinc may be insurmountable. Also, the low H_2 wt % drives to a large quantity of hydrogen to store hence a need in low temperature hydrogen container. Enthalpy of reaction 19 (from Table 3-3) is ≈ 128 $kJ \cdot mol^{-1}$ H_2 which is significant, but for only 0.3 H_2 wt % of hydrogen released. It is shown in section 3.4 that the LTMH quantity is an important factor in the total price, which depends on the H_2 wt % capacity but also on enthalpy per reaction of the HTMH.

3.3.2. *x*CaH_2 + *y*Sn

As for the previous example, the melting point of tin is low (MP_{sn}≈ 230°C). The average price of Tin since 2013 is US$2.06/kg as communicated by The Mineral Resources Program (MRP) that supports data collection prices.[61] The world production is around 290 000 tonnes per year.

The source of data for the Ca-Sn compound formation Gibbs free energies were taken from Ohno *et al.*[63] (and Dinsdale *et al.*[51] for pure tin). The phase diagram (Figure A-3) reports 7 possible phases between Ca and Sn from the poorer to the richer in Ca; $CaSn_3$, CaSn, Ca_7Sn_6, $Ca_{31}Sn_{20}$, $Ca_{36}Sn_{23}$, Ca_5Sn_3 and Ca_2Sn.

Figure 3-6: Equilibrium composition of the Ca-Sn system according to temperature.

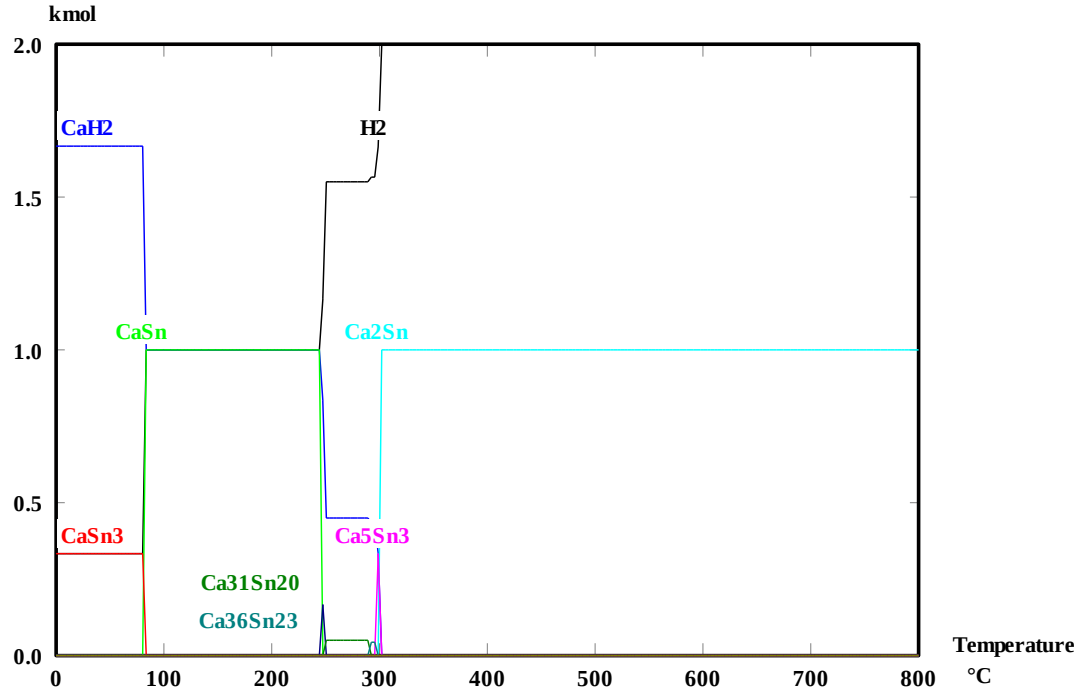

Figure 3-6 is the HSC© software plot of the 2CaH_2 + Sn system equilibrium composition for an initial composition of 2 moles of Sn for 1 mole of CaH_2 at 1 bar. The thermodynamic calculation (Figure A-4) shows that the $CaSn_3$ formation is irreversible. At 77 °C, $CaSn_3$ and CaH_2 form CaSn and H_2 and multiple steps of reaction occurred at T > 300 °C to a final composition of Ca_2Sn for a total hydrogen storage

capacity of 1.99 H_2 wt %. This system requires further investigation for low temperature hydrogen storage applications.

This system may be interesting for hydrogen storage at low temperatures, but due to the high molar mass of Sn (MM_{Sn} = 118.69 kg·mol^{-1}), a low hydrogen storage per kilogram capacity is expected.

3.3.3. *x*CaH_2 + *y*Pb

For the calcium hydride-lead system the theoretical gravimetric hydrogen storage capacity is limited. Indeed, the molar mass of lead is significant*:* MM_{Pb} = 207.19 kg/mol. Price of lead is estimated at US$2.26/kg for a wold production of 4700 tonnes/year. The Ca-Pb system and others had previously been explored by Notin *et al*.[64], and this is the source of the thermodynamic data. Chiboub S. also used this data for his thesis calculations.[65] The phase diagram shows 4 different phases between Ca and Pb: $CaPb_3$, CaPb, Ca_5Pb_3 and Ca_2Pb.

Figure 3-7: Equilibrium composition of the Ca-Pb system according to temperature.

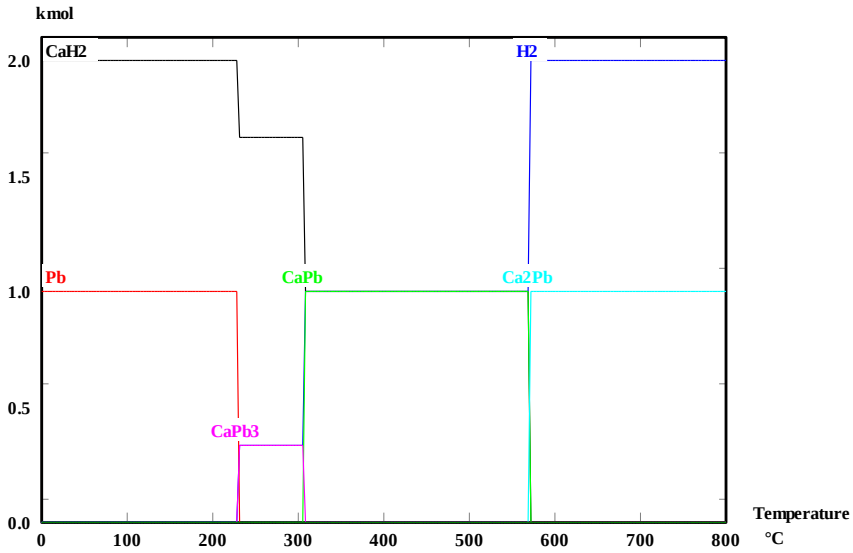

Three reactions are observable on Figure 3-7, occurring below 800 °C. The last phase observed obtains the Ca-richest phase: Ca_2Pb for a total desorbed H_2 wt % of 1.38.

- $CaH_2 + 3Pb \rightleftarrows CaPb_3 + H_2$ → T_{1bar}= 230 °C, $\Delta H \approx 46.9$ kJ·mol^{-1} H_2
- $2CaH_2 + CaPb_3 \rightleftarrows 3CaPb + 2H_2$ → T_{1bar}= 306 °C , $\Delta H \approx 74.5$ kJ·mol^{-1} H_2
- $CaH_2 + CaPb \rightleftarrows Ca_2Pb + H_2$ → T_{1bar}= 557 °C, $\Delta H \approx 101.7$ kJ·mol^{-1} H_2

3.3.4. Conclusions on the thermodynamic predictions

Table 3-1 compiles the selection of systems where the references have been cross-checked in order to determine accurate values for *ΔH*, *ΔS* and *ΔG.* According to this theoretical analysis, three systems have been selected for experimental analysis. The thermodynamic prediction and their experimental analysis are described in the following chapters (Chapters 4, 5 and 6). Based on this calculation, a Pressure-Temperature curve can be drawn as shown on Figure 3-8, with the example of CaH_2 + Si system. According to this data, a preferential pattern of reaction can be defined for the pressure and temperature condition required to obtain a certain compound.

From this table, it can be defined which metal is the most promising to destabilise CaH_2. Indeed, when a possible reaction is in the required range of temperature or close to 600 °C < *T* < 800 °C and has a high enthalpy of reaction, it can be considered as a good candidate. The most important parameter to take into account is the gravimetric heat storage capacity, which is defined as:

$$Gravimetric\ heat\ storage\ capacity = \frac{n_{H_2} \cdot \Delta H}{MM_{\ reactant}} \qquad \text{Equation 3-14}$$

Where ΔH is the enthalpy of the reaction per mole of H_2, n_{H_2} is the number of moles desorbed, and $MM_{reactant}$ is the molar mass of the initial composition. This last factor is dependent on the molar mass of the metal used for destabilisation:MM_m. It is also considered if the condition of temperature and pressure as shown on Figure 3-8 are manageable for application. In fact, for a temperature between 600 °C and 800 °C, the pressure doesn't have to be too high. If a material is considered interesting because of a high gravimetric capacity but under high pressure condition, the use of a compressor may be required. For a first selection, it has been defined arbitrarily that the pressure cannot be higher than 50 bar as shown in the red square in Figure 3-8 below. On this figure, the lines represent the equilibrium condition of relative reactions. Above these lines is the unreacted material or compound. Below these lines is the compound formed after reaction. This compound may react with CaH_2 at higher pressure or temperature to form the next phase. In this case the enthalpy of the multiple reactions can be added up if they can match the required conditions of pressure and temperature. The reactions CaH_2+Si ⇄ $CaSi_2$ +H_2 and CaH_2+2$CaSi_2$ ⇄ Ca_3Si_4 + H_2 are excluded because they are expected to occur at too low a temperature, and/or at too high a pressure while the reaction CaH_2 + Ca_5Si_3 ⇄ 3Ca_2Si + H_2 is expected to occur at too high a temperature or under high vacuum condition. The subtlety of this system is that the operating temperature must be 703 °C or higher because the T_{1bar} of the principal reaction: 2CaH_2+3CaSi ⇄ Ca_5Si_3+2H_2 is 703°C. If the operating

temperature is lower, the system would need a compressor for pressure and a vacuum pump for the reaction occurring below the atmospheric pressure. It is shown on Figure 3-8 that the 703 °C equilibrium pressure of reaction $CaH_2+2CaSi_2 \rightleftarrows Ca_3Si_4 + H_2$ is over the 20 bar limit. To summarize this example:

- 5 steps of desorption are possible between CaH_2, Si and the calcium silicide compound.
- $CaH_2 + Ca_5Si_3 \rightleftarrows 3Ca_2Si + H_2$. Ca_2Si forms at too high a temperature or too low a pressure.
- $CaH_2+Si \rightleftarrows CaSi_2 +H_2$. $CaSi_2$ is forms at a low temperature, but for TES applications cycling this reaction is excluded, because it needs a high-pressure condition in the required temperature range.
- Between 600 °C and 800 °C, the conditions of pressure are obeyed for 2 reactions: $CaH_2+Ca_3Si_4 \rightleftarrows 4CaSi + H_2$ and $2CaH_2+3CaSi \rightleftarrows Ca_5Si_3+2H_2$

In the next section it is shown that the raw material cost is not such a significant factor in the total cost, however the price of an expensive raw material, such as silver, can be insurmountable. Then, as said in section 3.3.1, it is important to know the phase diagram of the Ca-*M* system in order to consider the raw material melting point (MP) or compound eutectic point (EP). Above these points parts of the material become liquid, which changes the final predicted composition and can cause engineering issues.

Figure 3-8: Theoretical Pressure-Temperature curve for Ca-Si system.

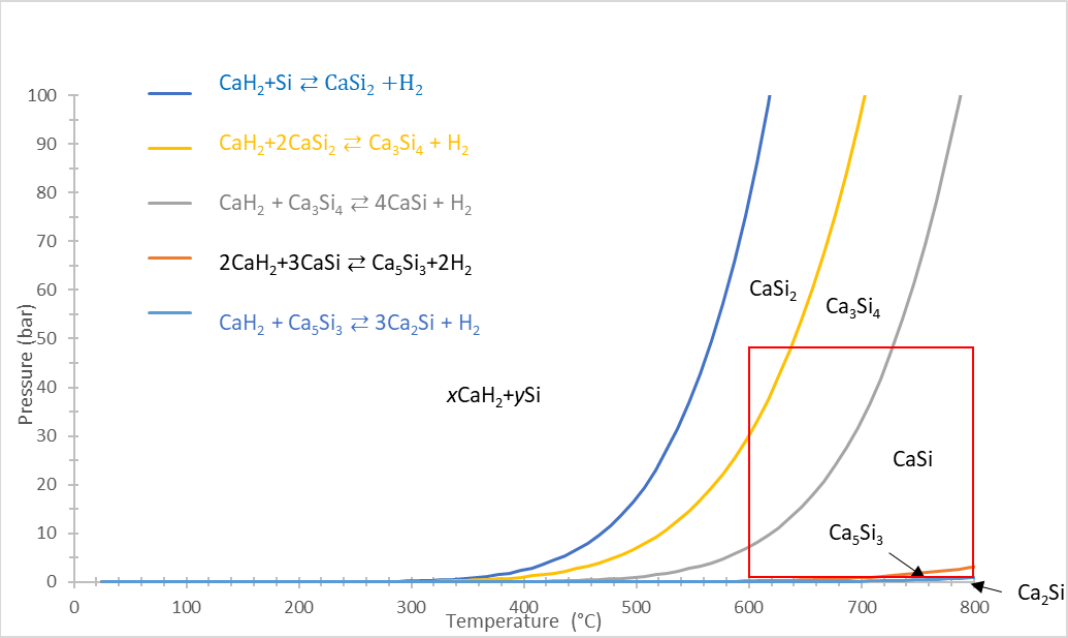

Table 3-4: Summary of thermodynamic values for different CaH_2 + M system for all the possible reactions between the raw material and intermediate compound, including the operating temperature at 1 bar pressure, the enthalpy of reaction at this temperature, operating pressure at 600 °C, gravimetric energy and a possible limiting condition.

M	Possible reaction at 25 °C < T < 800 °C range	$T_{(1bar)}$	H_2 wt %	ΔH (kJ·mol^{-1} H_2)	P at 600 °C (bar)	Grav. Energy kJ·kg^{-1}	Comment or limiting condition	Source of data
Pb	$CaH_2 + 3Pb \rightleftarrows CaPb_3 + H_2$	230	0.3	47	110	71	MP(Pb)=327°C	51, 64
	$2CaH_2 + CaPb_3 \rightleftarrows 3CaPb+2H_2$	306	0.54	74.5	173	200	EP(CaP_3)=635°C	
	$CaH_2 + CaPb \rightleftarrows Ca2Pb+H_2$	557	0.7	102.5	1.9	354	EP(CaPb)=557°C	
Ag‡	$2CaH_2+9Ag \rightleftarrows Ca_2Ag_9+2H_2$	394	0.38	85.2	35	162	MP(CaH_2)= 983°C	51, 64
	$4CaH_2+7Ca_2Ag_9 \rightleftarrows 9Ca_2Ag_7+4H_2$	434	0.11	115.3	13.7	61	EP(Ca_2Ag_9)=652°C	
	$3CaH_2+2Ca_2Ag_7 \rightleftarrows 7CaAg_2+3H_2$	750	0.34	132.6	0.06	221	EP(Ca_2Ag_7)=687°C	
Zn	$6CaH_2+5CaZn_{11} \rightleftarrows 11CaZn_5+6H_2$	619	0.3	133.7	0.6	198	EP($CaZn_{11}$)=620°C	51, 66
Sn	$2CaH_2 + CaSn_3 \rightleftarrows 3CaSn + 2H_2$	77	0.84	35.8	1377	149	EP($CaSn_3$)=628°C	51, 63
	$2CaH_2 + 3CaSn \rightleftarrows Ca_5Sn_3 + 2H_2$	247	0.72	42.4	45.5	151	MP(CaH_2)= 983°C	
	$CaH_2+Ca_5Sn_3 \rightleftarrows 3Ca_2Sn+H_2$	297	0.34	42.4	20	71	MP(CaH_2)= 983°C	
B§	$CaH2 + 6B \rightleftarrows CaB_6 + H_2$	230	1.88	55.5	250	519	MP(CaH_2)= 983°C	17, 51
Si**	$CaH_2+2Si=CaSi_2+H_2$	360	2.05	83.4	75	849	MP(CaH_2)= 983°C	51, 67
	$CaH_2+2CaSi_2 \rightleftarrows Ca_3Si_4 + H_2$	397	0.86	81.2	29	346	MP(CaH_2)= 983°C	
	$CaH_2 + Ca_3Si_4 \rightleftarrows 4CaSi + H_2$	498	0.73	107.5	6.8	391	MP(CaH_2)= 983°C	
	$2CaH_2+3CaSi \rightleftarrows Ca_5Si_3+2H_2$	707	1.4	107.3	0.2	743	MP(CaH_2)= 983°C	
Al	$CaH_2+4Al \rightleftarrows Al_4Ca+H_2$	420	1.06	74.2	13.7	390	MP(Al)= 660°C	51, 59
	$CaH_2+Al_4Ca \rightleftarrows 2Al_2Ca+H_2$	489	1.06	82.3	5.2	433	EP(Al_4Ca)= 700°C	
C††	$CaH2 + 2C \rightleftarrows CaC_2 + H_2$	495	3.05	125.9	20.5	1904	MP(CaH_2)= 983°C	51, 57
MgO ‡‡	$CaH_2 + MgO \rightleftarrows CaO + Mg + H_2$	787	2.45	149.5	0.02	1814	Vapour pressure of Mg at 600°C=1.2x10^{-3} bar	51, 68

‡ Figures A- 7 to A- 9 in appendix
§ Figures A- 10 to A- 11 in appendix
** Figure A- 12 in appendix
†† Figures A- 13 to A- 14 in appendix
‡‡ Figures A- 15 in appendix

Energy released by one or multiple steps of reaction in kJ·kg^{-1} (Table 3-4) is a good indication to calculate the total cost of a TES using this material as a HTMH. Three systems stand out:

- CaH_2-Si system. Multiple steps of reaction with high energy storage released by reaction; $2CaH_2 + 3CaSi \rightleftarrows Ca_5Si_3 + 2H_2$ specifically, theoretically occurs at a temperature between 600 °C and 800 °C for pressure of ≈ 1 bar.
- CaH_2 + 2C system. This system has the highest theoretical heat storage capacity.
- CaH_2 + MgO. This system has a high energy releasing capacity for a high temperature of reaction. It is interesting due to its temperature of reaction and a high enthalpy of reaction.

To complete this comparative study, the cost of each joule stored and released by each system is evaluated. This depends on the gravimetric heat storage capacity, but also on the raw material price and the number of moles of hydrogen required.

3.4. Cost calculation

The DOE Sunshot vision released specific technical targets for the CST TES systems[2] and reported a TES specific cost lower than 15US$·kWh^{-1}.

The study of the HTMH/LTMH system cost has been done previously by Corgnale *et al.*[23] and Sheppard *et al.*[69] In order to provide a comparison, a cost in US$ per kilowatt hour thermal produced per reaction was defined. The cost of the HTMH is calculated based on the cost of the raw material and the theoretical gravimetric heat storage capacity (see Table 3-4).

3.4.1. Principle

Firstly, the price of raw is defined material which for calcium and hydrogen[26] is estimated at US$2.54 and US$2.5 per kilogram, respectively. This price is defined per kg as the weight ratio of each element multiplied by their price as defined in Equation 3-15, where n_x, is the number of moles per reaction, MM_x is the molar mass, $\$_x$ is the price of each element per kilogram and $MM_{reactant}$ is the molar mass of the initial composition of reactant.

$$Price\ of\ reactant\ \left(\frac{US\$}{kg}\right) = \frac{n_{Ca}.MM_{Ca}}{\rho_{reactant}} \cdot \$_{Ca} + \frac{n_M.MM_M}{\rho_{reactant}} \cdot \$_M + \frac{n_{H_2}.MM_{H_2}}{\rho_{reactant}} \cdot \$_{H_2} \quad \text{Equation 3-15}$$

Using the gravimetric heat storage capacity and the thermodynamics evaluated in Table 3-4, the comparative HTMH specific cost for each $x\mathrm{CaH_2} + yM$ composition is calculated from Equation 3-16.

$$\text{HTMH specific cost } \left(\frac{US\$}{kWh}\right) = \frac{Price\ of\ reactant\ \left(\frac{US\$}{kg}\right)}{gravimetric\ heat\ storage\ capacity\ \left(\frac{kJ}{kg}\right)\cdot 3600} \qquad \text{Equation 3-16}$$

Table 3-5: Comparative table of the cost of different systems studied.

Initial composition	Cost of raw material per kg of RXN (US$·kg^{-1})	Steps of reaction	Theoretical H_2 wt %	Theoretical Thermal Storage per reaction (kJ·kg^{-1})	Cumulative Theoretical Thermal Storage per reaction (kJ·kg^{-1})	Theoretical Volumetric Storage (kJ·l^{-1})	Cost US $·kWh^{-1} thermal	Mass of H_2 Required (ton) *
CaH_2 + 2Pb	2.34	CaH_2 + 3Pb ⇄ $CaPb_3$ + H_2	0.23	161	350	1636	**24.07**	100
		$2CaH_2$ + $CaPb_3$ ⇄ 3CaPb+$2H_2$	0.69	254				
		CaH_2 + CaPb ⇄ Ca_2Pb+H_2	1.38	350				
$2CaH_2$ + 7Ag	501.3	$2CaH_2$+9Ag ⇄ Ca_2Ag_9+$2H_2$	0.35	47	219	1328	**8224.9**	77
		$4CaH_2$ + $7Ca_2Ag_9$ ⇄ $9Ca_2Ag_7$+$4H_2$	0.10	64				
		$3CaH_2$ + $2Ca_2Ag_7$ ⇄ $7CaAg_2$+$3H_2$	0.34	73				
CaH_2 + 5Zn	2.37	$6CaH_2$+$5CaZn_{11}$ ⇄ $11CaZn_5$+$6H_2$	0.30	33	198	1077	**43.07**	76
$2CaH_2$ + Sn	2.26	$2CaH_2$ + $CaSn_3$ ⇄ 3CaSn + $2H_2$	0.66	59	252	847	**32.28**	242
		$2CaH_2$ + 3CaSn ⇄ Ca_5Sn_3 + $2H_2$	0.55	69				
		CaH_2+Ca_5Sn_3 ⇄ $3Ca_2Sn$+H_2	0.66	69				
CaH_2 + 6B	1.63	CaH_2 + 6B ⇄ CaB_6 + H_2	1.35	376	376	1307.4	**15.61**	181
$5CaH_2$ + 3Si	2.39	CaH_2+2Si ⇄ $CaSi_2$+H_2	1.03	283	996	2007	**8.62**	69
		CaH_2+2$CaSi_2$ ⇄ Ca_3Si_4 + H_2	0.51	275				
		CaH_2 + Ca_3Si_4 ⇄ 4CaSi + H_2	0.51	365				
		$2CaH_2$+3CaSi ⇄ Ca_5Si_3+$2H_2$	1.37	361				
CaH_2 + 2Al	2.10	CaH_2+4Al ⇄ Al_4Ca+H_2	1.05	386	815	1895	**9.29**	130
		CaH_2+Al_4Ca ⇄ $2Al_2Ca$+H_2	1.05	428				
CaH_2 + 2C	1.77	CaH_2 + 2C ⇄ CaC_2 + H_2	3.05	1904	1904	5314	**3.34**	57
CaH_2 + MgO	0.87	CaH_2 + MgO ⇄ CaO + Mg + H_2	2.45	1814	1814	4450	**1.72**	68

* For a 200 MW CST plant with 7 hours of thermal storage

In Table 3-5, the reactions highlighted in red do not comply with the TES required conditions (600 °C < T < 800 °C and 1 bar < P < 20 bar) and their enthalpy of reaction is excluded from the cumulated theoretical thermal storage capacity. Also, the theoretical volumetric energy density of each system in $kJ \cdot l^{-1}$ has been calculated. The higher this value is, the lower the volume of high temperature metal hydride required, which makes a system such as $CaH_2 + 2C$, an interesting candidate. The costs of the raw materials are derived from the U.S. Geological Survey National Minerals Information Centre or Argus Metal Price.[26] In order to have a complete study of the TES cost, the cost of the Low-Temperature Metal Hydride (LTMH) is also required. Savannah River National Laboratory (SRNL) is focusing its research on low-temperature metal hydride costs. Sheppard *et al.*[24]. showed that the cost of the LTMH is the most important factor in the total price. This value depends directly on the mass of Hydrogen required to be stored.

3.5. Conclusion

It is observed that four systems are compatible with the DOE Sunshot vision: $5CaH_2 + 3Si$, $CaH_2 + 2Al$, $CaH_2 + 2C$ and CaH_2+MgO. It's important to keep in mind that this list is not exhaustive. An important literature review has been conducted, but other systems may be identified in the future. It is also important to remember that those calculations were based on theoretical values. Experimentation might confirm or refute these values. Those cost estimations were updated and corrected using experimental values obtained with the results gathered during this study and detailed in the following chapters.

According to these preliminary calculations, during this thesis, researches were focused on the following systems that are further described in the next chapters:

- $x CaH_2 + y Si$: a multi-step reaction system using silicon which is a material abundant and affordable
- $CaH_2 + 2C$: has the one of the highest enthalpies of reaction of all the systems compared in this chapter.
- CaH_2 + MgO: a promising system as magnesium hydride is the most known of all the hydrides systems. The starting material can be CaO and MgH_2 which give a very low price.

4. The xCaH$_2$ + ySi system

4.1. Background and Thermodynamic prediction

The oldest study found on the reaction between calcium hydride and silicon was by Wohler *et al.*[70]. It was observed that the hydrided calcium reacted with silicon at a lower temperature than pure calcium. Co-melting of calcium and silicon in air formed calcium carbide in a stainless-steel reactor at high temperature. Hydriding calcium before the reaction conduct to the formation of a calcium silicide and avoided the formation of calcium carbide instead. It was revealed that calcium disilicide $CaSi_2$ formation is thermodynamically preferable and the addition of extra CaH_2 caused a second step of the reaction resulting in the formation of a CaSi phase. First calcium disilicide is formed by reacting CaH_2 with Si. $CaSi_2$ then reacts with the excess calcium hydride to form CaSi.

$$CaH_2 + Si \rightleftarrows CaSi_2 + H_2 \qquad \text{(reaction 4-1)}$$

$$CaSi_2 + CaH_2 \rightleftarrows CaSi + H_2 \qquad \text{(reaction 4-2)}$$

Knowing this fact, thermodynamic predictions have been undertaken considering all the possible reactions between calcium hydride (see chapter 3 for details and equations), silicon and every possible Ca_xSi_y compound existing in the phase diagram.

Figure 4-1: Phase diagram of the Ca-Si system.[71]

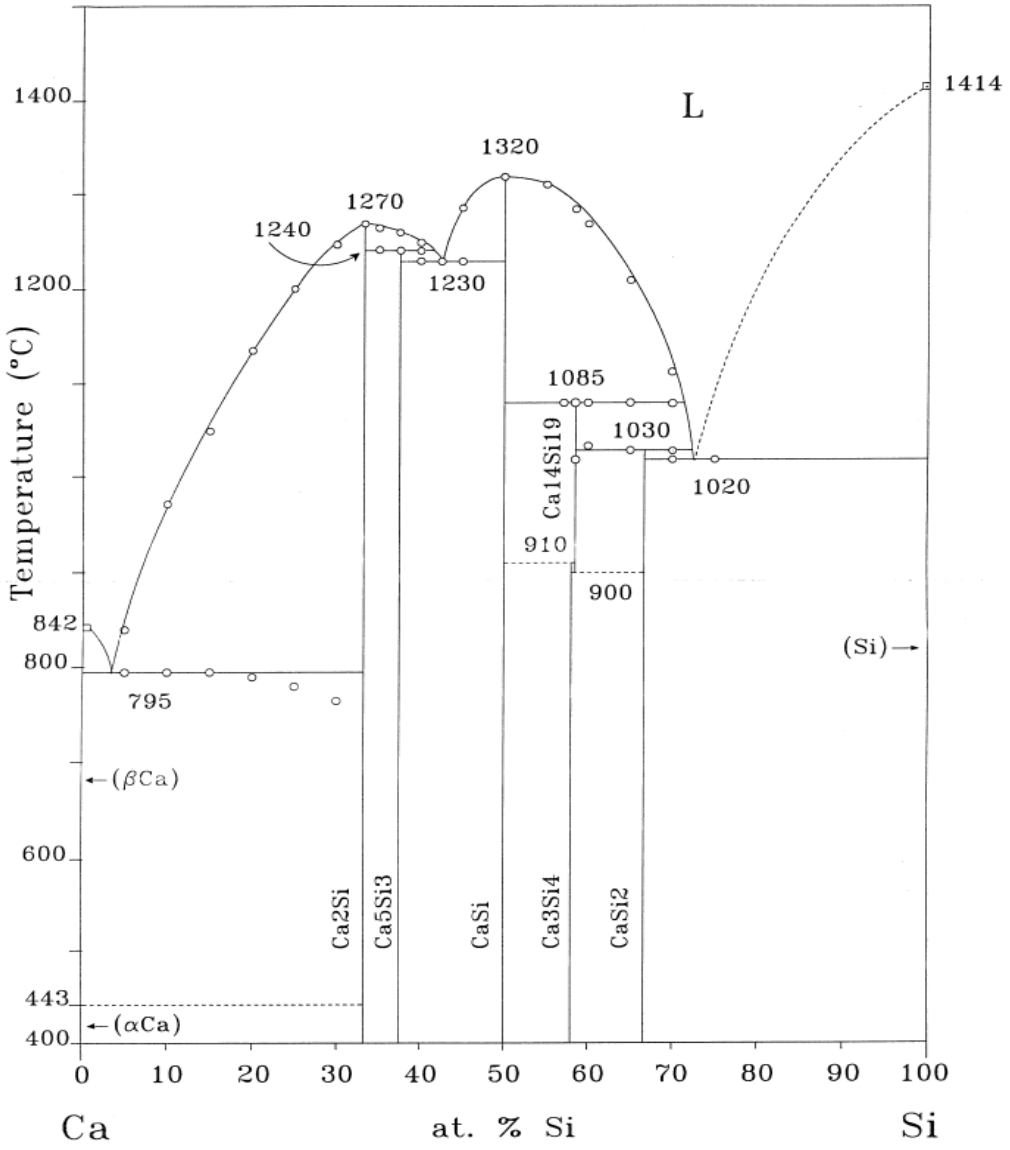

The phase diagram[71] (Figure 4-1) shows 6 different structures of Ca_xSi_y from the poorest in calcium $CaSi_2$ to the richest, Ca_2Si. Some interesting points from this article include:

- The $Ca_{14}Si_{19}$ phase is not stable at room Temperature. This phase exists only at a temperature between 900 °C and 1085 °C.
- It was possible to obtain the Ca_3Si_4 only by quenching the material after 3 - 4 weeks of annealing
- A possible cubic phase richer in Ca than Ca_2Si that has been reporter by older research is not visible in this reference. [72]

Table 4-1 : Thermodynamic calculations for the CaH_2-Si system. Temperature of reaction at 1 bar equilibrium pressure, number of moles of hydrogen released by reaction, enthalpy per mole of hydrogen, heat capacity and weight percent of H_2 released by reaction.

	Si	T_{1Bar} (°C)	Enthalpy (kJ·mol^{-1} H_2)	Heat capacity (kJ·kg^{-1}) at T_{RXN}	H_2 wt %
1	$CaH_2 + Si \rightleftarrows CaSi + H_2$	413	89.3	1272	2.87
2	$CaH_2 + 2Si \rightleftarrows CaSi_2 + H_2$	370	83.4	849	2.05
3	$2CaH_2 + Si \rightleftarrows Ca_2Si + 2H_2$	571	103.9	1852	3.59
4	$3CaH_2 + 4Si \rightleftarrows Ca_3Si_4 + 3H_2$	381	82.7	1040	2.53
5	$5CaH_2 + 3Si \rightleftarrows Ca_5Si_3 + 5H_2$	520	96	1629	3.42
6	$14CaH_2 + 19Si \rightleftarrows Ca_{14}Si_{19} + 14H_2$	391	85.8	1070	2.51
	$CaSi_2$				
7	$CaH_2 + CaSi_2 \rightleftarrows 2CaSi + H_2$	455	94	680	1.46
8	$3CaH_2 + CaSi_2 \rightleftarrows 2Ca_2Si + 3H_2$	640	110.6	1518	2.72
9	$CaH_2 + 2CaSi_2 \rightleftarrows Ca_3Si_4 + H_2$	405	81.2	346	0.86
10	$7CaH_2 + 3CaSi_2 \rightleftarrows 2Ca_5Si_3 + 7H_2$	587	101.4	1217	2.42
11	$9CaH_2 + 19CaSi_2 \rightleftarrows 2Ca_{14}Si_{19} + 9H_2$	435	90.8	370	0.82
	Ca_3Si_4				
12	$CaH_2 + Ca_3Si_4 \rightleftarrows 4CaSi + H_2$	496	107.5	391	0.73
13	$5CaH_2 + Ca_3Si_4 \rightleftarrows 4Ca_2Si + 5H_2$	684	116.3	1313	2.28
14	$11CaH_2 + 3Ca_3Si_4 \rightleftarrows 4Ca_5Si_3 + 11H_2$	636	106.8	1012	1.91
	CaSi				
15	$CaH_2 + CaSi \rightleftarrows Ca_2Si + H_2$	741	118.4	1074.1	1.83
16	$2CaH_2 + 3CaSi \rightleftarrows Ca_5Si_3 + 2H_2$	703	106.5	737.7	1.40
	Ca_5Si_3				
17	$CaH_2 + Ca_5Si_3 \rightleftarrows 3Ca_2Si + H_2$	803	142.3	436	0.62
	$Ca_{14}Si_{19}$				
18	$5CaH_2 + Ca_{14}Si_{19} \rightleftarrows 19CaSi + 5H_2$	471	97.7	374	0.77
19	$24CaH_2 + Ca_{14}Si_{19} \rightleftarrows 19Ca_2Si + 24H_2$	679	114.2	1302	2.30
20	$CaH_2 + 4Ca_{14}Si_{19} \rightleftarrows 19Ca_3Si_4 + H_2$	-90	-90.4	-20	0.05
21	$53CaH_2 + 3Ca_{14}Si_{19} \rightleftarrows 19Ca_5Si_3 + 53H_2$	629	104.1	1000	1.94

As shown in Chapter 3, to calculate the thermodynamic predictions of the CaH_2-Si system, H_f^0 , S_f^0 and the temperature function of C_p of every possible reactant are required. This data was collected by Heyrman *et al.*[67] for all possible temperature ranges. The results of this calculation are shown in Table 4-1. From these calculations, a preferential scheme of reaction can be drawn (Figure 4-2). This figure is based on the equilibrium composition of the system according to the temperature (Figure A-12):

Figure 4-2: preferential scheme of reactions between CaH_2 and Si.

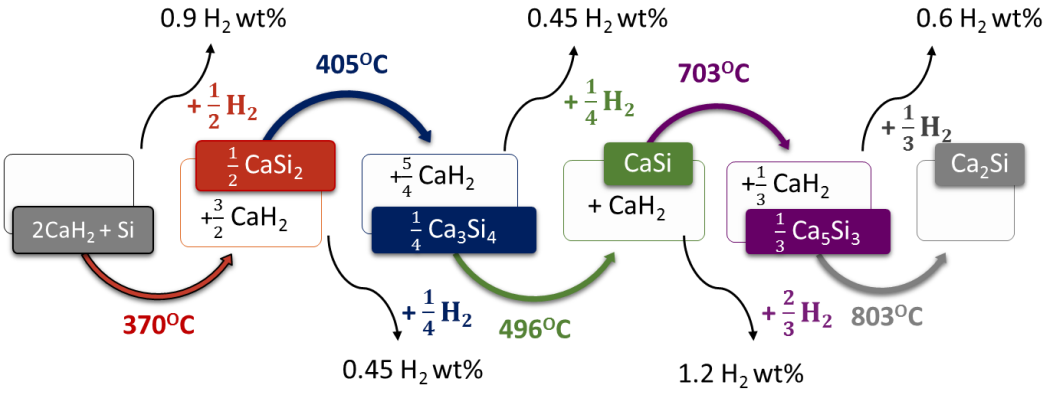

Figure 4.2 is based on the following observations:

- $CaSi_2$ (reaction 2 from Table 3-1) is the most preferable phase that calcium hydride and silicon form together. It can be deducted by comparing the T_{1bar} i.e. the temperature at 1 bar equilibrium pressure and the enthalpy of reaction. Indeed, the lower these values are the lower quantity of energy is needed in order to obtain this reaction.
- $CaSi_2$ is the most Si rich phase possible. Additional silicon would only allow a mixture of $x CaSi_2$ + ySi.
- On the other hand, adding CaH_2 to $CaSi_2$ would allow a second step of reaction to occur with the formation of Ca_3Si_4 (reaction 9 from Table 3-1).
- The same behaviour occurs for Ca_3Si_4 and extra CaH_2 with a third step of reaction to form CaSi: reaction 12 from Table 3-1.
- Reaction 16 from Table 3-1 between CaSi and CaH_2 is predicted to occur for 1 bar at 703 °C to form Ca_5Si_3 phase.
- Finally, the Ca-richer phase can be created at high temperature (803 °C for 1bar): Ca_2Si (reaction 17 from Table 3-1).

This scheme of reaction is visible in Figure 4-2 with the quantity of hydrogen desorbed step by step for an initial composition of $2CaH_2$ + Si.

Having those predictions one side and the examples of hydrogen desorption by calcium silicide phase from the literature on the other side, some results can be anticipated and corroborated by experimentation. For example, Armbruster *et al.*[72] revealed two different temperatures for hydrogenation of a CaSi structure. Wu *et al.*[73] described that the $Ca_5Si_3H_x$ structure decompose into

CaSi, CaH_2 and an amorphous hydride phase at high temperature under 1 bar at 600 °C. This decomposition is considered as an issue for hydrogen storage in a Ca_5Si_3 structure but is particularly interesting as a thermochemical reaction for thermal energy storage at high temperature. The interest for this system for TES application is based on this possible reaction of decomposition. In the followings sections, these predictions will be compared with experimental results using different stoichiometry with the aim to obtain a complete investigation of every possible reaction between CaH_2 and Si or every possible Ca_xSi_y phases.

4.2. Experimental

4.2.1. Material synthesis

Based on the work of H.Wu *et al.*[73],that shows a possible hydrogen absorption and desorption cycling of the Ca_5Si_3 phase and confirmed by thermodynamic prediction, a stoichiometry of 5 moles of CaH_2 for 3 moles of Si was chosen as a starting material for the first experiment. Indeed, the formation of the Ca_5Si_3 phase is predicted to form in the required range of temperature for the second generation of TES (between 600 °C and 800 °C).

The samples were prepared by using a 2 g batch with a ratio of 5 moles of CaH_2 (or 0.572 g: 71.4 wt %) and 3 moles of Si (or 1.428 g: 28.6 wt %) ball milled with 40 g of stainless-steel balls (8 ball 10 mm Ø + 8 balls 6 mm Ø). A percentage of the calcium hydride is oxidised as shown in Figure 4-3 because the purity of the CaH_2 provided by Sigma Aldrich® is 95 wt %; up to 5 wt % of CaO is expected.

Figure 4-3: X-ray diffraction (XRD) pattern (Bruker D8 A) of the ball-milled mixture of 5 moles of CaH_2 and 3 moles of Si. Pattern fitting was achieved using the Rietveld method in the Topas® software package using a fundamental parameters approach.

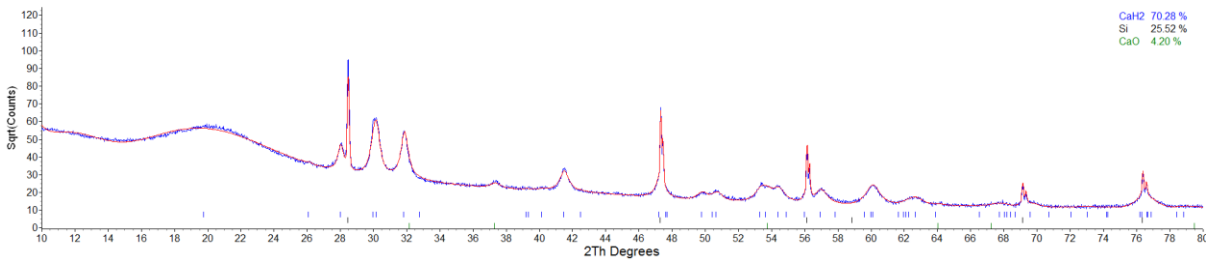

4.2.2. Sorption analysis: Temperature Programmed Desorption (TPD)

4.2.2.1. Initial TPD: problem with oxidation

A TPD analysis was conducted at a temperature ramp of 5 °C/min up to 700 °C followed by a plateau of 3 hours. A starting primary vacuum was settled in a closed system then the pressure was measured during the temperature ramp. During the plateau, the pressure stabilised and that revealed the gas releasing reached its maximum. This experiment showed that the pressure started to rise at 100 °C to obtain the equivalent of a total of 3.6 H_2 wt % (Figure 4-4). As a reminder, the theoretical H_2 wt % of a $5CaH_2 + 3Si$ initial mixture is 3.42 wt %. Indeed, a part of the measured gas release is due to the release of the moisture. Typically, sample containing water or moisture releases gas at approximately 100 °C.

Figure 4-4: Temperature Programmed Desorption results for $5CaH_2 + 3Si$. Evolution of hydrogen weight percent for a temperature ramp of 5 °C/min up to 700 °C followed by a 3 hours plateau.

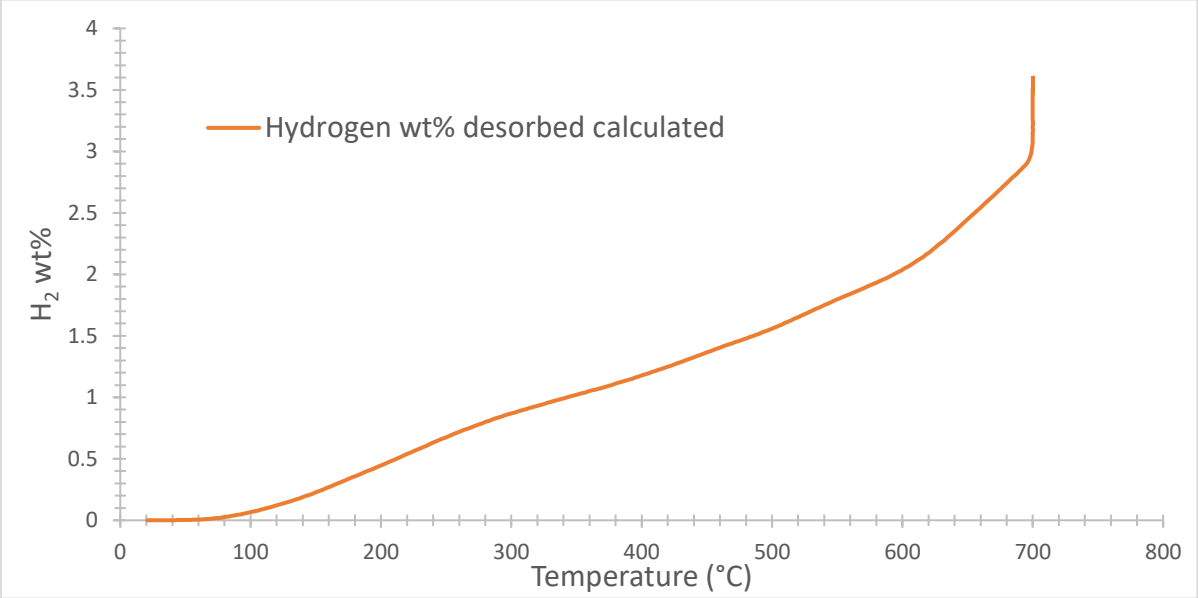

Quantification of the X-ray diffraction data (not shown here) presented a quantity of oxide; CaO ≈ 41 wt %. After the desorption experiment, it has been observed that the sample cell was rusty. It may explain the pressure rise at 100°C. Moisture in a sample cell drives water evaporation at T ≥ 100 °C and the formation of calcium hydroxide phase $Ca(OH)_2$. The decomposition of this phase releases gases at approximately 220 °C (see section 4.2.4 for more details). The equivalent gas wt % released

during this oxidation reaction is included in the total H_2 wt % calculated. This explains a calculated H_2 wt % value higher than the theoretical[§§].

X-ray analysis after the TPD experiment has shown, as expected, that a Ca_5Si_3 (*I4/mcm* space group) structure is formed, but a CaSi (*Amma* space group) phase is also formed and it turns out to be the predominant phase.

2 suggestions can be made based on this experiment and the theoretical predictions:

- CaH_2 is a limiting reagent
- The remaining CaSi due to the lack of CaH_2 oxidation limits the quantity of reacting CaH_2 and the reaction between CaH_2 and CaSi.

This experiment was repeated before changing the sample canister for the next set of experiment.

4.2.2.2. Second experimentation: observation of equilibrium pressure

The hypothesis that the oxidation is limiting the reaction between CaSi and CaH_2 has been confirmed by the following TPD (Figure 4-5). The weight percent of CaO measured by the quantification of the X-ray diffraction data after TPD is lower (around 17 wt %) and a higher quantity of Ca_5Si_3 (≈ 60 wt %) results from this experiment.

The pressure is stabilised at 0.71 bar in the plateau region. A practical H_2 wt % of 2.57 was measured. The formation of the Ca_5Si_3 phase is not complete, CaH_2 Si and CaSi left after the TPD is observed by X-ray analysis (Figure 4-6). A certain quantity of calcium hydride and silicon did not react. According to the thermodynamic prediction, the equilibrium pressure of the Ca_5Si_3 formation reaction at 700 °C is ≈ 0.96 bar (Table 4-2) for reaction 16 of Table 4-1 In the closed system. Due to the pressure rise the equilibrium condition of pressure and temperature was reached before all the reagents were consumed. An efficiency of 75 % has been calculated using equation 4-1 ($\frac{2.57}{3.42}$) . This result was in agreement with the X-ray pattern quantitative analysis; 60 wt % of Ca_5Si_3 plus 15 wt % of CaSi were formed. 75 wt % of products of reaction have been calculated, the leftovers are reactant or oxide that didn't react.

[§§] Indeed, the pressure rise is converted into weight percent of hydrogen on the total weight of initial material thanks to the gas law in a well-known volume. It supposes that all the gas released is only hydrogen.

$$efficiency = \frac{Practical\ H_2\ wt\%}{Theoretical\ H_2 wt\%} \qquad \text{Equation 4-1}$$

This result shows consistency with the prediction. At 700°C, the thermodynamic calculation predicts that the CaSi phase formed at a low temperature is reacting with CaH_2 to form Ca_5Si_3. The following section will confirm or refute the path of reaction (Figure 4-2). Indeed, the total weight percent desorbed at 700 °C fit agrees with prediction, but the multiple step reaction needs to be confirmed.

Figure 4-5: Evolution of pressure (red line) and Temperature (blue line) through the time (in hours) during a TPD ramp on $5CaH_2 + 3Si$. (5 °C/min up to 700 °C followed by a 2h plateau).

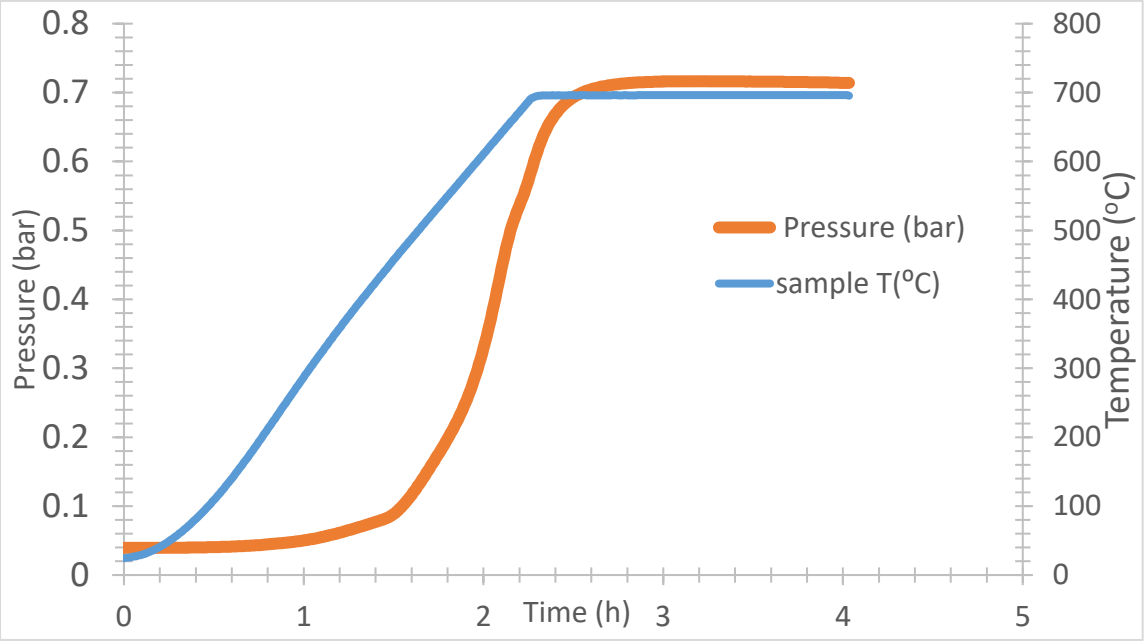

Figure 4-6: Rietveld refinement on Topas© of X-ray diffraction (XRD) pattern (D8A) of the mixture of 5 moles of CaH_2 and 3 moles of Si after TPD measurement (5 °C/min up to 700 °C and 1h plateau).

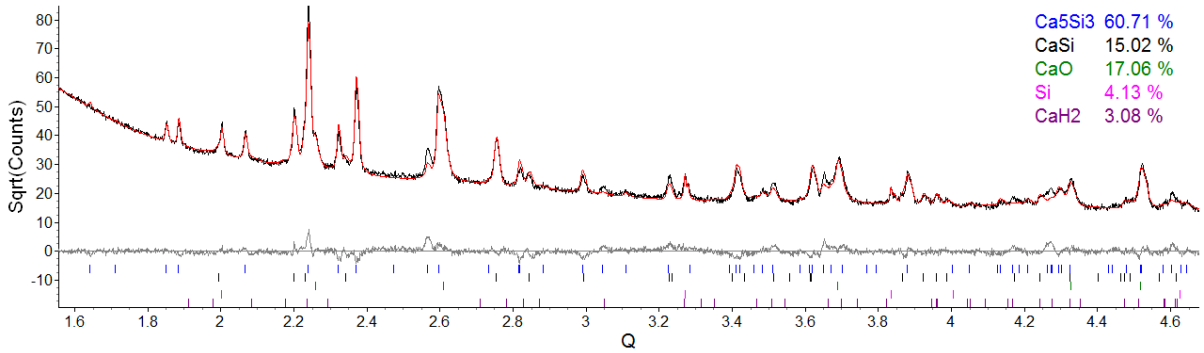

Table 4-2: Prediction calculation for the Ca_5Si_3 phase reaction. Enthalpy ΔH, Entropy ΔS, Gibbs free energy ΔG and estimated pressure of reaction at T around 700 °C.

$2CaH_2 + 3CaSi \rightleftarrows Ca_5Si_3 + 2H_2$				
***T* (°C)**	ΔH (kJ·mol^{-1}·H_2)	ΔS (J·mol^{-1}·K^{-1}·H_2)	ΔG (kJ·mol^{-1}·H_2)	Estimated equilibrium H_2 Pressure (bar)
695	100.6	103.0	0.8	0.90
696	100.6	103.0	0.7	0.91
697	100.6	103.0	0.6	0.92
698	100.6	103.0	0.5	0.94
699	100.6	103.0	0.4	0.95
700	100.6	103.0	0.3	0.96
701	100.6	103.0	0.2	0.97
702	100.6	103.0	0.1	0.98
703	100.6	103.0	0.0	1.00
704	100.6	103.0	-0.1	1.01

4.2.2.3. Comparison of 5 different stoichiometries of xCaH_2 + ySi

A systematic experiment was conducted on the following 5 stoichiometries according to the predictions: ratio CaH_2/Si = 1:2, 3:4, 1:1, 5:3, 2:1. It was expected that, CaH_2 being the limiting reagent, a different final compound would be obtained for each ratio. Each TPD measurement was done using the same parameters: 5 °C/min up to 700 °C. For each measurement it has been assured that the pressure did not limit the reaction. The pressure in the system was limited during the temperature plateau at 700 °C (2 hours) by evacuating the reference volume while the valve to the sample volume was closed. The sample valve was then reopened to reduce the total pressure in system.

As depicted in the summary Table 4-3 and Experimental section , an amount of oxide ≈ 4 to 12 wt % was observed. This explains the loss of efficiency compared to the theoretical value. Indeed, a part of the CaH_2 initial powder was oxidised and this limits the reaction with the silicon-based compounds except for the $2CaH_2$ + Si composition, where excess CaH_2 that didn't react was observed. The following was observed for each ratio:

- Ratio 1:2

Not all the silicon is consumed (13 wt % left). This is explained by the lack of CaH_2 due to the presence of CaO in the initial mixture. As expected, the $CaSi_2$ (*R*-3*m* space group) is formed (74 wt %), as well as a small amount (5 wt %) of CaSi (*Cmcm* space group).

- Ratio 3:4

No trace of a Ca_3Si_4 structure, but instead a mixture of CaSi and $CaSi_2$, respectively 45 and 49 wt %. It suggests that the Ca_3Si_4 phase might be not stable at room temperature as described in section 4-1.

- Ratio 1:1

Predominantly a CaSi (89 wt %) structure is formed and a small amount of $CaSi_2$ is leftover (7 wt %).

- Ratio 5:3

Mainly CaSi (54 wt %) is formed and also a Ca_5Si_3 (*I*4*/mcm* space group) structure is formed (25 wt %). Due to a large presence of CaO (12 wt %) the reaction is not complete.

- Ratio 2:1

Extra CaH_2 forms Ca_5Si_3 representing 79 wt % of the final composition. CaH_2 and CaSi phase are leftover: 6 wt % for both, probably due to the slow kinetics at 700 °C. A plateau duration of 2 hours may not be adequate. Ca_2Si is not detected. The theoretical temperature of formation is > 700 °C under primary vacuum condition (> 1 x 10^{-3} bar). See Figure 4-8.

Figure 4-7: Comparison of X-ray analysis between a ball milled mixture ($5CaH_2$+3Si) and 5 different stoichiometries (ratio Ca:Si : 2:1 (red), 3:4 (blue), 1:1 (green), 5:3 (purple), 2:1 (pink).

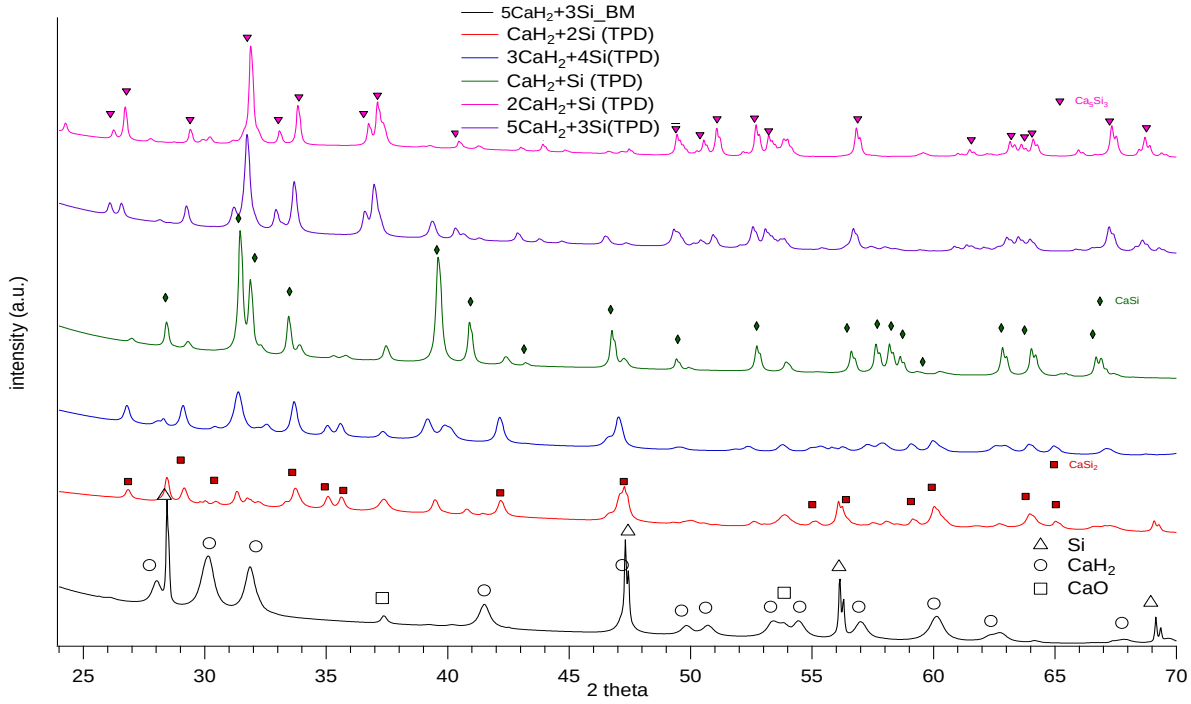

Table 4-3: Summary table of the TPD experiments for the $xCaH_2$ + ySi system. Efficiency is Experimental weight percent of hydrogen released divided by theoretical value. Weight percent of each phase quantified by X-ray analysis using Topas©(±1 wt %).

	ratio	Theo H_2 wt %	Exp H_2 wt%	Efficiency %	Si wt %	CaH_2 wt %	CaO wt %	CaSi wt %	$CaSi_2$ wt %	Ca_5Si_3 wt %
CaH_2 + 2Si	1:2	2.05	1.89	92%	13	0	8	5	74	0
$3CaH_2$ + 4Si	1:1.3	2.53	2.41	95%	1	0	5	45	49	0
CaH_2 + Si	1:1	2.87	2.73	95%	0	0	4	89	7	0
$5CaH_2$ + 3Si	1:0.6	3.42	2.98	87%	0	0	12	54	9	25
$2CaH_2$ + Si	1:0.5	3.59	3.00	83%	0	6	10	6	0	79

Figure 4-8: Calculated equilibrium condition of pressure and temperature for the $xCaH_2 + ySi$ system.

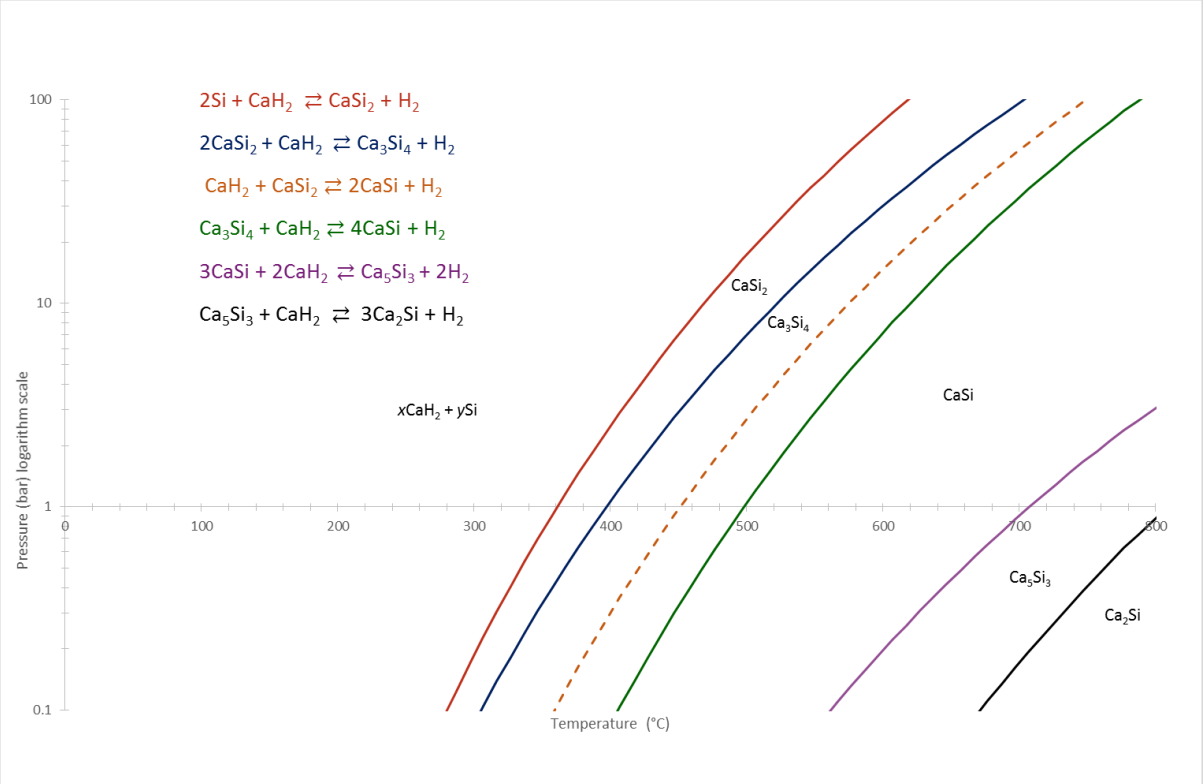

4.2.2.4. Summary of TPD measurements

It has been observed that an oxidation during handling of the samples is results in consumption of CaH_2 and makes calcium hydride a limiting reactant. To avoid this issue, it is imperative to load the sample in a clean and outgassed reactor and to seal this in a neutral atmosphere i.e. in a glovebox.

It has been observed also that at 700 °C the threshold of the equilibrium pressure has been reached below a pressure of 1 bar as calculated and showed on Figure 4-8.

According to these results, it can be understood that different structures are formed during the temperature ramp and that the desorption reaction is a multi-step reaction. The *ex-situ* X-ray analysis shows that all the expected phases determined by theoretical calculations do not appear; Ca_3Si_4 is missing but a mixture of $CaSi_2$ and CaSi appear. A direct reaction $CaH_2 + CaSi_2 \rightleftarrows CaSi + H_2$ (orange

dotted line on Figure 4-8) without intermediate formation of Ca_3Si_4 cannot be excluded. To summarise the different reaction according to the stoichiometry after a TPD measurement up to 700 °C:

- $CaH_2 + 2Si \rightarrow CaSi_2 + H_2$
- $3CaH_2 + 4Si \rightarrow CaSi_2 + 2CaSi + 3H_2$
- $CaH_2 + Si \rightarrow CaSi + H_2$
- $5CaH_2 + 3Si \rightarrow Ca_5Si_3 + 5H_2$
- $6CaH_2 + 3Si \rightarrow Ca_5Si_3 + 5H_2 + CaH_2$

In the following sections, thermal analysis (TGA, STA, DSC and MS) and *in-situ* synchrotron analysis help to visualise the path of reaction and the enthalpy of reaction evolution during the temperature ramp.

4.2.3. Thermal analysis

As explained above, the samples are air sensitive. Thermal characterisations were done at the Institute of Materials Research at Helmholtz-Zentrum Geesthacht (HZG) in Germany (The temperature ramps are pre-set in the machines). For complementary experiments, samples were sent to the University of New South Wales (UNSW) for simultaneous thermal analysis. DSC-TGA and Mass Spectrometry were run at the same time. Equipment for analysis in these laboratories are in gloveboxes (see Chapter 2-4).

4.2.3.1. Differential Scanning Calorimetry

At HZG laboratory, the DSC measurements had to be done in a controlled atmosphere glovebox under 1 bar of hydrogen back pressure with a temperature ramp rate of 5 °C/min up to 500 °C. The temperature limitation of the machine makes this result incomplete (Figure 4-9). Despite the lack of information at high temperature, some observations are interesting to analyse:

- At T ≈ 350 – 370 °C, all the curves start to inflect, therefore an endothermic reaction commences at this temperature
- An endothermic reaction accompanied with an important heat flow begins at T ≈ 450 °C
- For all the different stoichiometry, except the less CaH_2-rich, the reaction may continue at a temperature > 500 °C.

- For the 1:2 stoichiometry, an inflection is observed at T ≈ 480 °C.

Figure 4-9: Comparison of DSC measurement up to 500 °C at 5 °C/min under 1 bar of hydrogen back pressure on 4 different stoichiometric samples.

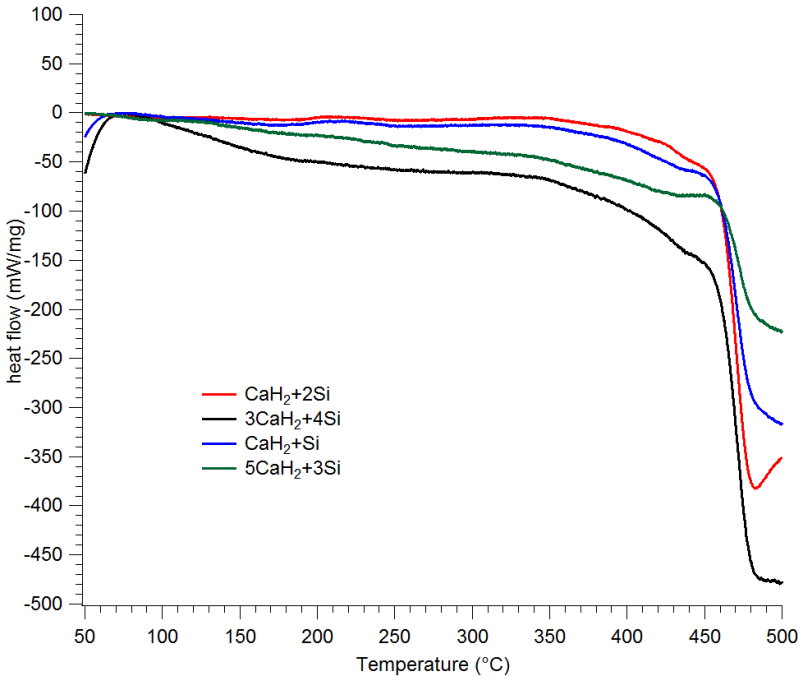

4.2.3.2. Simultaneous Thermal Analysis (STA)

DTA-TGA analysis (3 °C/min under Argon flow) on the same stoichiometric samples as above has been conducted. The machine equipped by a TGA analyser, a differential thermal analyser and mass spectrometer, is able to conduct experiments up to 750 °C. This type of measurement helped to understand the reaction occurring at higher temperature comparing with TPD data. For example, in (a), the differential thermal analysis (DTA, red line) and the thermogravimetric analysis (TGA, green line) are plotted, and compared with the TPD measurement (drawn-through black line). The derivative of the TPD measurement (dotted black line) highlights the hydrogen desorption inflection.

Figure 4-10 Comparison of thermal analysis (DTA and TGA) with hydrogen desorption and its derivative measurement (dotted black line) for a) CaH_2 + Si system and b) $5CaH_2$ + 3Si system.

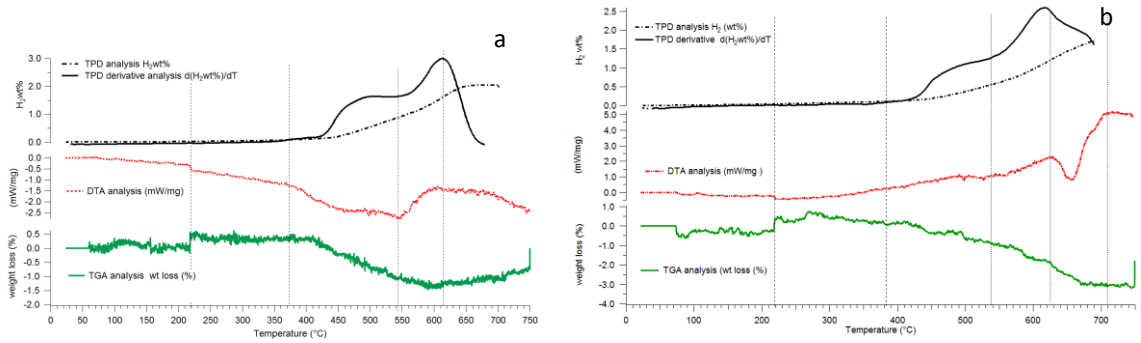

The results of this set of measurements are affected by two minor factors. Firstly, the system of analysis is highly sensitive to external disturbance. Because this equipment is sensitive, every movement around the glovebox could cause a measured artefact on the TGA curves. Secondly, calcium hydride is highly reactive to oxygen. Any trace of O_2 in the glovebox atmosphere can cause parasitic reaction. For example, in (a), on the TGA curve at high temperature (> 600 °C) a mass gain can be seen. This could be explained by the sample oxidation at this temperature. Several corrections have been done to correct artefacts of measurement without corrupted the measure in agreement with Dr Anna Lisa Chaudhary from HZG laboratory.

Despite the noisy signal for DTA and TGA, it is noted that a certain consistency exists for the samples. Only 2 of them are plotted here for a better visualisation, but a systematic study of all the previous stoichiometry has been done. Different events such as oxidation, hydrogen desorption, phase changing, etcetera can be observed. These observations are:

- At $T \approx 218$ °C, according to DTA and TGA analysis, a quick endothermic reaction with a mass loss probably due to oxide pollution occurred. This point is backed up by the *in-situ* X-ray analysis (section 4.2.4)

Especially, this set of measurement shows a multi-step endothermic reaction with specific points as follows:

- At $T \approx 370$ °C, first inflection point of decomposition
- At $T \approx 540$ °C, second inflection point of decomposition
- At $T \approx 610$ °C, end of the second decomposition
- At $T \approx 625$ °C inflection point of a reaction only for the samples with ratio CaH_2/Si > 1:1 (figure 4-10-b)

These results are comparable with the TPD measurement obtained in our laboratory. A small offset in the inflection point's temperature might be due to a different ramp rate between the two experiments (3 °C/min for STA versus 5 °C/min for TPD measurement).

Figure 4-11 shows a second set of measurements repeated to avoid oxidation issues as much as possible. The CaH_2 poorer and richer stoichiometry are plotted.

Figure 4-11: Comparison MS (Drawn through lines) and DTA (dotted lines) of CaH_2 + 2Si (green) and $2CaH_2$ + Si (red) composition. Under Ar atmosphere at 10°C/min up to 900 °C.

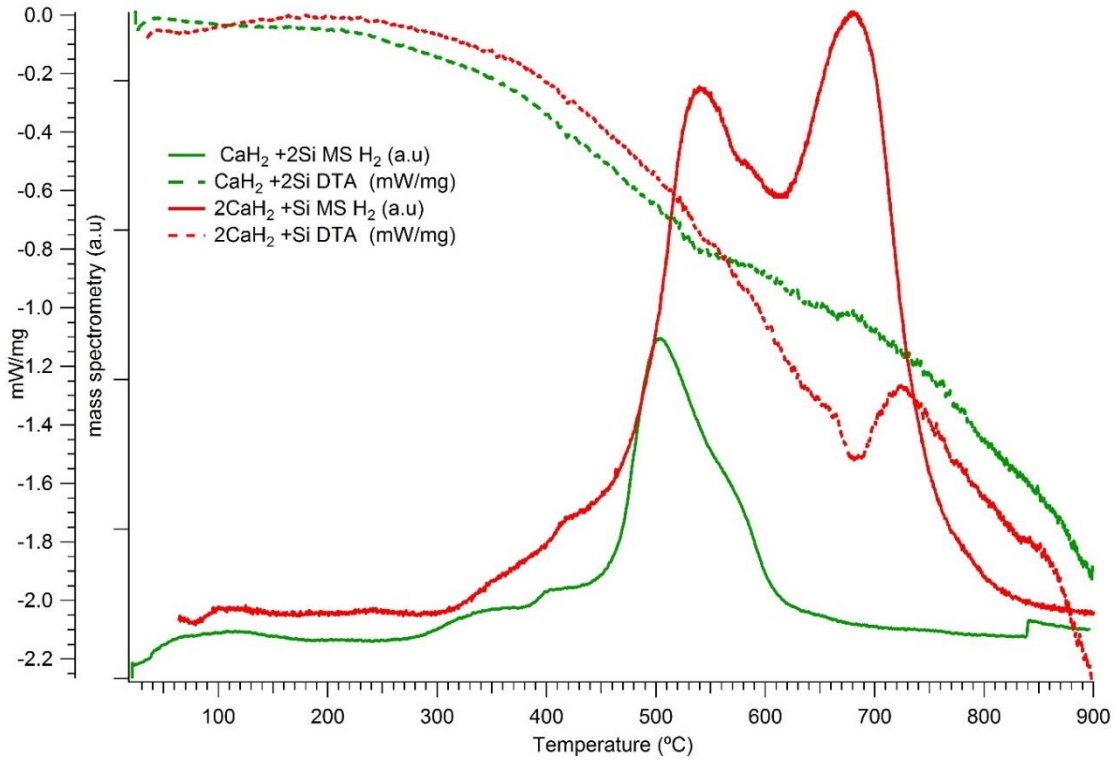

On Figure 4-11, focusing on the MS data (drawn- through lines), it can be observed that:

- For both extreme CaH_2/Si ratio: 1:2 and 2:1, two first weak hydrogen desorption steps happen below 450 °C.
- A main peak of desorption reaching a maximum at 500 °C for 1:2 ratio while for 2:1 ratio desorption continues and reach a maximum at 540 °C and descending to a minimum at 625 °C. This peak may need to be divided into 2 peaks since a bump at 570 °C is evident in both curves.
- For the 2:1 stoichiometry another desorption peak commences at 625 °C, having a maximum at 680 °C.

Powder X-ray analysis on the $2CaH_2$ + Si stoichiometry after this measurement (not shown here) exposed that Ca_5Si_3 has been produced. A high enthalpy reaction occurs for CaH_2-rich sample beginning at ≈ 625 °C with a maximum at 680 °C, showing a peak narrow and deep. This peak is representative of a reaction with a high enthalpy of reaction. All information supports the hypothesis that this reaction matches reaction 16 from Table 4-1:

$$2CaH_2 + 3CaSi \rightleftarrows Ca_5Si_3 + 2H_2 \qquad \text{reaction 4-3}$$

STA obtained from UNSW confirms these phenomena thanks to a DSC measurement (Figure 4-12) based on the multiple steps of reaction observed.[***] Potentially due to a different temperature ramp rate, an offset in the temperature, compared to the previous data, is noticed (10 °C/min). Under 600 °C, 1.8 wt % of hydrogen is desorbed in multiple steps of desorption. This hydrogen desorption matches the H_2 wt % for the formation of CaSi compounds in Figure 4-2. For the sample containing $2CaH_2$ + Si, the results showed a multiple step because of the shape of both DSC (black line) and MS (red dotted line) curves. An overlapping of several peaks of hydrogen releasing could be identified especially on the MS curve (red line). The hydrogen releasing may be due to different reactions. The first peak that can be considered as 2 peaks overlapping are matching with all the observations made for the formation of CaSi, and the last peak is matching with the suggested reaction 4-3. The maximum of these peaks is aligned with inflection point of the DSC curve (black line) and potentially of the TGA curve (green line). At $T > 600$ °C, an endothermic reaction of desorption (1.2 H_2 wt %) with an optimum of ≈ 700 °C is witnessed.

[***] Using a DSC measurement, a more precise idea of the heat flow is obtained i.e. the endo or exothermic characteristics of the involved reactions can be determined.

Figure 4-12: Simultaneous Thermal analysis on $2CaH_2$ + Si in a capillary sealed under vacuum at 10 °C/min up to 900 °C.

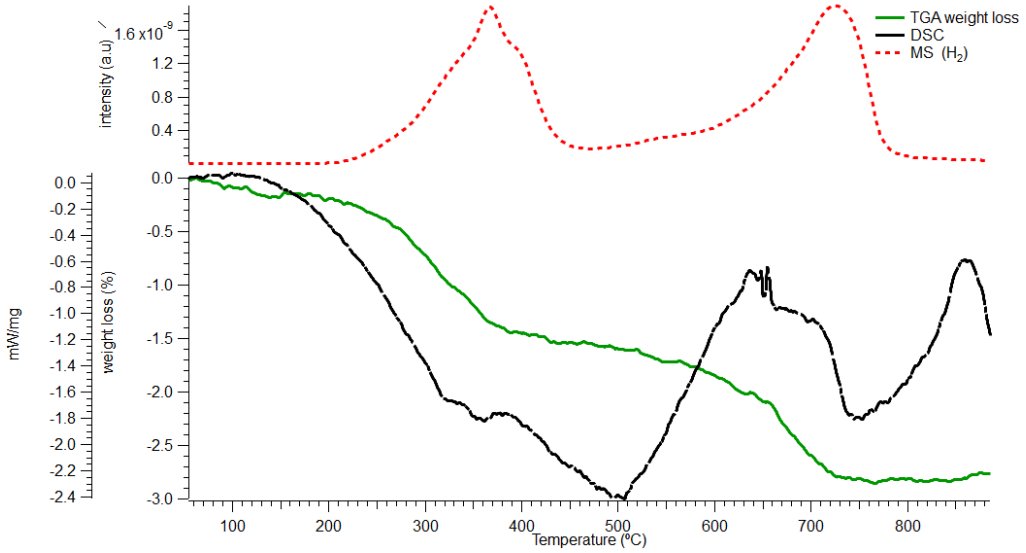

4.2.3.3. Summary of thermal analysis

These results corroborate the observations made in the literature. Wu *et al.* [73] observed that annealing Ca_5Si_3 under 1 bar at 600 °C results in the formation of CaH_2, CaSi and an amorphous phase. Armbruster *et al.*[72] describe the desorption process of a $CaSiH_x$ as a 2 step reaction at least: a first desorption ending before 500 °C followed by a second step finishing at 560 °C. In the case of an initial CaH_2 rich mixture, the desorption behaviour is a multi-step process ending at 700 °C. A first step of reaction before 600 °C in a multistep reaction resulting in the formation of CaSi and 1.8 wt % of hydrogen released. Then, a second step of reaction over 600 °C resulting in the formation of a Ca_5Si_3 structure and 1.2 wt % released. The initial composition of $2CaH_2$ + Si theoretical wt % of hydrogen is 3.6 wt %, and up to 3 wt % of hydrogen is released experimentally. As described in Figure 4-2, up to 3 wt % is necessary to form Ca_5Si_3 and the last theoretical reaction from the Figure 4-2 resulting in the formation of Ca_2Si doesn't occur. It has been observed also that when the formation of Ca_5Si_3 is not finished, traces of CaSi and CaH_2 are left over and no trace of pure Si is found. This infers that the formation of CaSi is a compulsory step of transition with hydrogen desorption before the total hydrogen desorption and formation of Ca_5Si_3. In Figure 4-12 between 450 °C and 600 °C, an endothermic step depicting a phase transition with little or no H_2 released can be distinguished. Using *in situ* synchrotron powder diffraction, the phase transitions with or without hydrogen desorption can be observed.

4.2.4. In situ synchrotron powder X-ray diffraction (SR-XRD)

Powdered samples were loaded in a quartz capillary (outer diameter 0.7 mm, wall thickness 0.01 mm) and mounted on a sample holder with Swagelok fittings in a glove box filled with purified argon (< 1 ppm O_2 and H_2O). The sample holder was then connected to a H_2 gas filling vacuum manifold and the capillary heated with a hot air blower with a heating rate of 5, 8 or 10 °C/min from room temperature (RT) up to 1000 °C under a H_2 atmosphere or vacuum. This measurement used the high-resolution Mythen detector to follow decomposition pathways and, if required, provided data with high statistics that allow the accurate detection of the structures of the decomposition products.

4.2.4.1. In situ synchrotron powder diffraction of CaH_2 samples

Figure 4-13: In situ synchrotron X-ray diffraction data (λ = 0.59027 Å). of pure CaH_2 (synthesised from high purity calcium metal) under 1 bar of hydrogen back pressure at a temperature ramp rate of 10 °C/min up to 938 °C followed by a 30 min isothermal stage and then cooled down (right scale). Left scale is the scan number where right scale shows the temperature evolution.

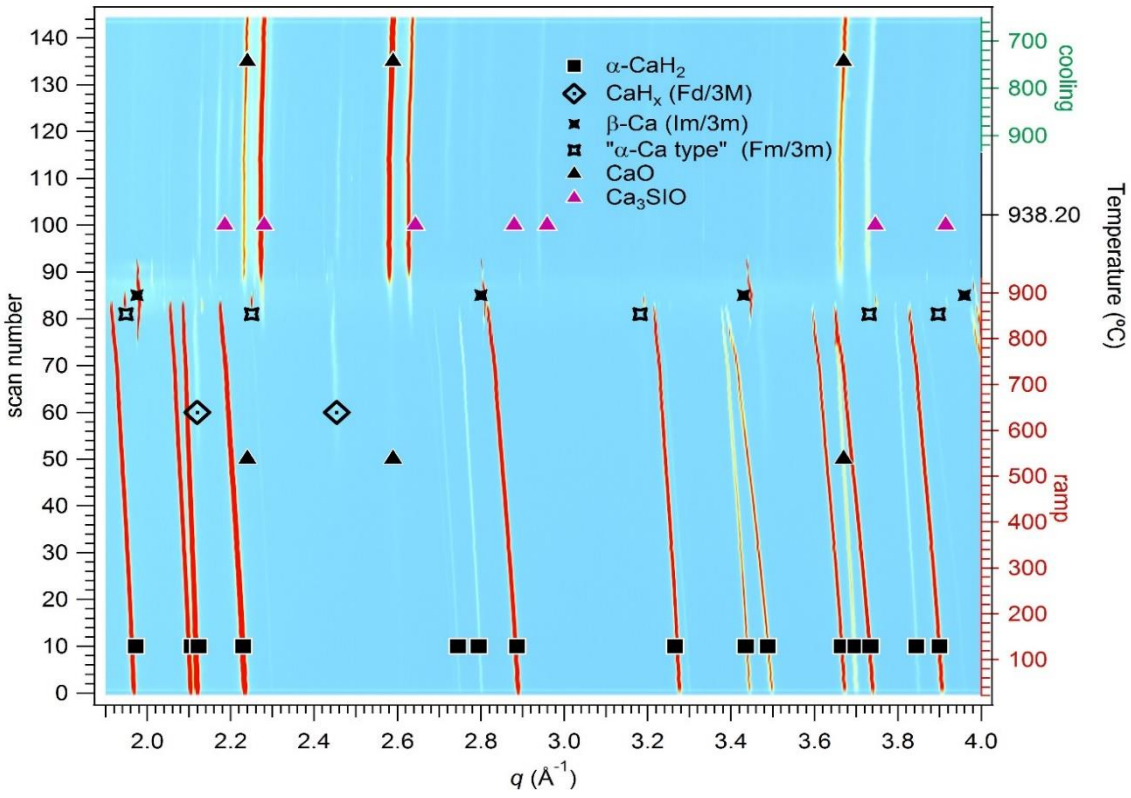

In order to establish a reference, pure CaH_2 was first analysed by *in-situ* X-ray diffraction to help understand the effect of Si-destabilisation on CaH_2 (Figure 4-13). This sample was obtained by

hydrogenating ultra-pure Ca (99% purity) stored in a sealed bulb using the method described by Bulanov *et al.*[74]

According to Johnson *et al.*[75], calcium hydride dissociates in two steps to form a solid solution of a first hydrogen rich phase to then a second H_2 poor CaH_2 phase. On the other hand, Peterson, Fattore *et al*.[29] report a phase change from a α-CaH_2 phase to a β-CaH_2 (β-BaH_2 space group[31])phase formed at 780 °C on the phase diagram (Figure 4-14). The second solid solution phase observed by Johnson *et al*. is due to the presence of Mg-impurities according to Peterson, Fattore *et al*.[29]

Figure 4-14: Phase diagram of Ca-CaH_2 system.[30]

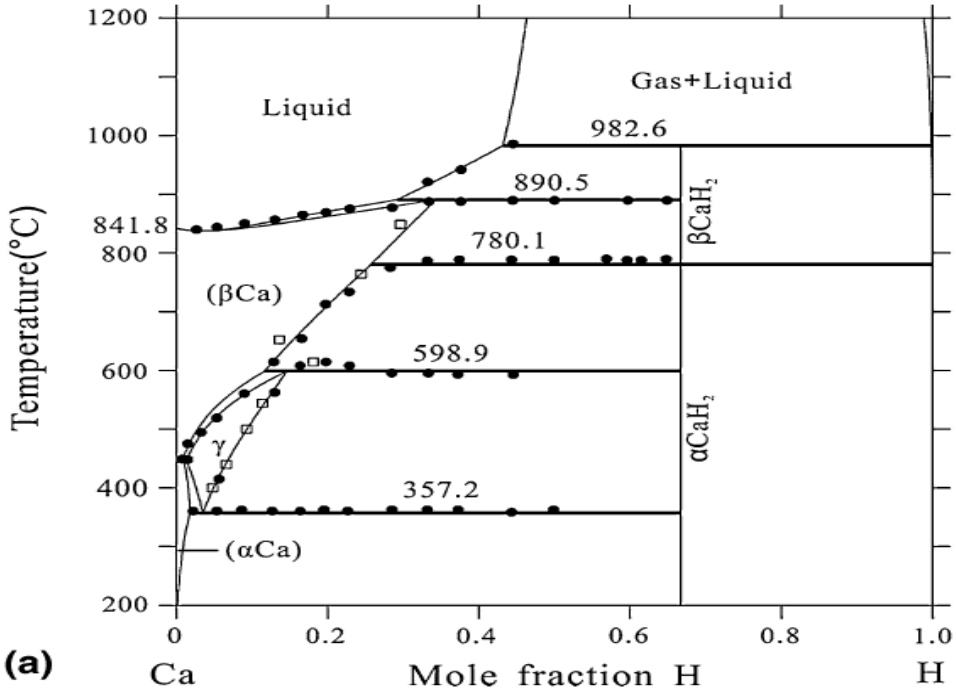

Figure 4-15: Phase identification of in situ synchrotron X-ray analysis for pure CaH_2 at 430 °C before any phase transformation; initial composition.

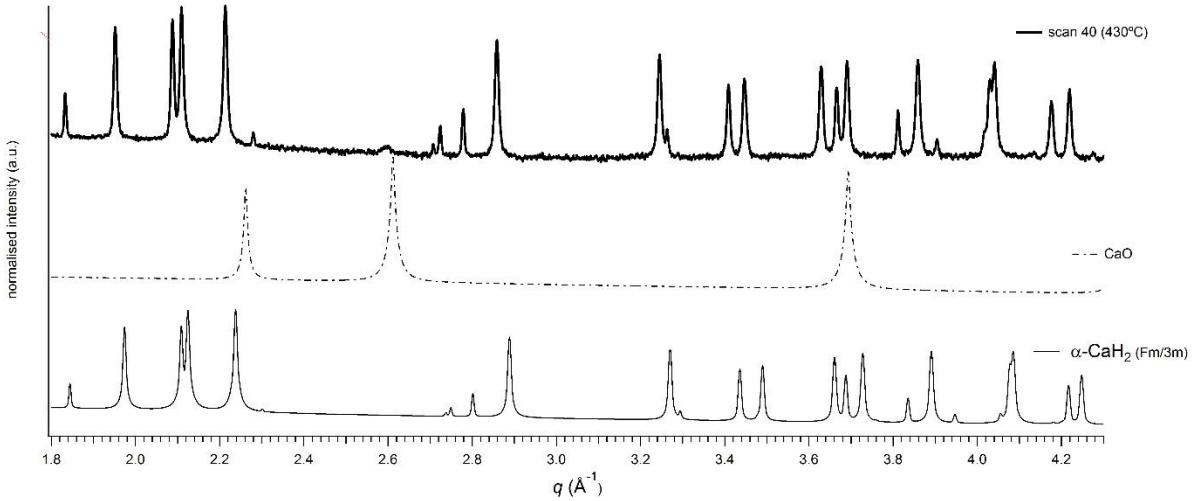

In our case, at room temperature, as expected, the pure (α-CaH_2 *PNMA* space group) peaks match all the peaks (plain black square on Figure 4-13). The weak intensity of CaO (black triangle on Figure 4-13) confirms the high purity of the sample (Figure 4-15): < 2 % of CaO[†††].

A phase transformation occurs starting at ≈ 600 °C and reaching a maximum intensity at ≈ 780 °C. The α-CaH_2 (*PNMA* space group) is partially consumed and no trace of pure α, β or γ pure metal Ca phase is noticeable. By phase identification, using Rietveld refinement software (Topas®), this phase (CaH_x, empty diamond on Figure 4-13) can be identified as a pseudo cubic body centred phase ($Fd\bar{3}M$ space group). A match analysis did not confirm that the observed structure is the β-CaH_2 describe by Curtis *et al.*[31] On the other hand, the broad shape and asymmetry of its peak's patterns (Figure 4-16, in red circle) can be described as a solid solution behaviour as mentioned initially by Johnson *et al.*[75] The shape of the peak confirmed the "pseudo" properties of this phase. Indeed, it can represent not only one peak phase, but a series of peaks with a similar structure and closed matrix parameter. During the temperature and the phase transformation process, this peak may be identified as a series of different stoichiometry of CaH_x composition.

[†††]The choice of plotting the scan at 430 °C has been done in order to obtain a good crystallisation of the CaO peaks and to choose a scan before any phase transformation occurs. It's important to understand that due to the thermal expansion of the calcium hydrides and oxides, there is an offset between the initial position of α-CaH_2 and CaO peaks and the observed peaks with the observed peaks at high temperature.

This possible solution will be called CaH_x phase in the following sections. Between ≈ 790 °C and 880 °C, a mixture with pure Ca metal phase as β-Ca ($Im\bar{3}m$ space group) and α-Ca ($Fm\bar{3}m$ space group) is observed. All the mixtures of α-CaH_2 and CaH_x phases are completely consumed at 880 °C to obtain only the β-Ca phase.

Figure 4-16: Phase identification of in situ synchrotron X-ray analysis of pure CaH_2 at 780 °C; observation of the CaH_x solid solution phase formed.

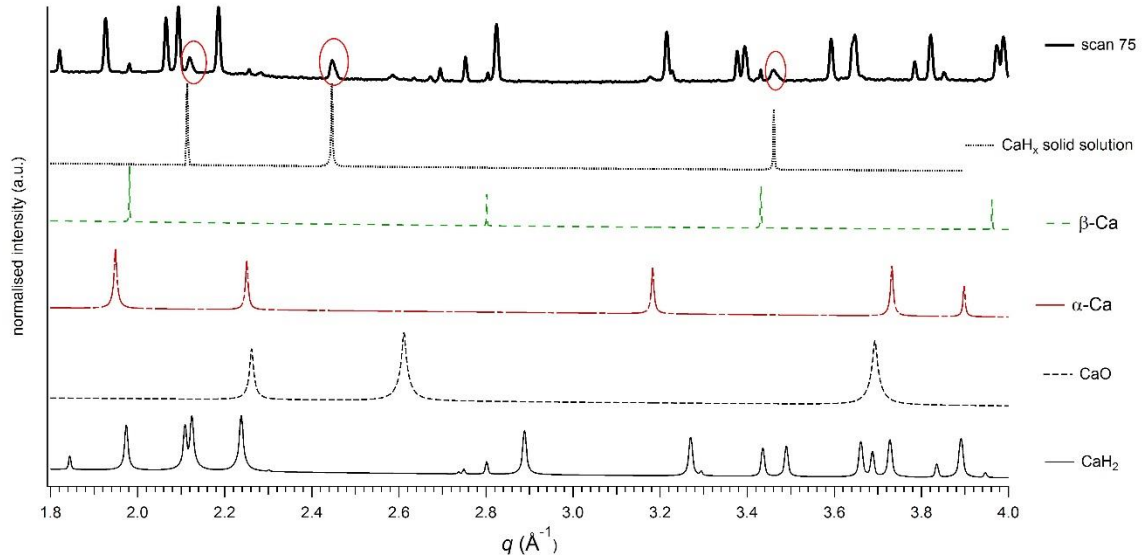

On the in-situ X-ray analysis (Figure 4-13), the appearance of CaO and a Ca_3SiO[‡‡‡] has been noted. It can be seen at 885 °C (Figure 4-13) that this phenomenon starts with the formation of pure β-Ca. It is assumed that Ca-metal or liquid is corrosive at high temperatures > 800 °C. These phenomena have been experimented on previous set of data in our laboratory. Indeed, melted calcium has been observed in a reactor heated up to 800°C. The formation of a calcium silicon oxide has been observed by *ex-situ* X-ray analysis after sorption measurement in a reactor, which was not been sealed or leaked at high temperature.

[‡‡‡] During the measurement, it has been observed that at high temperature, the sample seems to react with the capillaries, that crack before breaking during the cooling ramp at 660 °C. That's why our observations stopped at this temperature.

Figure 4-17: Phase identification on in situ synchrotron X-ray analysis of pure CaH_2 at 885 °C; maximum of desorption, formation of β-Ca and beginning of capillary cracking.

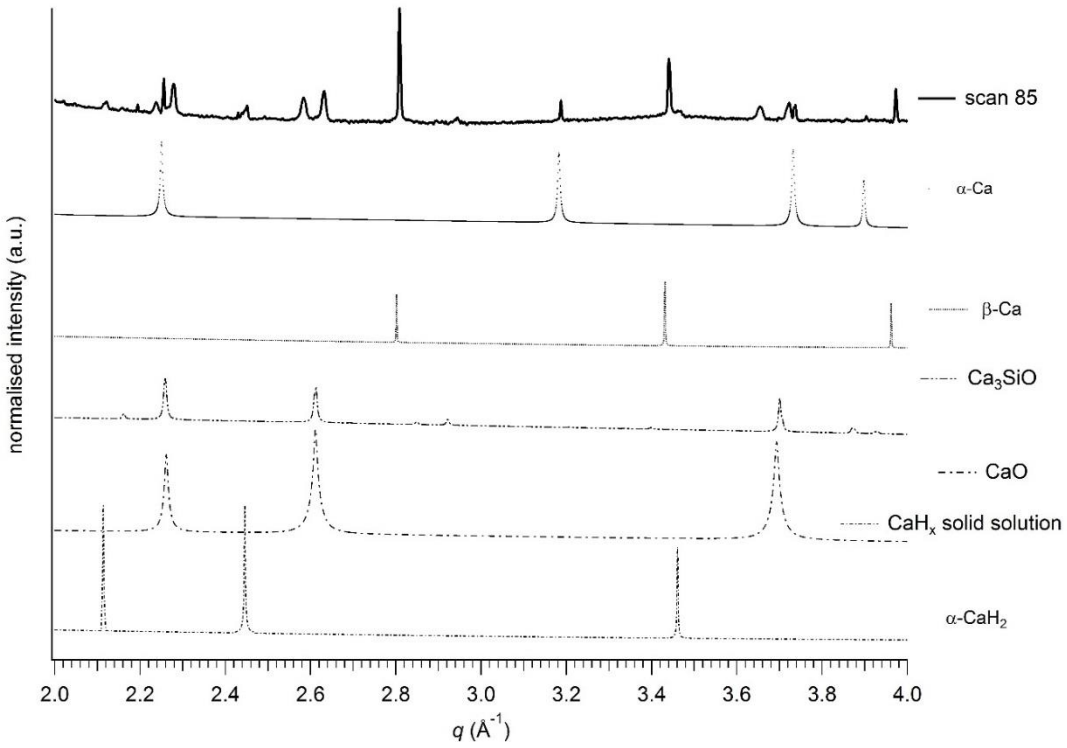

The oxidation reactions due to oxide pollution can be identified by comparing the results of i*n-situ* synchrotron X-ray diffraction with the CaH_2 powder provided by Sigma Aldrich® (95 % pure CaH_2) (Figure 4-18). Because of the 5 % of oxide contamination in the Sigma Aldrich® samples, specific reactions due to CaO or $Ca(OH)_2$ are observable. Quantitative XRD analysis of the as received material at room temperature indicates ~1.5 wt % of calcium hydroxide ($Ca(OH)_2$) (empty black triangle) and 2.5 wt % of α-CaO (plain black triangle). Below 300 °C, $Ca(OH)_2$ decompose and forms CaO, releasing a low quantity of water.[76] Then calcium oxide reacts to form an "α-Ca type" structure (*Fm*$\bar{3}$*m* space group) (empty cross) at 760 °C. This structure contracts i.e. the lattice parameter diminishes whereas the thermal expansion involves a lattice expansion. Finally, this "α-Ca type" structure transforms into α-CaO and Ca_3SiO, probably at the instant when the capillary starts to crack. The observation of a "α-Ca type" structure is in contradiction with the phase diagram (Figure 4-14), since at 450 °C the α-Ca

should have already transformed into β-Ca[§§§]. From here after this phase will be called the "α-Ca type" phase. The phases α-Ca and α-CaO are cubic structures. The lattice parameter of the "α-Ca type " phase is reduced from *q* = 5.58 Å to 4.98 Å. (The final lattice size of CaO is 4.78 Å). The "α-Ca type" phase is an intermediate phase between the α-Ca and α-CaO structures.

Finally, the CaH_x solid solution is formed at the same temperature (≈ 580 °C) as in the previous experiment. Contrariwise, it has been observed that the initial α-CaH_2 phase is totally transformed at ≈ 780 °C while for the pure caH_2 sample, the α-CaH_2 phase is totally transformed at ≈ 880 °C. This suggests that the presence of the oxide destabilises CaH_2. With an initial proportion of 4 wt % of CaO (estimated by Rietveld refinement on scan 30, at ≈ 300 °C), the hydrogen desorption temperature is lowered by ≈ 100 °C[****].

[§§§] The hypothesis that the beam size is larger than the heated area and that a part of the measured sample is at lower temperature (< 450 °C) than the displayed one, cannot be excluded.

[****] The temperature calibration was conducted before and after the whole in-situ session and it shows an error of ≈ 50 °C. Due to this important uncertainty, the last point cannot be fully assumed.

Figure 4-18: In situ synchrotron X-ray analysis (λ = 0.59027 Å) of CaH_2 (Sigma Aldrich (95 % purity) under vacuum. Left scale is the scan number, and the right scale shows the evolution in temperature. The different peaks are converted in q ($Å^{-1}$) on the x axis. Temperature is increased up to 870 °C at 10 °C/min

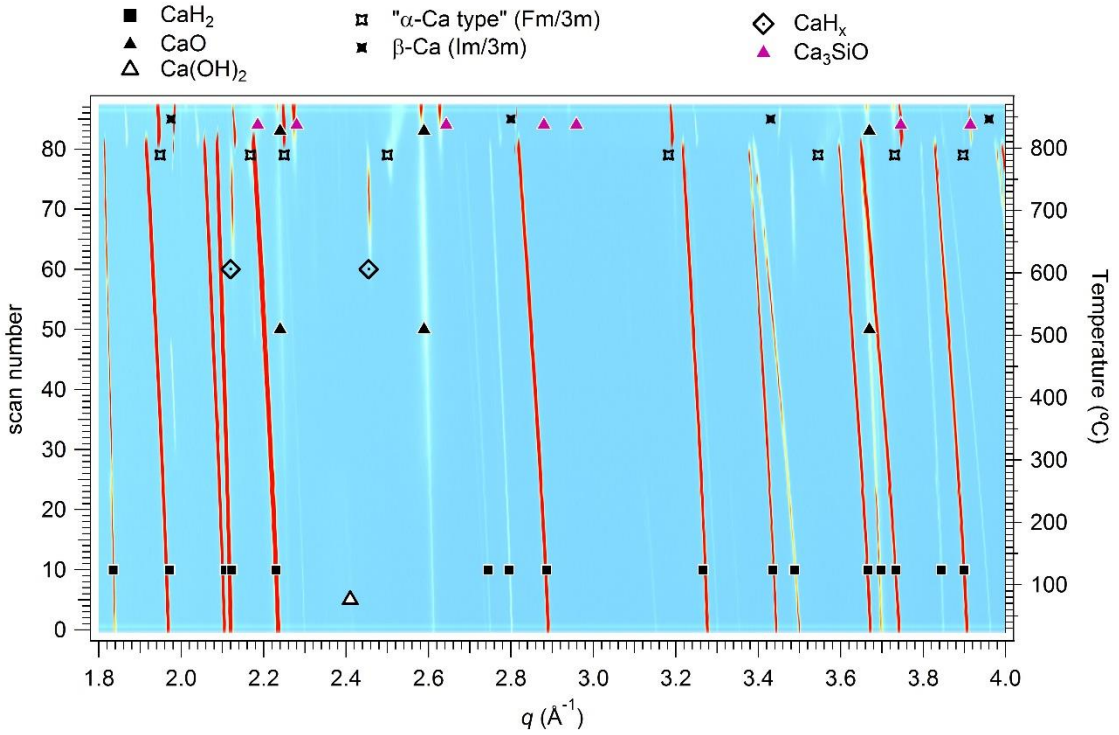

These experiments are interesting to compare as they allow one to observe the reactions of CaH_2 and the oxidation reaction, and help understand the unmatched peaks that do not correspond to a Ca_xM_y structure, where *M* is a metallic element or compound such as Si, C or MgO.

To summarize:

- α-CaH_2 transforms partially to a CaH_x solid solution.
- Starting around 780 °C the β-Ca phase is formed.
- The presence of an oxide causes a parasite phase at $T \approx 760$ °C to form a "α-Ca type structure".
- Then the lattice parameters of the "α-Ca type" structure reduces before transforming back into the CaO phase.
- All the hydride is consumed between 780° C to 880 °C. The difference might depend on the presence of oxide and/or the temperature calibration error.
- The CaO seems to be destabilising the CaH_2.

4.2.4.2. *In situ synchrotron powder diffraction of CaH_2 + 2Si*

Figure 4-19: In situ synchrotron powder diffraction of CaH_2 + 2Si ((λ = 0.77454 Å).

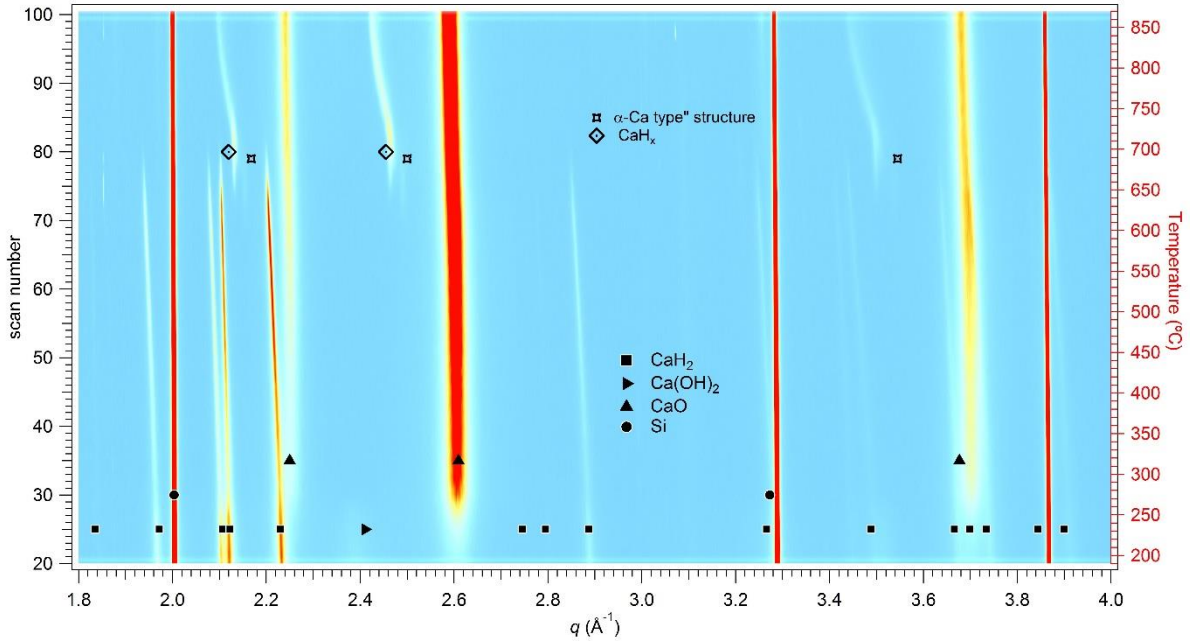

A powdered mixture of calcium hydride (Sigma Aldrich®, CaH_2 95 %) and silicon (Sigma Aldrich®, Si 99%) was packed in to a sealed quartz capillary and scanned by *in-situ* synchrotron X-ray diffraction (wall thickness = 0.01 mm) with a back pressure of 0.5 bar of hydrogen and heated up to 850 °C at 5 °C/min.

In Figure 4-19 markers show the identified phases (CaH_2, Si, CaO, $Ca(OH)_2$) and the estimated phases ("α-Ca type" structure and CaH_x solid solution type) using the Topas© software for the identification of the unknown phases formed at high temperature. Some qualitative information can be obtained from the results of this set of measurements:

- The initial mixture was contaminated by calcium hydroxide: $Ca(OH)_2$. The $Ca(OH)_2$ is consumed while CaO is formed at temperature lower than 300 °C.
- At least 2 phases are formed during the heating ramp: "α-Ca type" and CaH_x solid solution type. The first phase appears at ≈ 600 °C and disappears at ≈ 670 °C, similar to the cubic structure "α-Ca type"; the peaks of this phase are shifting to the right, which is characteristic of a lattice contraction.

- A second phase is formed at 620 °C, possibly being the CaH_x solid solution observed on pure CaH_2 (see section 4.2.4.1). The peaks shift to the left, a typical signal of a lattice expansion. According to the evolution of the lattice expansion during the temperature ramp, it can be assumed that the CaH_x is acting as a solid solution, either with a silicon atom insertion or with a lattice reorganization due to vacancy formation caused by H_2 desorption in a slow kinetic process.[††††] Indeed, the peaks shifting is too important to be only due to the thermal expansion.
- At ≈ 700 °C, all the initial α-CaH_2 has been consumed and the CaH_x solid solution was formed at a temperature < 700 °C.

Solving structures at high temperatures is a complex process. Indeed, the lattices show an important expansion, depending on the temperature. The structure files from PDF 4+, crystallography.net or other sources are generally calculated at room temperature. To remedy this problem, with help from a crystallography expert, Dr Matthew Rowles, a code was programmed, using JEdit© communicating with Topas© software. With the known phase at room temperature, this code made the lattice parameters evolve using the previous scan parameters. In this way, the matrix parameter evolved step by step according to the thermal expansion. Furthermore, by identifying the peaks that appear at high temperature, it could be determined that the CaH_x structure was pseudo cubic body centre ($Fd\bar{3}M$ space group).

By using the SMV (crystal structure Scale, matrix Mass and Volume) method described by Styles *et al.*[77] i.e. estimating a crystal structure mass in order to maintain SMV stable, the composition of these phases can be determined. Figure 4-20 shows the SMV factor including the estimation of the mass of the "α-Ca type" and CaH_x phases. This way, weight percent evolution of each phase has been estimated. Using those values, the evolution of molar fraction of all phases was calculated in order to determine both phase composition stoichiometry. Neither the silicon nor calcium sublime in this temperature range so their proportion is constant during the measurement even when a leak is present. The "α-Ca type" phase formed and disappeared between 580 °C and 670 °C, and was estimated to be < 2.3 wt %. A high quantity of CaH_2 was oxidised (≈ 35 wt % of CaO in the final

[††††] The statistics on the silicon peaks are too poor to determine if the Si is consumed or not during the reaction.

composition) and ≈ 10 % of the CaH_x formed at ≈ 640 °C was produced. During this measurement the capillary was leaking, and this can be seen by the increase of CaO.

At this stage, it cannot be determined if the decomposition of CaH_2 is due to the formation of a Ca_xSi_y phase formation or due to the oxidation.

Figure 4-20: Estimation of SMV of each initial and estimated phase and sum of all SMV values kept stable by defining the mass of the solid solution curve of the estimated structure.

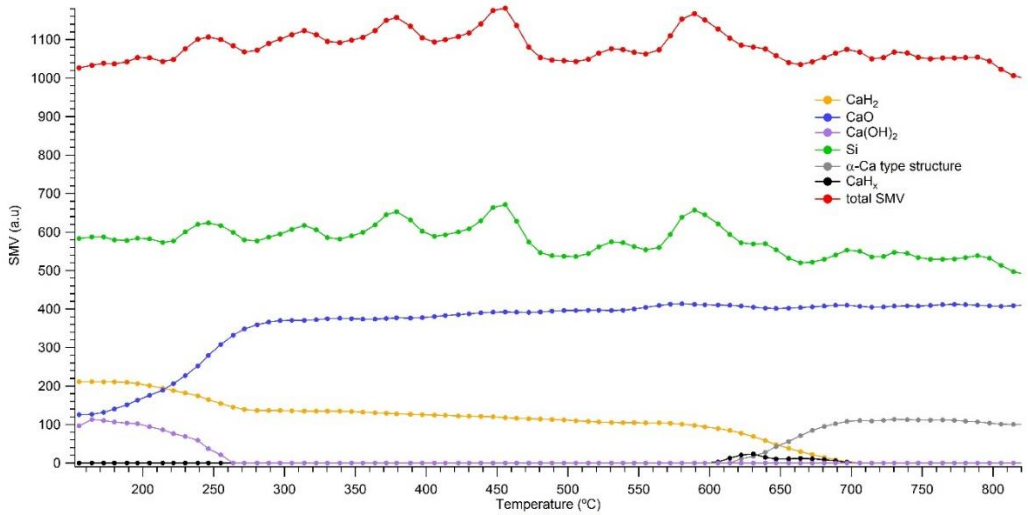

4.2.4.3. *In situ synchrotron powder diffraction of $3CaH_2 + 4Si$*

Figure 4-21: In situ synchrotron powder diffraction of $3CaH_2 + 4Si$ (λ = 0.77454 Å). Q factor vs Temperature and number of scans. Heating ramp up to 786 °C, 20 minutes plateau and cooling ramp down to 350 °C under 0.5 bar of hydrogen back pressure.

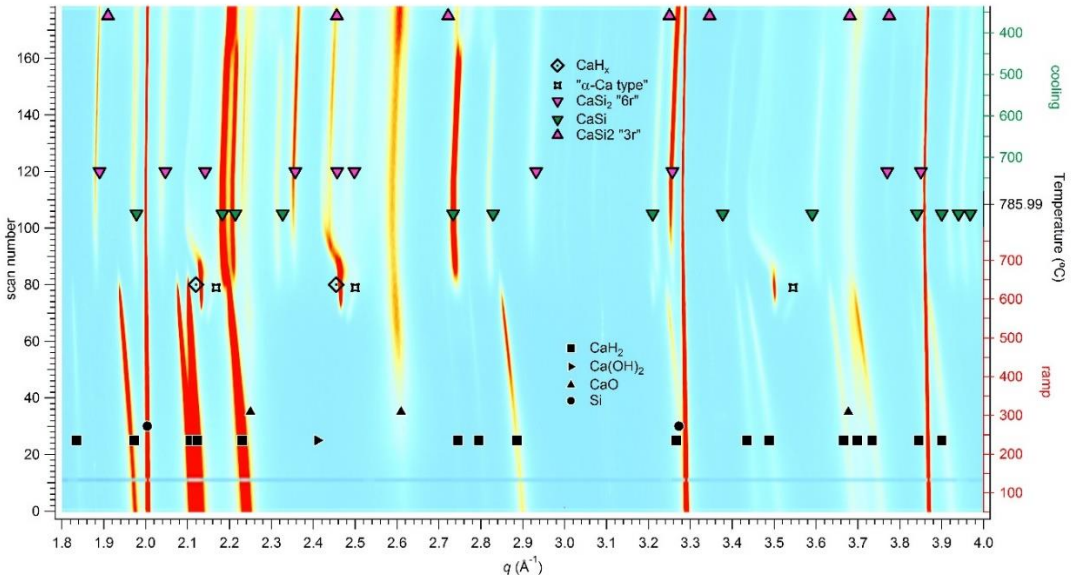

A sample mixture of $3CaH_2$ + 4Si has been analysed by *in-situ* X-ray analysis (Figure 4-21). *In-situ* powder diffraction analysis has been conducted on this system during the heating ramp, a 20 minutes plateau and a cooling ramp down to 350 °C. These results can give more information about the system. First of all, the reaction pathway is consistent with the set of data above:

- Up to 18 wt % of CaO is measured at ≈ 220 °C (scan 22)
- A first phase is formed "α-Ca type" at ≈ 550 °C (scan 67) and is consumed before ≈ 700 °C (scan 87).
- A phase is formed at 580 °C (scan 71) and forms a "CaH_x solid solution" as the temperature increase.
- 2 different phases are formed at respectively T ≈ 650 °C (scan 80) and T ≈ 695 °C (scan 85). Peaks at q = 1.87 $Å^{-1}$, 1.96 $Å^{-1}$, 2.31 $Å^{-1}$, 2.8 $Å^{-1}$, 3.57 $Å^{-1}$, 3.8 $Å^{-1}$, 3.9 $Å^{-1}$, 4 $Å^{-1}$ and at q = 2.36 $Å^{-1}$, 2.9 $Å^{-1}$ etc. In Figure 4-22, those phases are identified as CaSi (*Amma* space group) and the $CaSi_2$ ($R\bar{3}m$ "6r" space group) described by Nedumkandathil *et al.*[78] The $CaSi_2$ "6r" structure (c = 30.17 $Å^{-1}$ = 2 time the c lattice parameter of a 3r c = 15.84 $Å^{-1}$) is stable at high temperature and may revert to "3r" during cooling.
- A reorganisation of the structure is notable during the cooling ramp for these two structures. Analysis of the last scan of this experiment at 350 °C showed a match with CaSi (*Amma* space group) and a $CaSi_2$ ($R\bar{3}m$ space group) "6r" and "3r" mix. It seems that the CaSi structure is decomposing during cooling to 470 °C – 460 °C to form a $CaSi_2$ "3r" ($R\bar{3}m$ space group), and the $CaSi_2$ ($R\bar{3}m$ space group) "6r" is stable. This is in agreement with Nedumkandathil *et al.* who observed that the "6r" structure stabilises over the "3r" structure.
- All the α-CaH_2 is consumed at 650 °C i.e. all the hydrogen is released.

Figure 4-22: Phase ID of scan number 118 at 786 °C at the plateau's end of $3CaH_2 + 4Si$ sample.

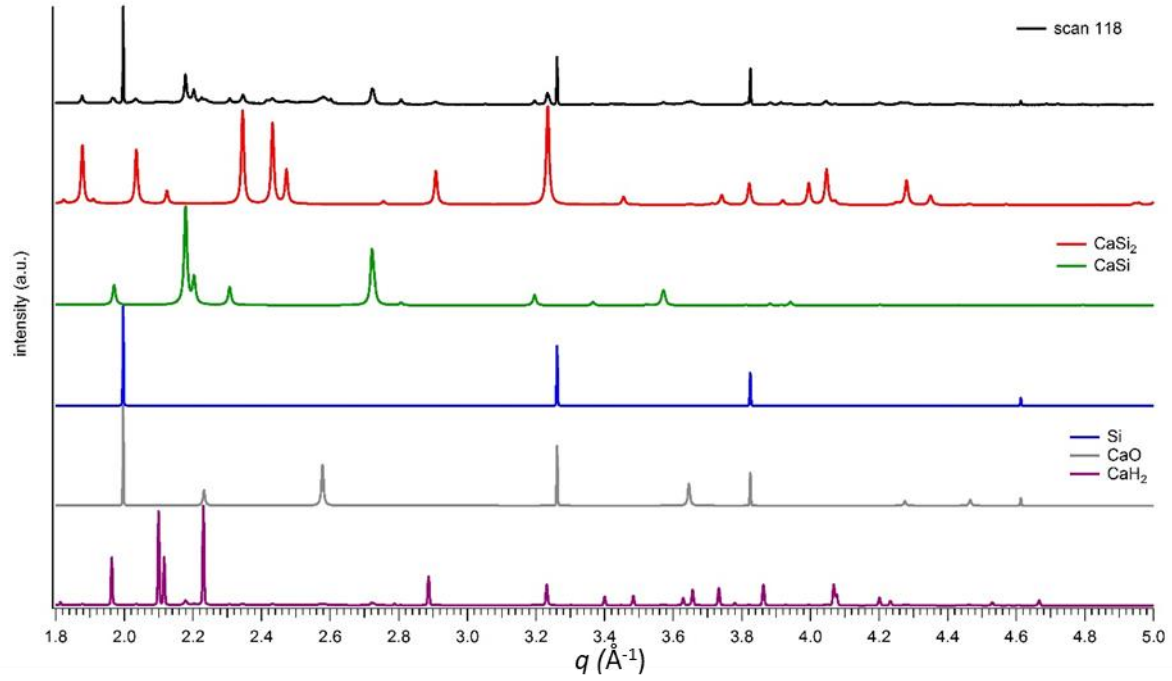

To conclude, the behaviour of the CaH_x confirms the hypothesis that a solid solution has been formed. Indeed, it has been observed that the lattice size of this structure decreases and then forms a mixture of CaSi and $CaSi_2$ structures. Also, the CaH_x and the "α-Ca type" structure contraction can be due to two causes: silicon substitution in a calcium lattice (the silicon atom is smaller than the calcium atom, hence the lattice size diminishes) or hydrogen release, which by definition reduces the lattice size.

Two other sets of measurements with a higher CaH_2/Si ratio were analysed (not shown here), but the data are not usable due to a final concentration of CaO equal or superior to 20 wt % which mean that even with an initial material rich in CaH_2. The number of moles of CaH_2 that may react with Si is equivalent to a ratio under 1.5:1 maximum. The analysis of this result does not provide more information concerning the steps of reaction between CaH_2 and CaSi or $CaSi_2$. This explain why the formation of Ca_5Si_3 was not observable. It should be noted that by comparing these data, it can be seen that the higher the percentage by weight of CaO, the more the reaction temperatures are shifted to a higher temperature. It is hypothesised that the oxide creates a kinetic barrier between the calcium hydride and the silicon. The phenomenon of kinetic barriers has been already described by Meggouh *et al.*[79] for complex metal hydrides.

4.2.4.4. *In situ synchrotron powder diffraction of $2CaH_2 + Si$*

In order to avoid oxidation during the measurement, a new system for a sample container using 0.05 mm wall thickness capillaries was used for the following beam time experiments (see Figure 4-23). A set of measurements under 1.5 bar of hydrogen back pressure was analysed.

Figure 4-23: In situ synchrotron powder diffraction data for $2CaH_2 + Si$ (λ = 0.59027 Å). Q factor vs number of scan and temperature. Heating ramp up to 886 °C (10 °C/min), and cooling ramp down to 338 °C under 1.5 bar H_2 back pressure.

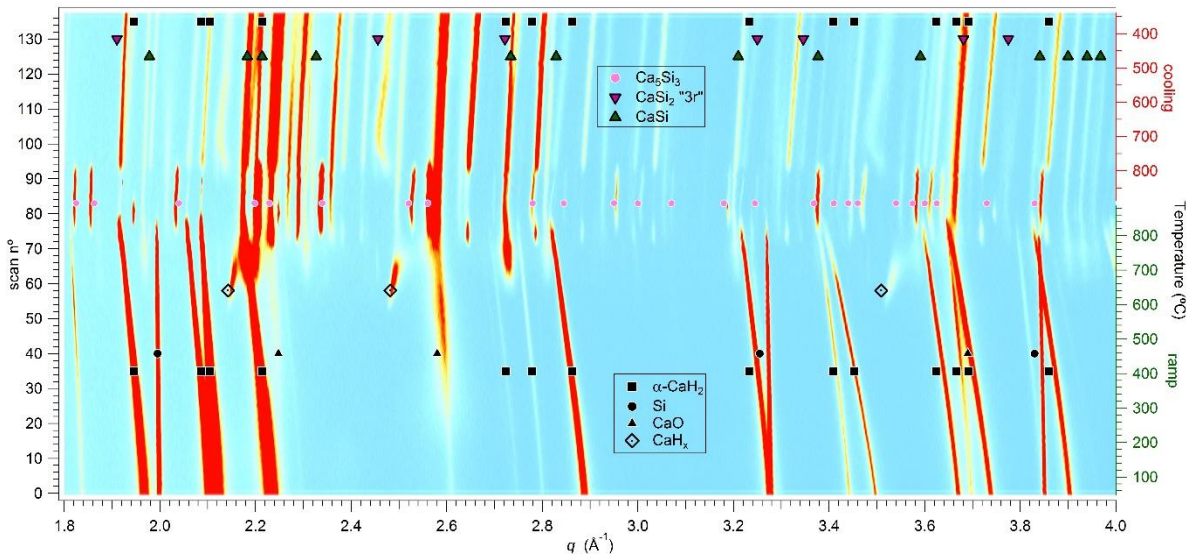

In Figure 4-23, several new phases can be observed. A reversible reaction is observed in this *in-situ* synchrotron X-ray measurement, which was conducted in a closed system under a hydrogen atmosphere. Indeed, the reversible formation of Ca_5Si_3 and CaH_2 transformation can be identified.

Nonetheless, the peak matching analysis doesn't identify all the phases formed or the different events. In order to identify the path of reaction, the unknown peaks (*a*, *b* and *c* on Figure 4-24) have been identified. Then, the evolution of the normalised intensity of each known phase and unknown phase is determined for every scan via the peak detection using Jedit associated with Topas®. The weight percent of the different unknown phases cannot be estimated by this technique because the detection was based on the evolution of a single or only 2 peaks, but it is possible to detect which phases react to obtain one of the unknown phases.

Figure 4-24: In situ synchrotron powder diffraction data for $2CaH_2$ + Si (λ = 0.59027 Å). Q factor vs number of scan and temperature. Heating ramp up to 886 °C (10 °C/min), and cooling ramp down to 338 °C under 1.5 bar H_2 back pressure.

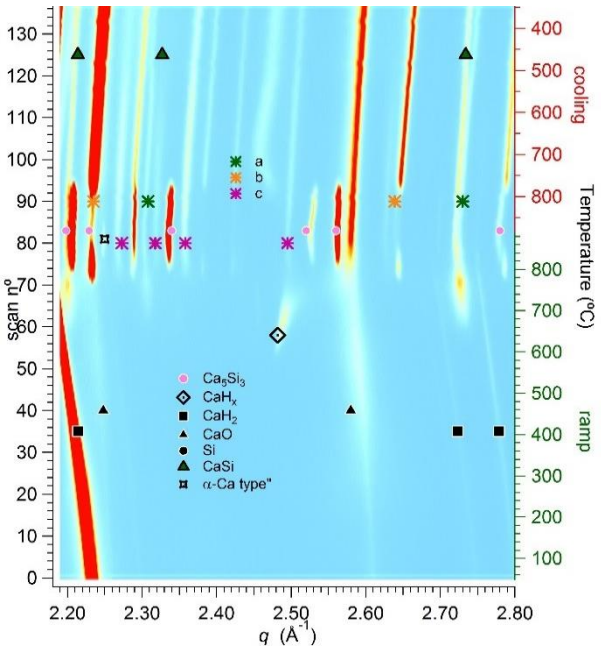

In Figure 4-23 and Figure 4-24 the following is observed:

1) For scan 53 (≈ 600 °C), CaH_2, Si and a portion of CaO react to form the solid solution CaH_x
2) For scan 62 (≈ 690 °C) CaH_x, Si and CaH_2 transform into the "unknown phase *a*" and the CaO intensity increases.
3) At scan 70 (≈ 770 °C), Si, "unknown phase *a*" and CaH_2 react to form the "unknown phase *b*" and the "unknown phase *c*". The peak intensity of the "unknown phase *c*" is negligible.
4) Ca_5Si_3 is reversibly formed. Starting at scan 72 (≈ 790 °C), "unknown phase *a*", "unknown phase *b*", CaH_2 and Si are consumed to form Ca_5Si_3 and during the cooling ramp starting at scan 86 (at T < 850 °C), Ca_5Si_3 decompose to form back CaH_x, CaH_2, "unknown phase *a*" and "unknown phase *b*". In parallel, the "α-Ca type" is formed consuming partially "unknown phase *b*" and CaH_2, but decompose at ≈ 870 °C.

Figure 4-25: Normalised peak phase intensity of known phases (CaH_2, Si, CaO, Ca_5Si_3) and unknown phases (CaH_x, a, b, c and "α-Ca type").

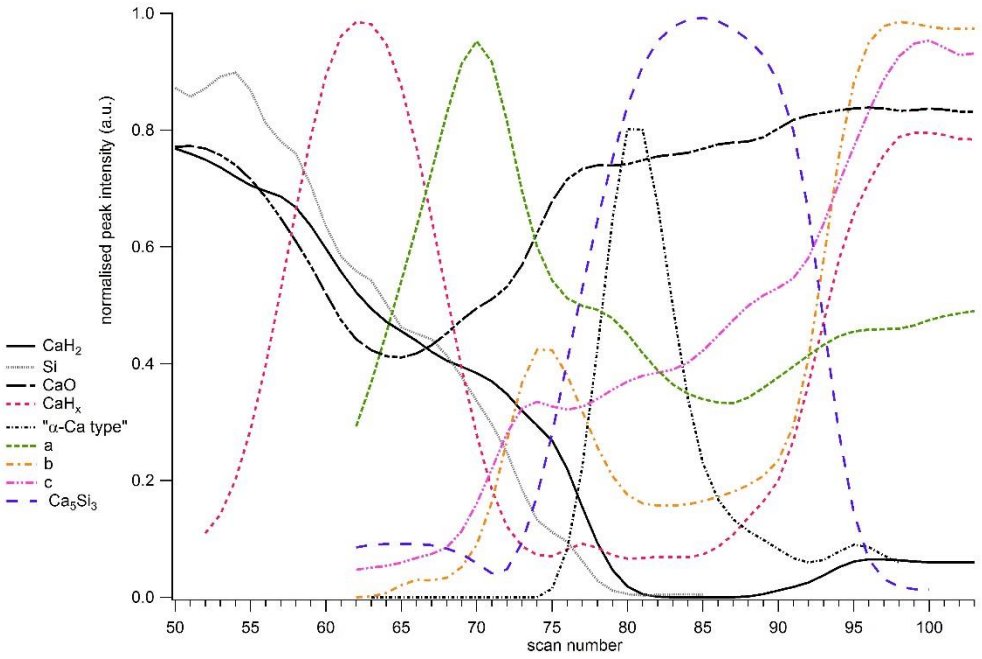

The peaks of "unknown phase a" can be estimated as corresponding to the phase CaSi. All the peaks of CaSi form at scan 62 or at ≈ 690 °C (focus on 3 peaks between 3.8 $Å^{-1}$ and 4 $Å^{-1}$ in Figure 4-23), and the 2 peaks "unknown phase *a*" are match with the CaSi peaks with an offset due to thermal expansion at high temperature. At high temperature, it couldn't be confirmed that the CaSi phase corresponded to these peaks, but instead by following the thermal behaviour during the cooling ramp it was concluded that these peaks are CaSi. Furthermore, to conclude, a reversible reaction can be described:

$$x_1CaH_2 + x_2CaH_x + x_3CaSi + x_4\text{"unknown phase } b\text{"} \rightleftarrows y_1Ca_5Si_3 + y_2H_2 \qquad \text{reaction 4-4}$$

Matching analysis on "unknown phase b" has been done and it is concluded that this phase is not Ca_3Si_4, $Ca_{14}Si_{19}$, $CaSiH_{1.3}$[80], $CaSiD_{1.19}$,$CaSiD_{0.97}$[81], or $Ca_5Si_3H_{0.53}$. Wu *et al.*[82] also described the decomposition of Ca_5Si_3 forming CaSi, CaH_2 and an unknown "amorphous" phase. "unknown phase *b*" can be the phase defined as the unknown "amorphous" phase described by Wu *et al*.

The Ca_5Si_3 formation reaction, being reversible and occurring at high temperature, has potential for reversible thermal energy storage application.

4.2.6. Pressure Composition Isothermal (PCI) analysis

Initially a PCI measurement at 520 °C was conducted on a CaH_2 + Si sample contained in a stainless-steel reactor . The temperature was limited due to technical reasons concerning the stainless-steel reactor (for more information on the reactors, see section 2.5). At 520 °C, the thermodynamic prediction showed that the predicted 3 steps of reaction can be observed (Figure A-16).

At 520 °C, the theoretical equilibrium pressure of the preferential steps for the reaction are:

- Step 1: $CaH_2 + 2Si \rightleftarrows CaSi_2 + H_2$ → 22 bar ≤ P ≤ 27 bar
- Step 2: $CaH_2 + 2CaSi_2 \rightleftarrows Ca_3Si_4 + H_2$ → 9 bar ≤ P ≤ 11 bar
- Step 3: $CaH_2 + Ca_3Si_4 \rightleftarrows 4CaSi + H_2$ → 3.5 bar ≤ P ≤ 4.4 bar

It is not possible to identify a flat equilibrium plateau (Figure A-16) on the *P* vs H_2 wt % plot but slopes with variable ramp rate to a total hydrogen weight desorbed equal to 1.86. This behaviour is characteristic of a solid solution reaction as describe by Tortoza *et al.*[25] This result can be seen in appendix A-16.

Using a silicon carbide reactor (section 2.5.3), a series of PCI measurements were conducted between 698 °C and 778 °C. Due to the specific limitation of this reactor, the pressure in the system is limited to ≈ 15 bar. The risk is that the pressure passes under the threshold of the equilibrium curve (Figure 3-8) during the temperature ramp at high temperature resulting in a part of the hydrogen being desorbed during the ramp. Indeed, it was observed during thermal analysis that the reactions occurred at < 500 °C (see figure 4-12). During the first step of the PCI measurement, a pressure drop is observable (see kinetic data in Figure 4-27). For safety reasons, the sample cell reactor was designed using a blow off valve set at a maximum pressure of 15 bar. The pressure drop is due to a blow off at a pressure too close to the safety valve limit. But the hypothesis of a slow hydrogen leakage during the measurement cannot be excluded, the pressure loss being compensated for by hydrogen desorption of the sample during the following steps. This results in an error in the calculation of the total H_2 wt %.

It is noted that the pressure doesn't equilibrate at the end of each step (Figure 4-27). The pressure at equilibrium for an infinite duration step estimation has been done on each step. It results into the same sloping curve and cannot be assimilated as a flat plateau. Therefore, it confirms the hypothesis of a solid solution behaviour is due to intrinsic properties of the materials and not to experimental reasons.

Figure 4-26: PCI measurements for $2CaH_2$ + Si between 698 °C and 778 °C using 5 hour steps and step decrement of 2 bar in a SiC reactor and the generated van't Hoff plot.

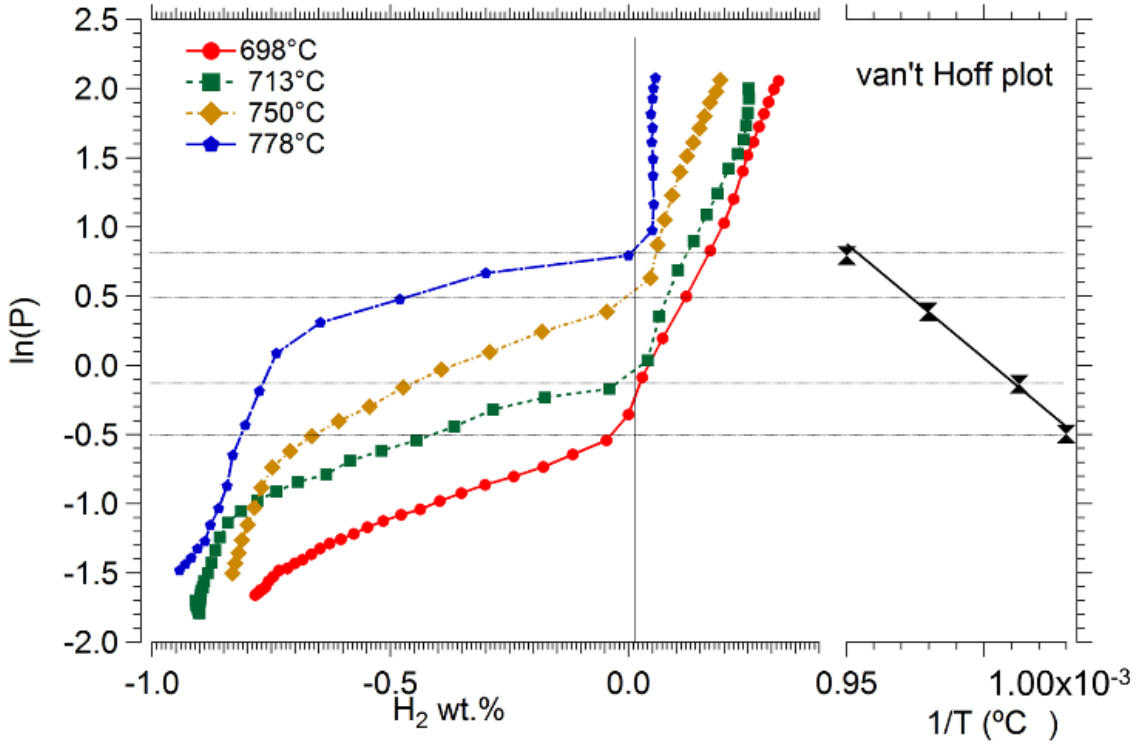

The hydrogen desorption (Figure 4-26) behaviour can be divided into 2 different sloping parts. As mentioned above, the first desorption ramp may commence at a pressure > 15 bar. More interesting is the second step of decomposition with a H_2 wt % of ≈ -0.8. Rietveld refinement after each experiment shows the formation of Ca_5Si_3, and CaO. Remaining CaH_2 has been observed after the PCI by ex-situ X-ray analysis on the 3 lowest temperature, whereas on the highest temperature a Ca_3SiO phase is observed. At high pressure, the shape of the PCI curve at 778 °C is different than for the lower temperatures. Indeed, the curve is almost vertical, which infers that between 15 bar and 2.6 bar, the sample is not desorbing hydrogen.

Based on the 4 curves in Figure 4-26 a van't Hoff plot was used to determine the enthalpy and entropy of the Ca_5Si_3 formation reaction. However, since the commencement of desorption cannot be defined precisely due to the reasons described above, a large variation is measured on the enthalpy and entropy calculation (R^2 ≈ 0.977).

The van't Hoff equation (eq. 2-4) calculated at the inflection point, the "mid-plateau" point or the end of the reaction show an enthalpy of reaction between 122 $kJ \cdot mol^{-1}$ H_2 and 143 $kJ \cdot mol^{-1}$ H_2 associated with and entropy between 123 $J \cdot mol^{-1} \cdot K^{-1} \cdot H_2$ and 140 $J \cdot K^{-1} \cdot mol^{-1}$ H_2.

Figure 4-27: kinetic data of the PCI on $2CaH_2$ + Si at 747 °C. Step duration = 5 hours. Step increment = 2 bar.

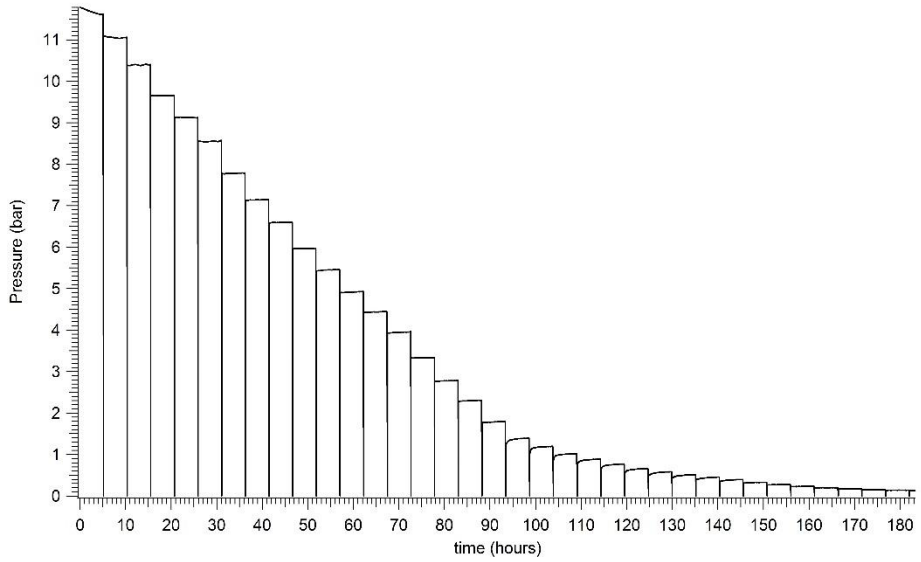

A PCI measurement was conducted at a temperature of 820 °C (see figure 4-28). The first reason was to observe if the behaviour of this material at higher temperature is similar to that at 778 °C. This would mean that over a threshold of temperature, the path of reaction is different than above. Secondly, this experiment has been done by measuring the H_2 wt % during the ramp rate in order to know the total weight percent of hydrogen loss during the measurement.

Figure 4-28: PCI measurement for $2CaH_2$ + Si at 820 °C using 5 hour time steps and pressure step increments of 2 bar in a SiC reactor.[‡‡‡‡]

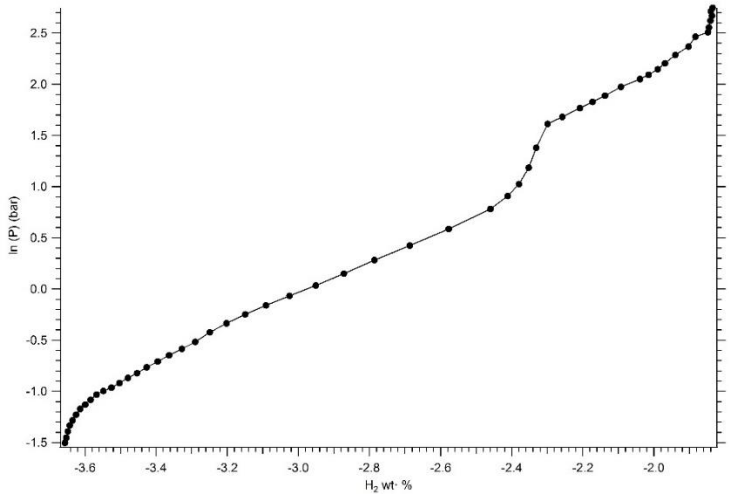

This result can be observed in Figure 4-28. During the heating ramp to reach 820 °C before starting the PCI measurement, 1.83 wt % of hydrogen desorbed was measured. The starting point of the PCI curve is shifted by this value on the figure. Furthermore, a slow leakage was found during the measurement. A drop-in pressure was observed on the high temperature plateau during the first 10 hours using a SiC reactor. This can be explained by the permeability of the reactor, but also after this period a linear pressure decrease was observed (see section 2.5.2). A ΔP due to a leakage by diffusion is defined as a function of the square of the pressure.[83, 84] A leak rate correction has been estimated on the first steps of the PCI curve before hydrogen desorption steps. In addition to this, the correction due to absorption and desorption of hydrogen in the stainless-steel sample cell is calculated as usual.

At this temperature the hydrogen desorption can be divided into two distinguishable steps. Up to 0.45 H_2 wt % is desorbed in a first step between 15 and 5 bar and then 1.2 H_2 wt % is measured during the second step of the reaction.

It is possible to determine pairs of ΔH and ΔS at the mid-point for each step of the reaction:

1. High pressure step: Mid-point = 7 bar. For ΔS = 110 ± 10 $J \cdot K^{-1} \cdot mol^{-1}$ H_2;
   ΔH = 102 ± 11 $kJ \cdot mol^{-1}$ H_2
2. Low pressure step: Mid-point = 0.5 bar. For ΔS = 110 ± 10 $J \cdot K^{-1} \cdot mol^{-1}$ H_2;
   ΔH = 121 ± 11 $kJ \cdot mol^{-1}$ H_2

[‡‡‡‡] The safety valve limit pressure was set at 30 bar for this experiment in order to avoid any issue due to blow off from the safety valve.

4.3. Analysis and discussions

As shown in the preliminary TPD measurement, the confinement of the hydride is an important factor for the desorption efficiency. Indeed, traces of oxygen or water drive to the formation of a calcium hydroxide and this phase release hydrogen at low temperature and form CaO.

Several Ca_xSi_y can be decomposed accompanied by hydrogen absorption at different temperatures as describe by Wu *et al*.[73, 81], Aoki *et al*.[85], Anikina *et al*.[86] It has been shown that the difference between the thermodynamic predictions is due to the formation of a hydrogenated solid solution. A comparative calculation has been done using as reference the thermodynamic data calculated by Wang *et al*.[30] and the one in the HSC database.[57] A difference of ± 50 °C has been observed in the temperature of reaction but the path of reaction was identical for these two references. In both references, the C_p values have been estimated using approximations: at high temperature the value of Barin *et al*. is estimated as constant, which is consider as correct for the liquid phase but not for the solid phase, and the model by Wang *et al*. results in an overestimation of C_p at room temperature (54 $kJ.mol^{1}.K^{-1}$ instead of 40 $kJ.mol^{-1}.K^{-1}$).

The reactions between CaH_2 and Si occur in 2 main steps:

- Under 600 °C, CaH_2 and Si reacts to form the $CaSi_2$ and CaSi compounds and an unknown Ca_xSi_y phase (Figure 4-11 and Figure 4-23). For an initial stoichiometry with a ratio $CaH_2/Si \leq 1$, the reaction stops at this step with a final mixture of $CaSi_2$ and CaSi as shown in Table 4-1.
- Over 600 °C, the phase Ca_5Si_3 is formed from CaH_2, CaH_x, CaSi and an unknown phase.

The in-situ synchrotron X-ray analysis of CaH_2 helps to understand the path of reaction. The initial α-CaH_2 decomposes to a β-CaH_2 type phase starting at around 580 °C. This phase acts as a solid solution "CaH_x", and contracts due to silicon substitution and/or hydrogen vacancies. This contraction is consistent with an endothermic behaviour observed by the DSC measurement (Figure 4-12).

Also, an unknown intermediate phase has been observed, which explains the difference between prediction and experiment. As seen in Figure 4-29, this unknown phase has been observed by a collaborative partner; the Savannah's River National Laboratory (SRNL) team. This phase was also described by Armbruster *et al*.[72] as a hydrogenated $CaSiH_x$ phase.

Figure 4-29: Comparison between scan 136 (360 °C after cooling) and metallic Ca_2Si obtained by SNRL in the dehydrogenated state after cycling 6 times.[87]

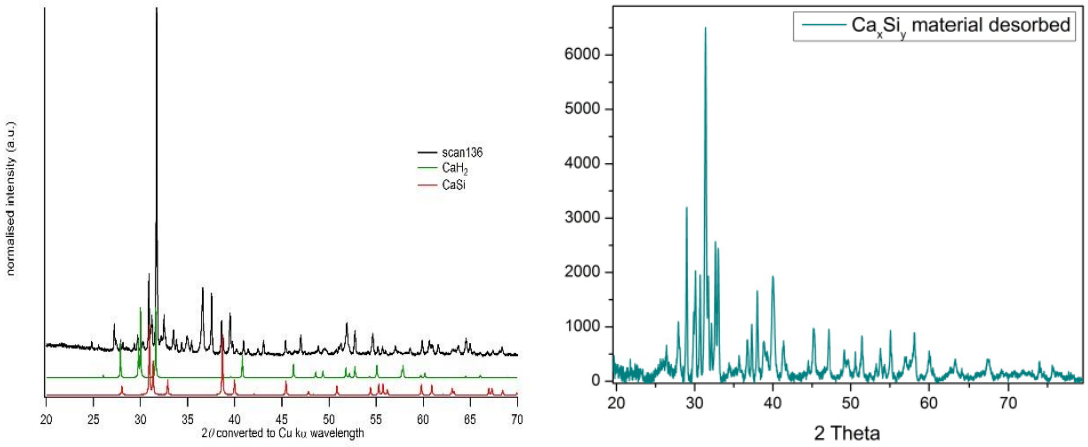

The *in-situ* synchrotron X-ray analysis for $2CaH_2 + Si$ (Figure 4-23) suggests that the formation of Ca_5Si_3 is the reversible reaction exploitable for thermal energy storage (TES) application. The formation of this unknown phase may be irreversible and is probably the cause of the difference between the thermodynamic prediction and the experimental results (different temperature of reactions and no traces of Ca_3Si_4).

The reaction resulting in the Ca_5Si_3 formation has been described also by SRNL[87]. An enthalpy of 111 $kJ \cdot mol^{-1} H_2$ has been calculated by the DSC technique and a H_2 wt % of 1.2 was determined (Figure 4-30). SRNL experimented a TGA measurement after cycling 6 times with a $Ca_2Si + H_2$ initial composition at 675 °C under 64 bar of hydrogen. 1.2 wt % of hydrogen. This reaction corresponds to the lower pressure plateau measured on the PCI measurement at 820 °C (Figure 4-28) without loose of efficiency after 6 cycle.

Figure 4-30: TGA/RGA analysis of hydrogenated Ca_2Si after 6 cycles at 675 °C and 64 bar H_2, obtained by SNRL.[87]

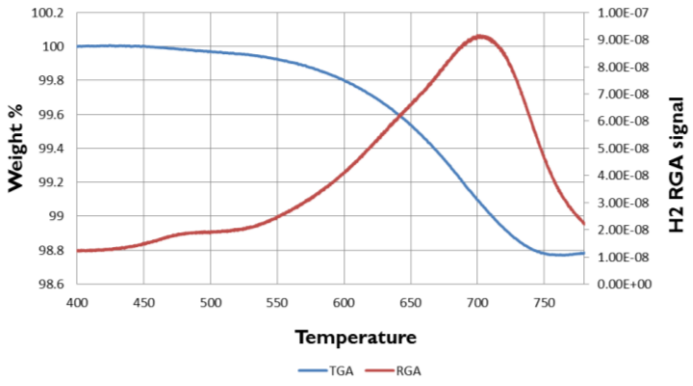

In order to validate the potential of the calcium hydride-silicon system, the enthalpy and hydrogen weight percent desorbed for the calcium hydride- calcium silicide results had been compared with a recent example of TES material analysed by Ward *et al.*[88]: the calcium hydride- aluminium system. CaH_2 and Al react in a 2-step reaction resulting in an enthalpy of reaction of 74 $kJ \cdot mol^{-1} \cdot H_2$ and 83 $kJ \cdot mol^{-1} \cdot H_2$ respectively which give a total experimental gravimetric heat storage capacity of 765 $kJ \cdot kg^{-1}$ with a hydrogen capacity of 1.9 wt % at 600 °C for both reaction together. The $2CaH_2$-Si system results in a gravimetric heat storage capacity between 660 $kJ \cdot kg^{-1}$ for a single step reaction desorbing 1.2 wt % and 807 $kJ \cdot kg^{-1}$ for 2 steps of reaction desorbing 1.65 wt % in total, respectively and an enthalpy of reaction estimated at 111 $kJ \cdot mol^{-1}$ H_2.

4.4. Conclusion

The reaction between CaH_2 and Si, occurs in a multistep reaction. The phases CaSi, $CaSi_2$ are formed under 600 °C and are not viable for TES applications. However, the reversible decomposition of Ca_5Si_3 into CaSi, an unknown Ca_xSi_y phase, CaH_2 (and its high temperature form "CaH_x") and resulting in the desorption of up to 1.2 wt % of hydrogen occur at the required range of temperature for application. Depending on the change of temperature during a day and night cycle, the formation of a solid solution able to absorb and desorb hydrogen might add an extra hydrogen storage capacity and an extra source of energy during the absorption time.

To conclude the system of calcium hydride destabilised by CaSi has the potential for TES comparable with the Al-destabilised CaH_2. For field application, the abundance and low price of silicon are promising argument for a large scale and sustainable application.

5. The CaH_2+2C system

5.1. Introduction

Reich *et al*.[37] mentioned that calcium hydride might react in the presence of carbon and oxide, forming a calcium carbide structure. Later, Goerrig[89] patented the process for the production of calcium hydride via the reaction of calcium carbide with hydrogen. The reaction results in the primary products of CaH_2 and C_2H_2. It is mentioned that the acetylene releasing (C_2H_2) formation is not dependent on the experimental conditions and is always present during the reaction process. Reich *et al.*[37] and Goerrig[89] revealed an optimal temperature between 500 °C and 600 °C under 1 bar hydrogen atmosphere for the reaction:

$$CaH_2 + 2C \rightleftarrows CaC_2 + H_2 \quad \text{Equation 5-1}$$

Thermodynamic calculations confirmed this observation with an equilibrium temperature suitable for TES application. The reference for the CaC_2 (IV, *I4/mmm* structure) thermodynamic values is Ji *et al.*[90]:

- $T_{(1bar)}$ = 492 °C
- $\Delta H_{rxn}^{T(1bar)}$ = 125.9 kJ·mol^{-1} H_2
- $\Delta S_{\mathrm{rxn}}^{T(1bar)}$ = 164.5 J· K^{-1}·mol^{-1} H_2
- H_2 wt % = 3.05

As developed in chapter 3, the low price of carbon and its low molar mass makes carbon an interesting candidate for the destabilisation of calcium hydrides. The gravimetric heat storage capacity was measured to be 1904 kJ.kg^{-1} (see section 3.3.4) which is a very important argument for TES application on field. Nevertheless, the possibility of releasing acetylene may be a barrier to the cyclability of this material. Indeed, it involves a loss of the carbon contained in C_2H_2 and leads to a lack of carbon in stoichiometry.

The objective in the following sections is to observe by mass spectrometry the gas released during the desorption process and the path of reaction by *in-situ* synchrotron X-ray analysis. TGA and DSC analysis were used to confirm the heat exchange during the desorption process and sorption analysis was used to determine the gas releasing process of this system.

Expanded natural graphite (ENG) powder, pre-heated at 400 °C during 2 hours in order to eliminate traces of moisture was used in the experiments presented in this chapter. ENG was mixed with calcium hydride provided by Sigma Aldrich® (95 % pure CaH_2) and ball milled for 3 hours. 2 grams of the mixture of CaH_2 + 2C composition (M_I = 0.8 g or 38.6 wt % with $M_{(CaH2)}$ = 1.27 g or 61.4 wt %) was ball milled with 40 grams of stainless-steel balls. The result of the X-ray analysis after ball-milling is shown in Figure 5-1:

Figure 5-1: X-ray powder analysis of Ball milled CaH_2 + 2C mixture.

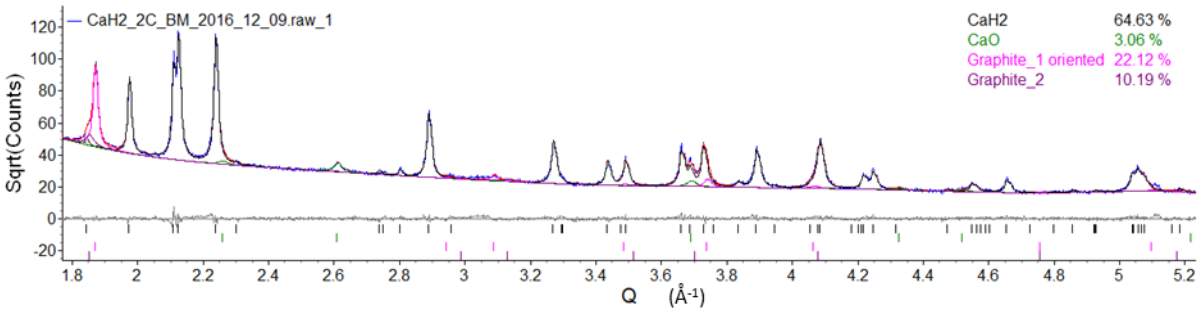

- C (graphite) = 22.12 + 10.19 = 33.5 wt %
- CaH_2 = 63.40 wt %
- CaO = 3.09 wt %

The weight percent of carbon is lower than expected (33.5 wt % instead of 38.6 wt %); this may be due to the ball milling process or because the X-ray analysis underestimates the proportion of C. Indeed, the quantification of the carbon by quantification X-ray analysis using Topas is based on the main peak of carbon (at $q \approx 1.8$ Å^{-1}), which may cause a relative error in the quantification. According to the Topas© software, the error in the phase quantification for a multiple peak fitting is ≈ 10%. However, the error can be larger for a single peak fitting. On the other hand, it cannot be excluded that the material is not outgassing during the ball milling due to the heat produce by the friction produced from the balls.

In order to confirm the observations (cf. reaction 5-1 and acetylene release) from Reich *et al.*[37] and Goerrig[89], simultaneous thermal analysis measurements were conducted on this sample under an argon atmosphere at 10 °C/min. The mass spectrometry analysis helped determine the different types

of gas released during the heating ramp. In Figure 5-2, the two main types of gas observed are plotted. This experiment was conducted twice by Professor Kondo-Francois Aguey-Zinsou and his team at UNSW. In both experiments, hydrogen is released in a first step (2 peaks at 230 °C and 320 °C respectively), between 100 °C and 370 °C prior to the release of acetylene gas between 380 °C and 500 °C. As observed in the previous chapter (chapter 4.2.4.1), the release of H_2 at low temperatures is due to the presence of $Ca(OH)_2$ which forms CaO and releases hydrogen at low temperature. The main peak of hydrogen desorption starts at ≈ 500 °C, reaches a maximum at 645 °C and finishes at 720 °C.

Figure 5-2: Normalised intensity of the major components of gas released measured by mass spectrometry on the CaH_2 + 2C sample under Ar atmosphere at 10 °C/min up to 890 °C.

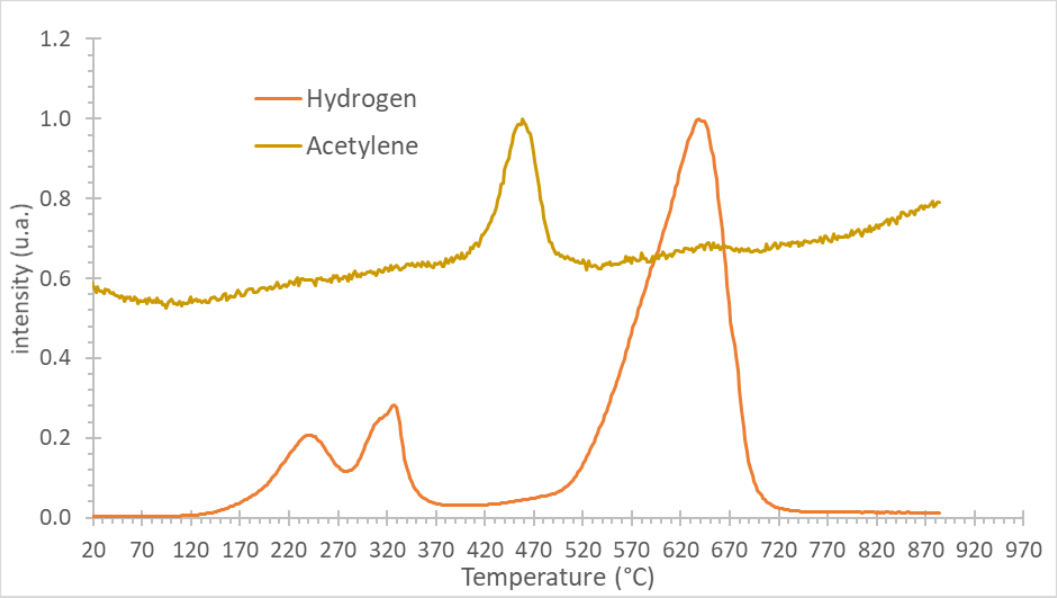

The different steps of reaction are confirmed by the TGA and DSC (Figure 5-3). These measurements were measured simultaneously with the MS measurement from in Figure 5-2. Below 500 °C, up to 0.55 wt % of gas released is measured on the TGA measurement (blue line). This step of reaction is exothermic according to the DSC measurement (red line). This result has been repeated and is surprising. Indeed, either the hydrogen and the acetylene desorption should be endothermic reactions. Further investigations are required to understand this behaviour. Above 500 °C, an endothermic reaction occurs. The TGA measurement shows that up to 2.25 wt % of gas is released. Above 720 °C, an endothermic reaction without gas release is observed. This may be due to a phase transition.

Up to 3.05 wt % of hydrogen is contained in the initial composition. The difference between this value and the total of hydrogen released during the STA measurement(2.83 wt % at the end of the TGA measurement) can be due to the release of acetylene, which involves less carbon being available to react with calcium hydride.

Figure 5-3: Simultaneous Thermal Analysis on CaH_2 + 2C. DSC and TGA under vacuum at 10 °C/min up to 900 °C.

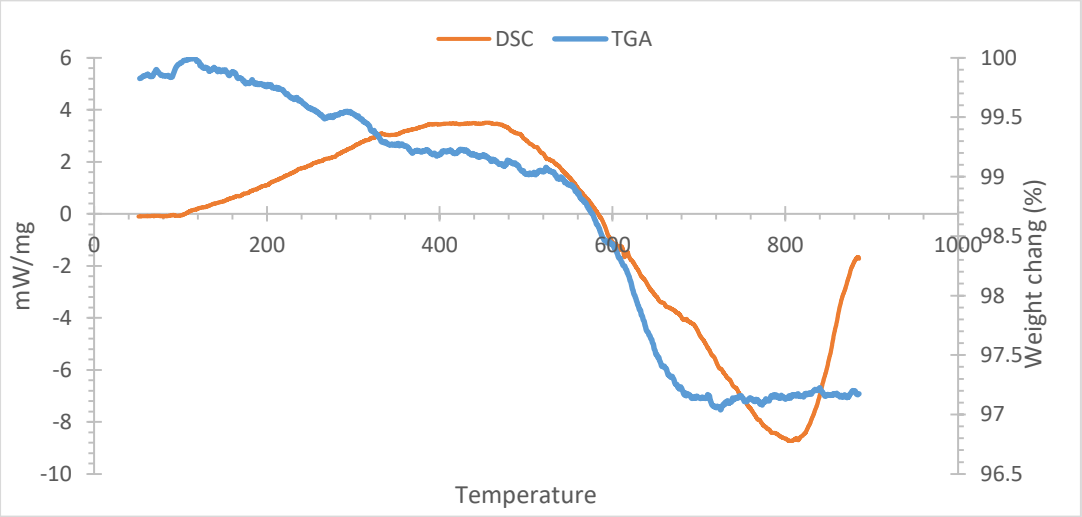

A TPD measurement was conducted during the first part of the heating ramp up to 630 °C and then the temperature was raised to 716 °C (Figure 5-4-a). 2.38 wt % of gas is desorbed during the first step, then up 0.33 wt % of gas is desorbed during the second part of the heating ramp between 630 °C and 716 °C, reaching a maximum of 2.8 wt % before stabilising the total weight percent to 2.71 wt %. The different steps of gas release described above are shown in Figure 5-4-b. Between 100 °C and 370 °C ≈ 0.25 wt % of gas (hydrogen?) is released and between 370 °C up to 500 °C,≈ 0.3 wt % of gas (acetylene?) is released. The largest gas release occurs above 500 °C, stabilising the total gas released at 2.71 wt %. The different steps of reaction match with the thermal analysis:

- The first step of gas desorption (0.25 wt %) commencing at ≈ 200 °C matches with the $Ca(OH)_2$ decomposition.
- The second step of gas release (0.3 wt %) at ≈ 400 °C corresponds to the acetylene release observed by mass spectrometry (Figure 5-2).

  The third and principal step of desorption (up to 2.71 wt %) consistent with reaction 1 of the desorption process. This reaction desorption is equivalent with the one measured by TGA (Figure 5-3). Over 500 °C an endothermic hydrogen release occurs.

Figure 5-4: TPD measurement on CaH_2 + 2C at 5° C/min. left : Temperature (in °C) and pressure (in bar) vs time (in hours). a) experimental conditions: temperature (°C) (blue line) and pressure (bar) (orange line) versus time. b) hydrogen weight percent calculated during the heating ramp: H_2 wt % vs temperature (°C[§§§§]).

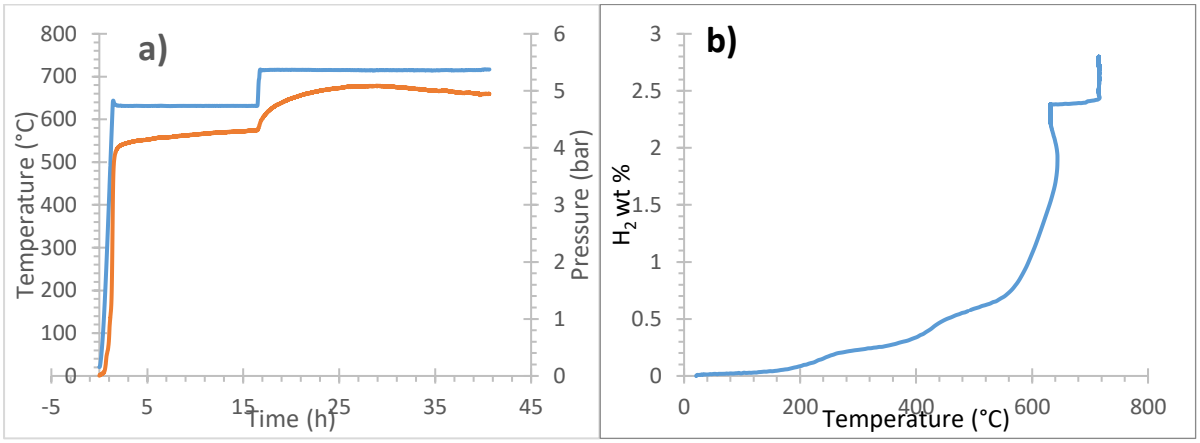

The X-ray analysis conducted after the TPD showed:

- CaC_2 (*C2/c* and *C2/m* structures) = 91.4 wt %
- CaH_2 = 5.2 wt %
- CaO = 3.4 wt %

The presence of CaH_2 leftover after the TPD measurement may be due to the loss of carbon, via acetylene gas being released. Calcium carbide has a monoclinic structure (*C2/c* and *C2/m*), observed after cooling the system down and by *ex-situ* X-ray analysis as described by Konar *et al.*[91], who predicted a tetragonal structure (*I4/mmm*) unstable at room temperature, but present at high temperature. From the *in-situ* synchrotron X-ray analysis (Figure 5-5), the formation of this structure is the result of CaH_2 and C being consumed. During the cooling ramp at ≈ 470 °C, this phase transforms into the monoclinic CaC_2 II (*C2/c*). On the other hand, no trace of the monoclinic structure CaC_2 III (*C2/m*) was found.

These results show that the calcium hydride destabilisation with carbon reduces the hydrogen desorption temperature to ≈ 720 °C. The PCI measurement shows that ≈ 0.35 wt % of gas is reversibly desorbed and absorbed. This has only been done for one cycle. The PCI and the cycling analysis needs

[§§§§] the curve goes slightly backwards near ≈ 2 – 2.5 wt % in Figure 5.4 (b) due to the stabilisation of the temperature. Indeed, in Figure 5.4 (a), it can be observed that the temperature goes up to 660 °C before stabilising to 640 °C at the beginning of the plateau.

to be repeated for a confirmation of this results in order to settle the non-cyclability of this system. This phenomenon may be due to a phase transition during the cooling process from a tetragonal structure (*I*4*/mmm*) to a monoclinic structure (*C*2*/c*). The tetragonal structure may not be stable for hydrogen absorption.

Figure 5-5: In situ synchrotron X-ray analysis of CaH_2 + 2C under 1 bar of hydrogen (λ = 0.59027 Å). Temperature ramp of 10 °C/min up to 887 °C then cooling down to 320 °C.

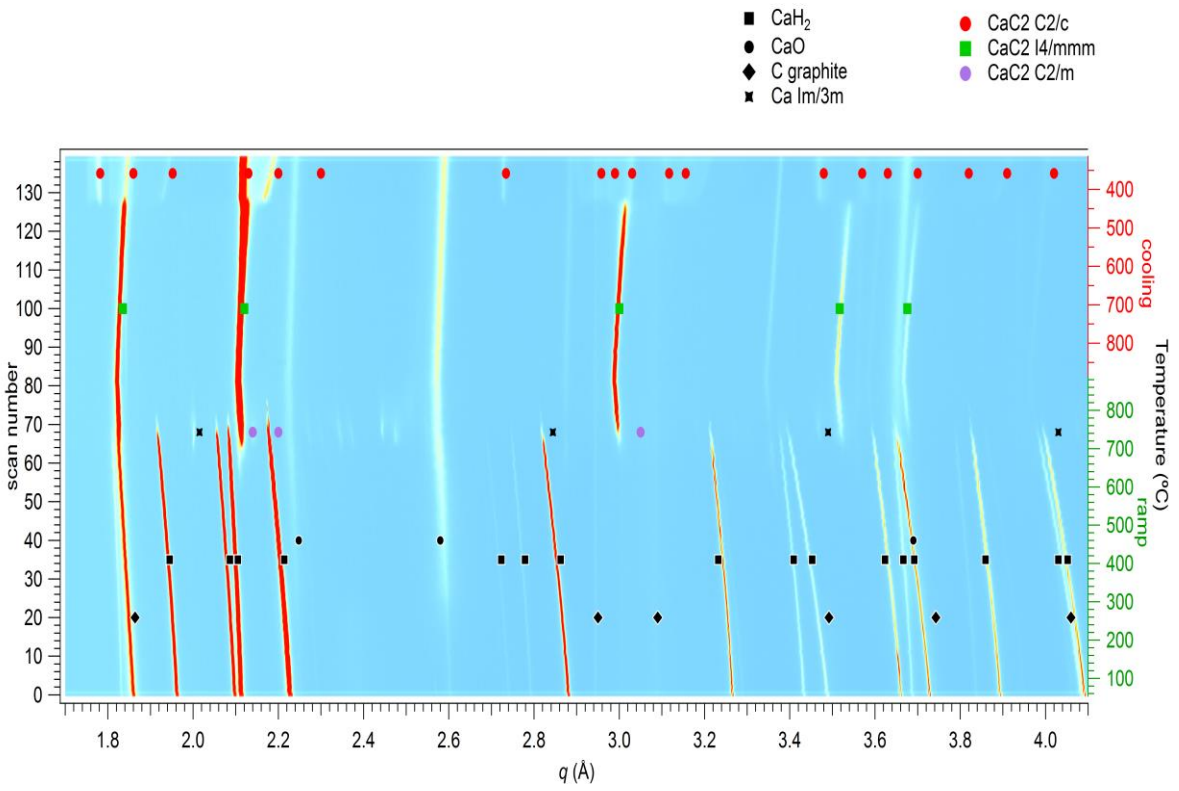

.

5.2. Conclusion and perspectives

A brief analysis has been conducted on the reaction between CaH_2 and C. Thermal analysis, and specifically mass spectrometry, reveal that a gas other than hydrogen was released. Acetylene was formed during the temperature ramp below 500 °C. *In-situ* synchrotron X-ray analysis has determined the temperature of reaction between CaH_2 and C, as well as the structures of CaC_2 formed during the heating and cooling ramps.

Unfortunately, the formation of acetylene gas is problematic for the reversibility of the hydrogen desorption reaction as well as the phase transition during the cooling process. Furthermore, thermal

analysis is required to determine the enthalpy for each reaction. On the other hand, the prediction relative to the reaction $CaH_2 + 2C \rightleftarrows CaC_2 + H_2$ Equation 5-1were confirmed by the different analyses. Effectively, CaH_2 and C react to form the CaC_2 (*I4/mmm*) around 500 °C.

This system requires further investigation. The literature and, in particular the Goerrig patent,[89] mentions that substances such as N_2, S, NH_3, H_2S, NaS, CaS or Na may act as catalysts. However, it is also specified that sodium can react with hydrogen to form sodium hydride. These substances increase the speed of reaction but may also change the path of reaction and the product of reaction. It is also suggested in the literature that reducing the reactant powder size and/or increasing the temperature ramp rate may avoid the release of acetylene as a product of the reaction. At this stage, it is not possible to determine the viability of this system for high temperature hydrogen storage applications.

6. The CaH_2 + MgO system

6.1. Thermodynamic calculation

In 1935, Alexander P.P. patented a method for the production of calcium hydride from calcium oxide and hydrogen in the presence of metallic magnesium.[92] This method described the following reaction:

$$CaO + Mg + H_2 \rightleftarrows CaH_2 + MgO \qquad \text{reaction 5-1}$$

The interest for this reaction is that lime associated with magnesium can be used as a starting material. CaO, the price of which is more than twenty times lower than CaH_2 (See section 3.4), is abundant and can be directly extracted from mines as crushed stones.[61, 93] Magnesium hydride is a well-known material for its metal hydride applications, owing to its favourable cost, high gravimetric and volumetric hydrogen densities and low application temperature. [3,94]

The thermodynamic predictions from data collected by Islam *et al.*[95] on the oxide phases, by Dinsdale *et al.*[51], on the pure elements and by Hillert *et al.*[68] on the Mg-Ca structures, confirmed that reaction 8-1 is the preferential reaction and the following conclusions can be drawn:

- $T_{1bar} = 812$ °C
- $\Delta H_{rxn}^{T(1bar)}$ = 141.2 kJ·mol^{-1} H_2
- $\Delta S_{rxn}^{T(1bar)}$ = 130.1 J· K^{-1}·mol^{-1} H_2.
- H_2 wt % = 2.45

Figure 6-1: Equilibrium composition at 1 bar according to the temperature set for an initial mixture of CaH_2 and MgO.

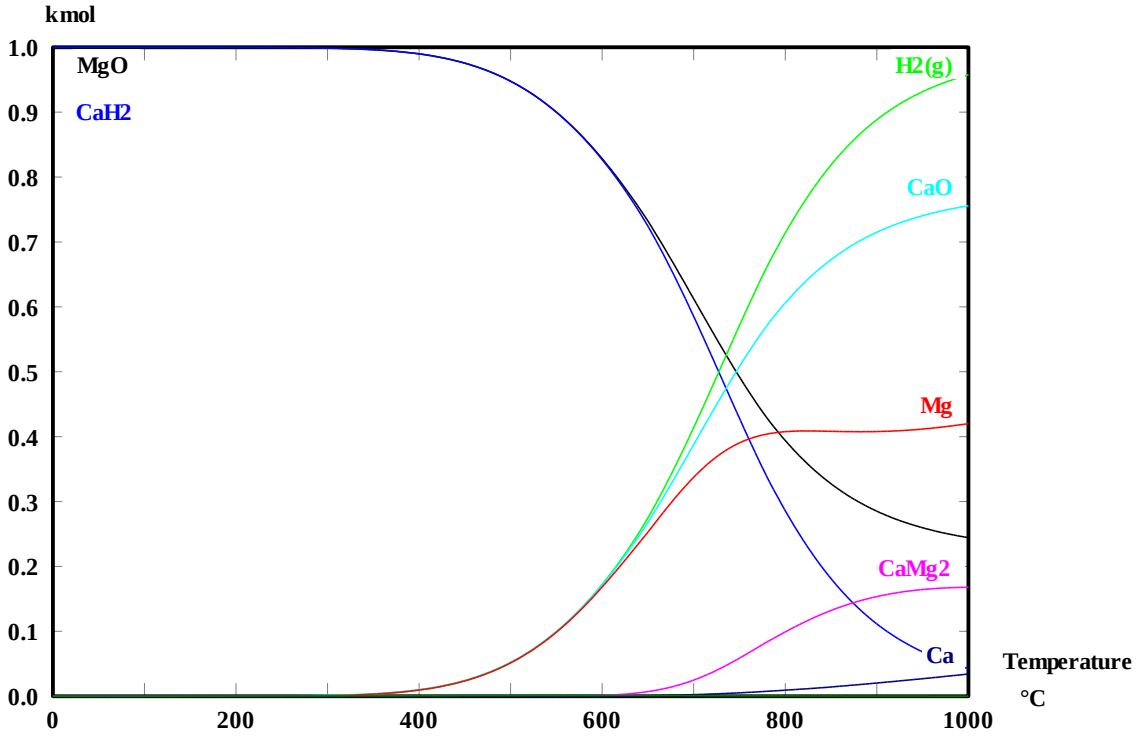

Either the formation of solid solutions between CaO and MgO composed of the pure CaO or MgO phase with insertion of Mg or Ca respectively as described by Doman *et al.*[96] (Figure A-15) or the formation of $CaMg_2$ compound shown on Figure 6-1 may interfere with the reaction, driving it to irreversible reactions resulting in this material being less interesting as a thermal energy storage option. Also, the low vapour pressure of the metallic Mg could be an issue.[4] Indeed, Mg evaporation would cause an imbalance in the stoichiometry during cycling or segregation if the gas is not contained. Despite these different points to consider when studying this material, the results of the thermodynamic prediction confirmed the potential of this system for TES applications: a hydrogen release temperature between 600 °C and 800 °C with a high enthalpy of reaction.

6.2. Experimental and discussions

This section compares thermal analysis, *in-situ* synchrotron X-ray analysis and sorption analysis results.

Figure 6-2: Simultaneous Thermal analysis of CaH_2 + MgO composition under Ar conditions at 10 °C. The black line is the mass spectrometry of the hydrogen signal and the red line is the weight change in wt %.

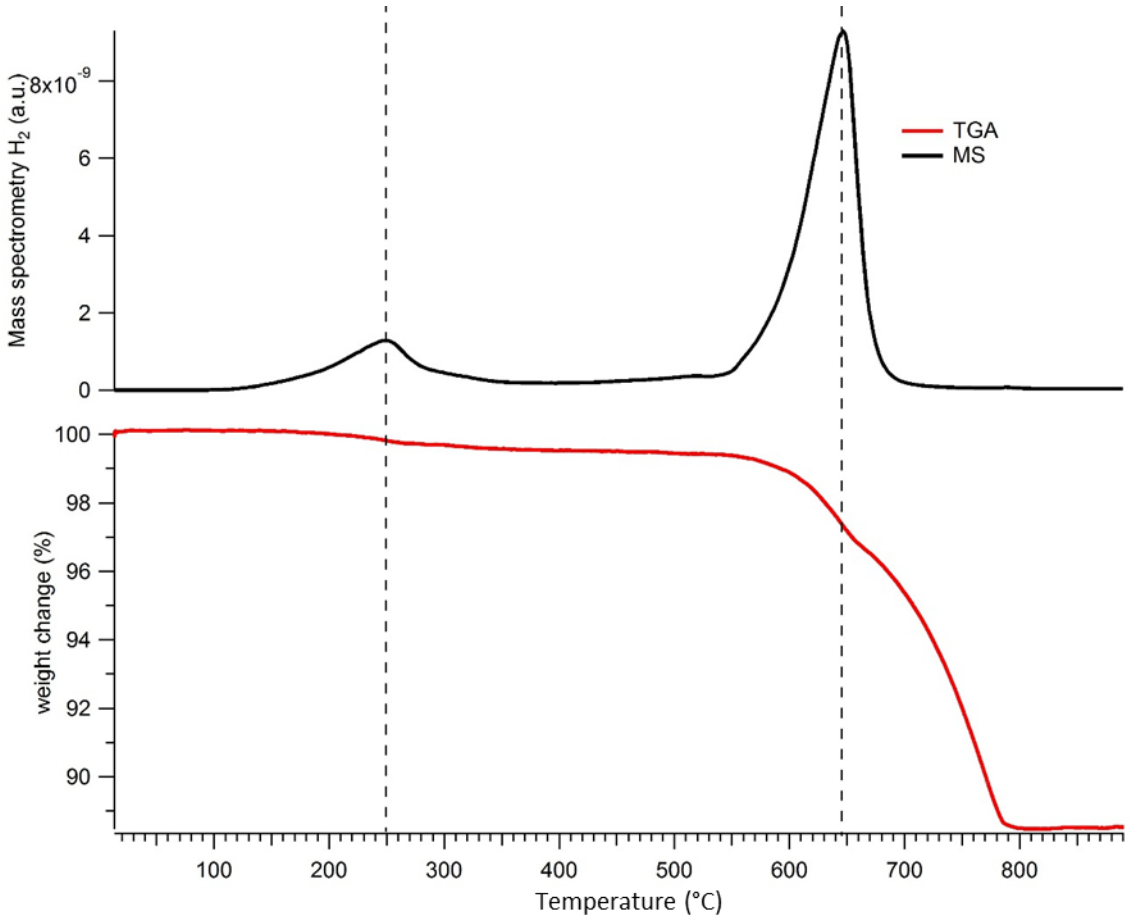

Two peaks of hydrogen release can be observed in Figure 6-2. A quantity of hydrogen (0.5 wt %) is released between 200 °C and 300 °C (as shown in section 4.2.4) due to the calcium hydroxide impurities contained in the raw material (CaH_2 provided by Sigma Aldrich® purity = 95 wt %). Between 540 °C and 700 °C, the hydrogen desorption reaction occurs with a maximum at 645 °C. It is observed on the TGA curve, at the end of the hydrogen desorption (700 °C), that 3 wt % is lost in the process. This value matches the theoretical hydrogen weight percent (2.45 wt. %) contained within the material. The extra 0.5 wt % hydrogen was lost at low temperature. If exposed at a higher temperature than 800 °C the sample loses up to 11.5 wt % because the Mg gas evaporates. An inflection in the

curve can be observed above 700 °C. Before and after this temperature point, it can be estimated that the weight loss is due to several different reactions that are analysed in the following paragraph.

Firstly, according to the DSC results (Figure 6-3), an endothermic reaction starts as the temperature is reaching 650 °C. This temperature matches the melting point of Mg. The reaction between CaH_2 and MgO start at this temperature and the metallic Mg is formed in a liquid or gas form. Then the inflection in the heat exchange (between 570 °C and 650 °C) might be due to the solidification of the magnesium on the walls which is an exothermic reaction. Above 800 °C it can be observed that heat being exchanged in the process. This effect could be due to residual Ca or CaH_2 melting. The calcium is melting at 842 °C and the calcium hydride is at 816 °C.

The conclusion is that at high temperature the heat exchange is partially due to the hydrogen desorption but also partially due to the phase transformation of the reactant. Secondly, two endothermic reactions can be observed on Figure 6-3. The first one is starting as the temperature is reaching 100 °C and the second one is starting at 540 °C. The same starting point of the hydrogen release can be observed via MS. MS shows that the hydrogen release is triggered at the same temperature point.

Figure 6-3: DSC analysis of CaH_2 + MgO under vacuum up to 900 °C at 10 °C. Insert: zoom on the endothermic reaction between room temperature and 700 °C and between 0 mW/mg and 1 mW/mg.

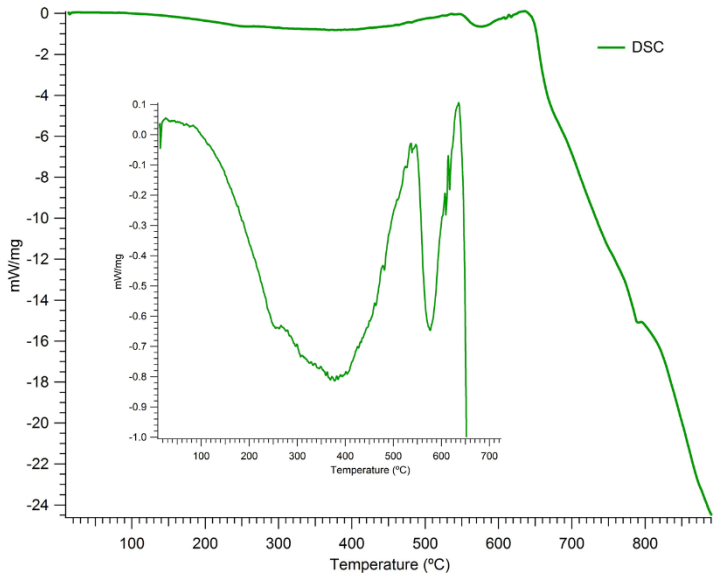

Figure 6-4: In situ synchrotron plot of CaH_2 + MgO under 2 bar of hydrogen (λ = 0.59027 Å). Temperature ramp of 8°C/min up to 887 °C then cooling down to 380 °C.

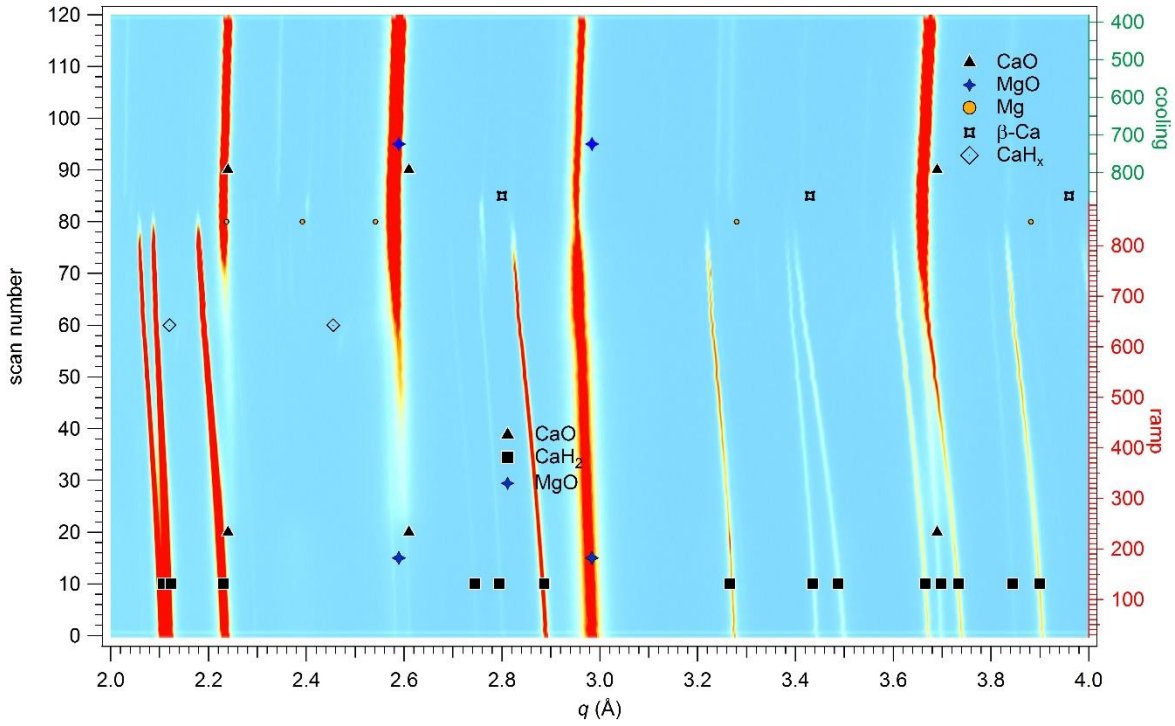

Figure 6-5: phase identification of scan number 40 (at 450 °C). Observation of the CaH_2, CaO and MgO phase. Potential identification of the Mg metal phase main peak as a shoulder on the CaO peak.

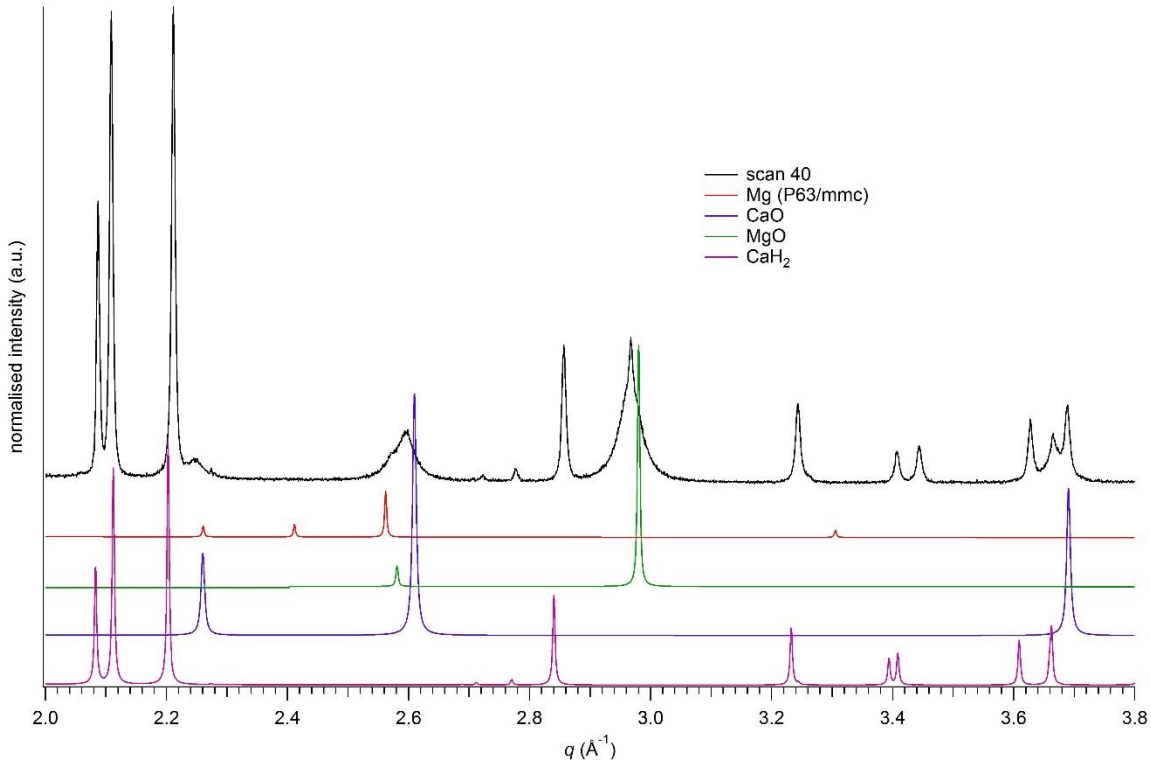

The results in figure 6-3 are confirmed by the *in-situ* X-ray analysis (Figure 6-4). CaO begins to form at scan number 20 (≈ 230 °C) consuming CaH_2, which in turn is completely consumed by scan number 80 (or 850 °C). The *in-situ* X-ray analysis experiments were conducted under 2 bar of hydrogen. An offset in temperature between *in-situ* X-ray analysis and the thermal analysis done under vacuum is expected. On scan number 40 (≈ 450 °C), the shoulder of the CaO peak at 2.58 Å is matching the main peak of Mg (Figure 6-5). The analysis of scan number 80 at 850 °C (Figure 6-6) shows that the peaks of Mg (*P63/mmc*) are matching with the observed pattern. Since Mg melts at 650 °C, it is assumed that the beam size is larger than the heated zone or it has shifted. This infers that part of the sample is not at the calibrated temperature.

According to this phase identification, at high temperature, the main phases observed are probably the solid solutions $Ca_{0.88}Mg_{0.134}O$ and $Mg_{0.964}Ca_{0.036}O$ as described by Hillert *et al.*[68] as shown in the phase diagram (see appendix figure A-15). As the phase diagram shows, a part of those solid solutions is formed at high temperature at the limit of the concentration in CaO and MgO without creating intermediate phases of CaO*MgO. During the measurement, it has been observed that the capillary broke during the cooling ramp. However, the presence of the oxide phases in the measurements can be an indication that the structural integrity has started to weaken at high temperatures during the heating process.

Figure 6-6: Phase identification of the scan number 80 (≈ 850 °C). of in-situ Synchrotron X-ray analysis on CaH_2 + MgO Qualitative comparison with the CaO, MgO phases, solid solutions : $Ca_{0.88}Mg_{0.134}O$, $Mg_{0.964}Ca_{0.036}O$, the pure β-Ca and α-Ca.

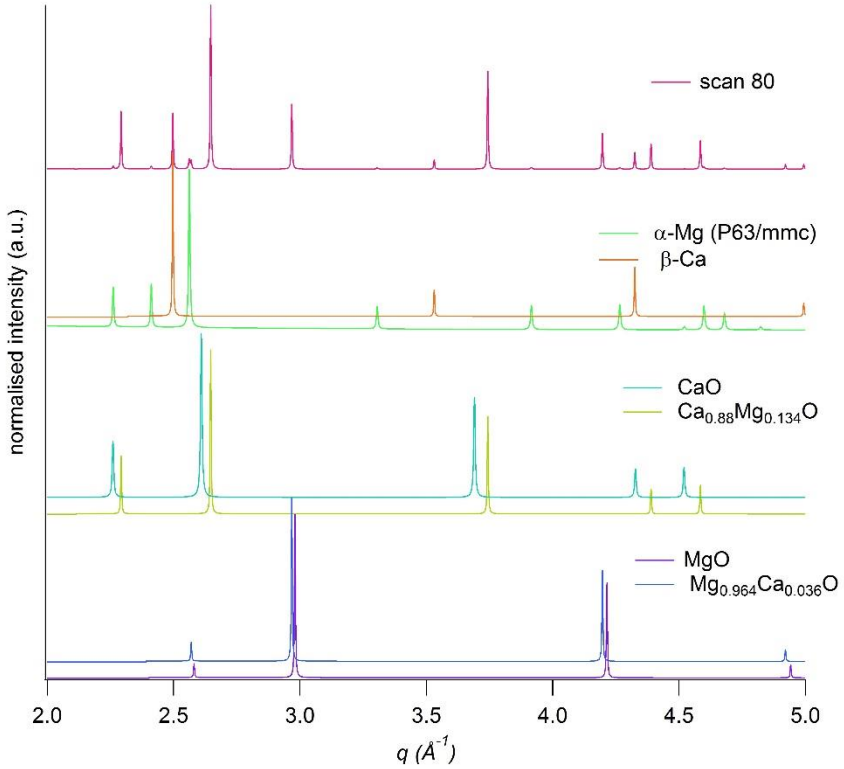

The evolution of the hydrogen weight percent (insert Figure 6-7-a) shown on the TPD measurement is comparable to the evolution of the main peak of CaO[*****] at 2.58 $Å^{-1}$ during its formation (insert Figure 6-7-b). This reaction may correspond to the 0.5 wt % of hydrogen lost at a temperature lower than 600 °C, analysed on the TGA-MS measurement (Figure 6-2). This pattern of reaction may be due to the formation of the solid solutions $Ca_{0.88}Mg_{0.134}O$ and $Mg_{0.964}Ca_{0.036}O$.

Starting at ≈ 720 °C up to 850 °C, the formation of CaO is more pronounced (Figure 6-7 main figure). Above 850 °C, which is the temperature at which all the CaH_2 is consumed, the rate of formation of CaO is slower. The peak of CaO is increasing due to external oxidation caused by the capillary cracking. The result of the TPD measurement showed a total weight percent of hydrogen desorbed of 2.0, or the equivalent of 82% efficiency compared to the theoretical value.

[*****] The small offset is due to different starting pressures. *In-situ* synchrotron analysis was done under 2 bar initial pressure.

Figure 6-7: Evolution (8°C/min) of the main peak of CaO (q = 2.6 Å) for in situ synchrotron X-ray diffraction of CaH_2 + MgO under 2 bar. Insert: overlapping of the TPD measurement of CaH_2+MgO (heating ramp = 3 °C/min up to 700 °C. under initial static vacuum ($1e^{-3}$ bar)) and the evolution (8 °C/min) of the main peak of the CaO phase (q = 2.6 Å) by in situ X-ray diffraction under 2 bar from room temperature to 700 °C.

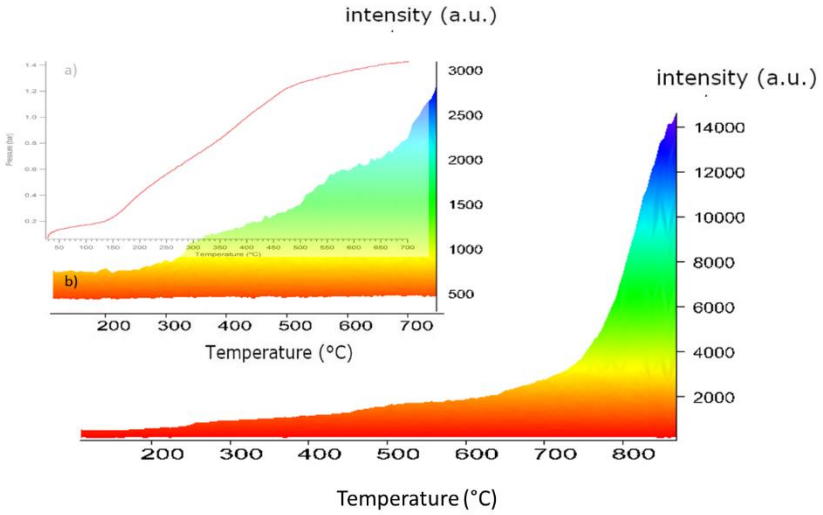

Technical details:

In order to perform the TPD measurement, The CaH_2 + MgO samples were packed in an iron tube (GoodFellow®, Outer diameter= 5 mm, wall thickness= 0.25 mm), pinched and then blended two times at both ends, as showed in Figure 6-8. As mentioned in the introduction of this section, a part of the Mg evaporates due to the low vapour pressure of the material at 700 °C.[4] The Mg gaseous and thus encloses inside the tube, while hydrogen can diffuse through the iron walls. The remaining empty volume of the sample cell reactor was filled with alumina rods It is rather common to observe Mg deposited on the surface of the alumina rod at the end of the experiment, as shown in Figure 6-9. As the handling of the iron tube is a painstaking job, the tube is easily punctured, partly due to the thinness of the walls.

Figure 6-8: Photograph of a CaH_2 + MgO packed in an iron tube.

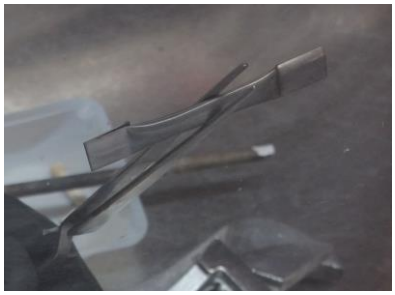

Figure 6-9: Photograph of Mg metal deposit on the alumina rod after TPD measurement.

Following the TPD measurement, 3 cycles of absorption and desorption were done in order to determine if these results were correct and whether TES was applicable (i.e. if the segregation of the Mg or its evaporating were insurmountable outcomes of the cycling phases within the system). The first step consists of a TPD measurement. The hydrogen release is calculated during the ramp rate. Then, at a stable temperature and as per each of the other steps, the reference volume is evacuated several times as soon as the pressure reaches the equilibrium pressure. The duration of the steps is different from one step to the other (some steps were done overnight- see Figure 6-10 a). The equilibrium pressure is observed for 700 °C around 0.4 bar. The hydrogen release reduces from 1.8 wt % to 1.44 wt % during the third desorption. The interesting observation about this cycle is that, as observed in Figure 6-10 b, this hydrogen sorption reaction can be considered to be at least partially reversible. To run the absorption, after each desorption, the pressure in the system has been set at a higher pressure than the equilibrium, thus leading to a pressure drop. Unfortunately, the absolute hydrogen weight percent calculated cannot be determined due to a leak in the system. However, it can be observed that each step can be broken down into two different parts. A first pressure drop due to the hydrogen absorption in the system and a second linear part. The latter part is characteristic of a gas leak. The leak rate is higher when the pressure is higher.

Figure 6-10: Cycling analysis for CaH_2 + MgO. a) 3 desorptions b) 3 absorptions. The top curve is the observation of pressure as function of time and the lower curve is the calculated hydrogen weight percent.

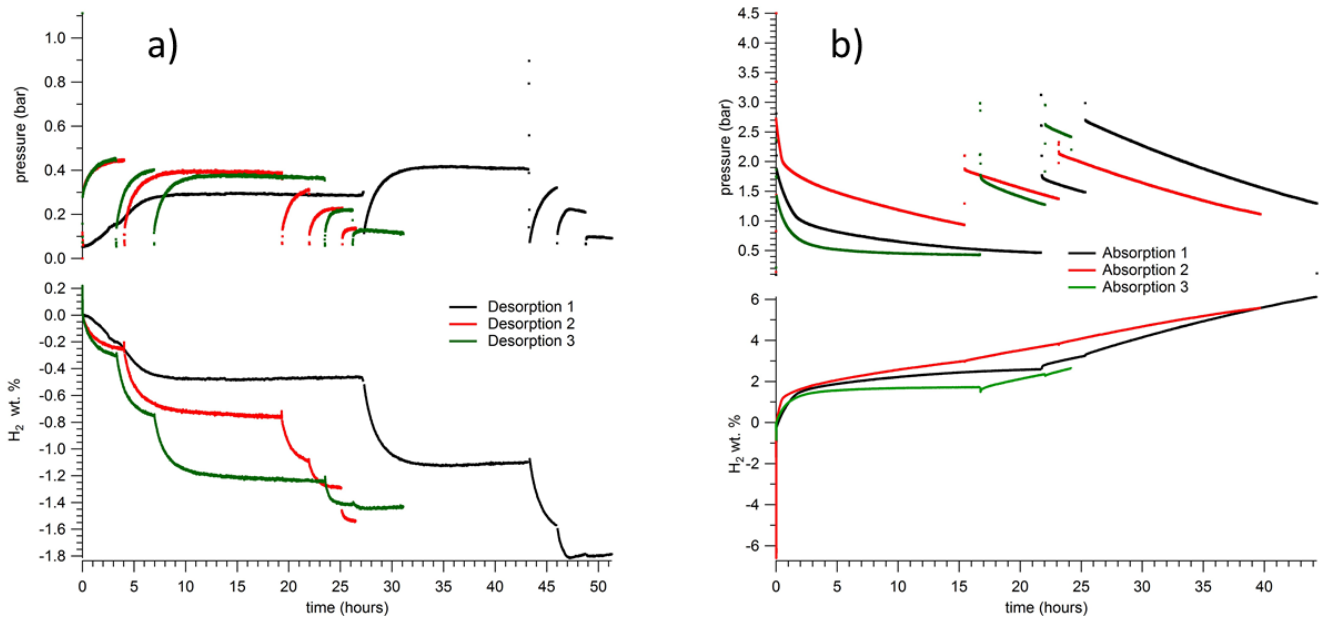

Figure 6-11 , shows the X-ray diffraction analysis after this cycling experiment. The powder in the iron tube and the powder on the iron tube walls were analysed. The sample had been cooled under dynamic vacuum, so it was in the desorbed state. The results showed that CaO, MgO, metallic Mg and traces of $CaMg_2$ compound were formed, however the highest concentration of metallic Mg was clearly found on the iron tube wall. These observations were not detected by *in-situ* synchrotron X-ray analysis. This might tell that they are slow kinetic process.

The X-ray analysis of the powder agglomerate found on the iron tube was conducted using an X-ray diffraction wizard using iron rich correction (grey line on Figure 6-11). [†††††] A concentration of Mg was observed which mean that the deposit on iron tube is due to Mg evaporation and deposit on the walls. It is representative of a segregation phenomenon.

[†††††] Indeed, iron causes fluorescence and bad counting statistics. The iron rich correction on the X-ray analysis helps to reduce this effect. Thus, the result has a lower statistic on the peaks intensity but by using this technique, the height of the Fe peaks dominating the other phases was avoided.

Figure 6-11: Comparative analysis of the normalised X-ray diffraction of the CaH_2 + MgO powder and the powder agglomerated on the iron tube after the cycling described in Figure 6-10.

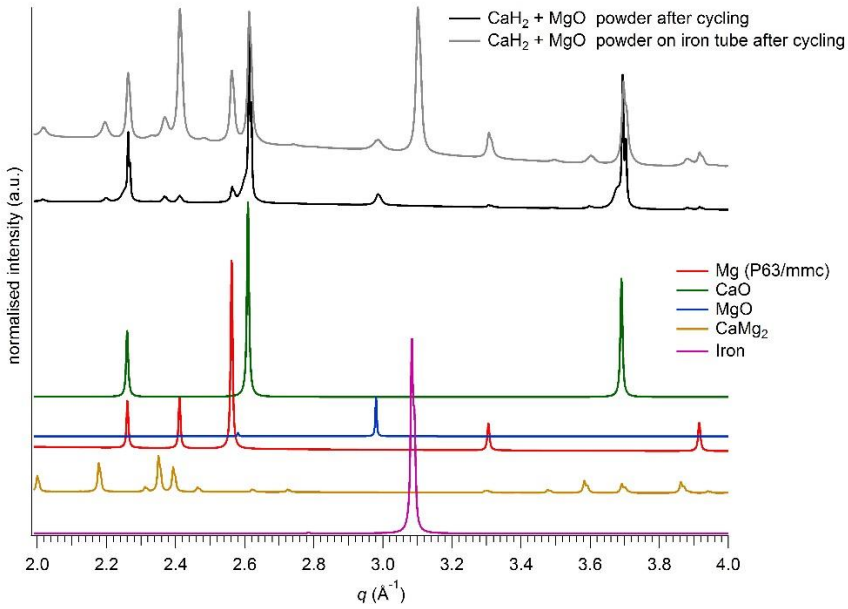

In order to construct the van't Hoff plot between 790 °C and 850 °C four PCI experiments were conducted in a silicon carbide reactor using an iron tube. Using the van't Hoff equation (eq.6-2), the enthalpy $\Delta H_{reaction}$ and the entropy $\Delta S_{reaction}$ of the reaction was calculated.

$$\text{van't Hoff eqation: } \ln\left(\frac{P_{H_2}}{1\ bar}\right) = -\frac{\Delta H_{reaction}(P,T)}{RT} + \frac{\Delta S_{reaction}(P,T)}{R} \qquad \text{Equation 6-2}$$

Figure 6-12: PCI's measurement of CaH_2 + MgO (step duration = 5 hours, pressure increment = 2 bar) between 790 °C and 850 °C. Ln (P) in bar versus calculated H_2 wt %,, and van't Hoff plot: ln (P) vs 1/T‡‡‡‡‡. using the mid-plateau (black markers) and using corrected for an infinite time mid-plateau step estimation (red markers).

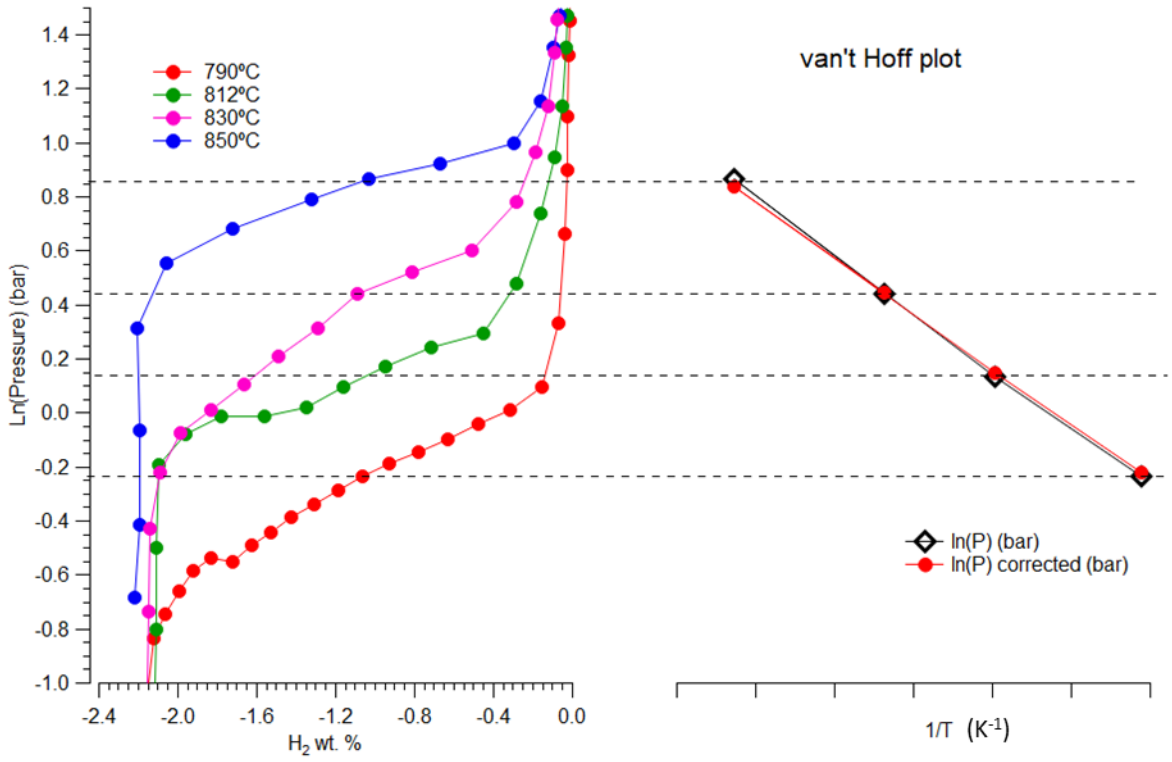

A deposit of magnesium metal was observed on the thermocouple as in the previous example, but at the same time, a consistent hydrogen weight percent of 2.17 ± 0.05 wt % was released. Using the mid-point of the plateau at 1 wt % to define the equilibrium pressure, the following can be calculated:

- $\Delta H_{reaction}$ = 177.4 ± 25 kJ·mol^{-1}·H_2
- $\Delta S_{reaction}$ = 165 ± 12 J·K^{-1}mol^{-1}·H_2

This value is overestimated because the equilibrium was not reached after 5 hours. This error becomes more important as the temperature of the measurement gets lower. Indeed, as the temperature is high the kinetics are improved. The pressure used for the van't Hoff plot has been estimated fitting

‡‡‡‡‡ A drop of temperature of 80 °C can be observed at the 830 °C temperature measuring point (pink curve). This drop explains the change in the ramp at the end of the plateau's end.

the kinetic curve at the mid-point of the plateau with a mathematical model to determine the final pressure at equilibrium (Figure 6-13) The corrected enthalpy and entropy using the corrected van't Hoff plot are the following, s (red markers on Figure 6-12):

- $\Delta H_{reaction}$ = 170.7 ± 25 kJ·mol^{-1} H_2
- $\Delta S_{reaction}$ = 158.4 ± 12 J.K^{-1}·mol^{-1} H_2
- R^2 = 0.9998

Figure 6-13: Mid-plateau step of PCI measurement on CaH_2 + MgO (red line) and asymptotic fit for an infinite time of this step (blue line) . Insert: Curve fitting command with equation.

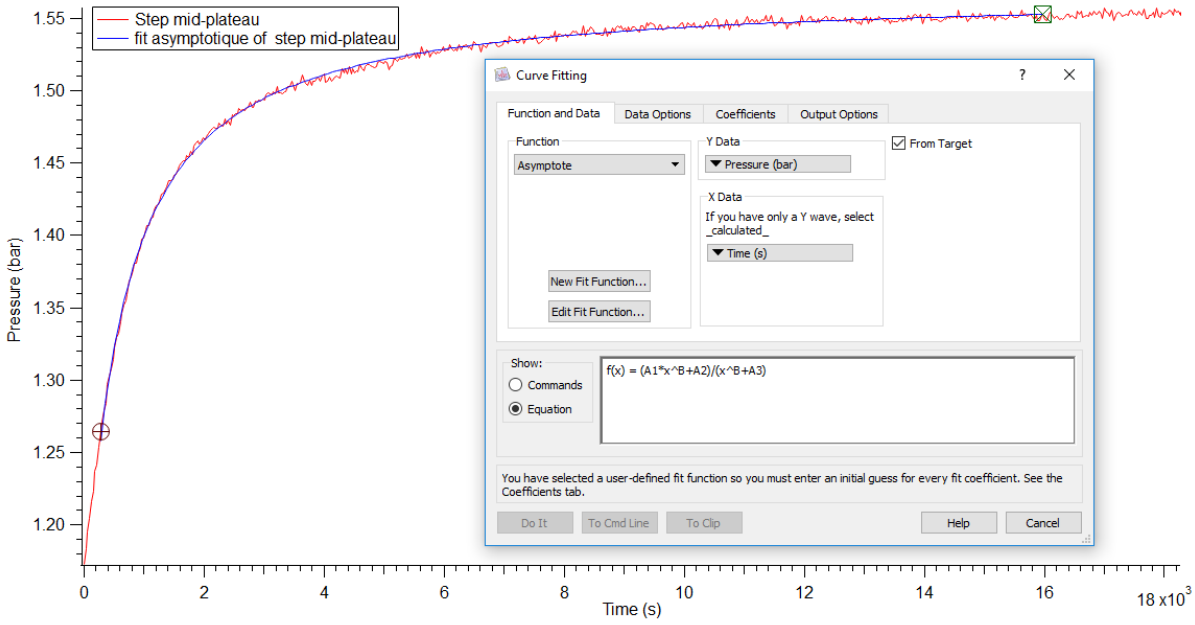

Note: A literature review has shown that the iron tube may react with the silicon carbide of the SCR[48-50]. Indeed, it is explained that a solid-state reaction occurs between SiC and iron at high temperature. Thus, the iron tube puncture must be due to the contact between the SiC and the iron. Due to the shape of the iron tube pinched and blended, the contact between the iron tube and the SiC reactor is a single point contact. In this case, the effect is considered to be negligible.

6.3. Conclusion and perspectives

This study confirms the potential of the CaH_2 + MgO system as a TES. Despite the Mg leakage from the iron tube and the segregation issues, it has been demonstrated that this system is possibly reversible. The observed loss of efficiency may be due to this phenomenon or the intermediate solid-state calcium magnesium oxide. For a potential application, it is necessary to develop a robust technique of compacting and confining the sample in the iron tube, in order to avoid segregation and leakage of Mg gas. A solution could be compacting the material into pellets as developed for magnesium hydrides-based materials.[97]. This solution would be useful to confine the material into the iron tube and be favorable for thermal conductivity.

Further investigations are necessary such as a cycling experiment, in order to define if the efficiency lost occurs at each cycle or if it is saturated at one point. A systematic kinetic study might also confirm if the iron tube wall thickness has any consequence on the hydrogen release rate. TPD analysis was conducted after polishing the iron tube's outer diameter to reduce the wall thickness to 0.15 mm and no noticeable increase in the kinetics was observed.

The calculations were done using the experimental H_2 wt % and $\Delta H_{reaction}$, resulted in a gravimetric heat storage capacity of 1910 $kJ \cdot kg^{-1}$ and a desorption temperature, T_{1bar} = 805 °C.

7. Conclusions and perspectives

This research program aimed to develop the knowledge base of energy storage materials, leading to a state-of-art renewable energy research portfolio. A screening tool for the selection of high temperature metal hydrides operating at the range required for the 2nd generation of TES for CST has been developed. As described in the introduction of this document, calcium hydride has a favourable energy density. Its abundance and the relatively low cost to synthesise calcium hydride makes it an interesting candidate for TES. Unfortunately, its operating temperature is too high and its corrosivity make it unsuitable for application. Thermodynamic destabilisation of metal hydrides involves adding a second element or compound to a metal hydride to change the reaction pathway associated with H_2 release. The objective of this study was to select which element or compound is required to add to calcium hydride in order to lower the temperature of H_2 release in the range recommended by the U.S. Department of Energy SunShot vision i.e. between 600 °C and 800 °C.

The first step was to select the most promising system using the thermodynamic calculations. First, an important phase of literature review has been done to find the most accurate values for the thermodynamic values i.e. the theoretical enthalpy, entropy and coefficients to calculate the evolution of the heat capacity depending on the temperature. Then, the path of reaction and the H_2 wt % released by each reaction assessed and an estimation of the economic viability of each system is predicted in order to select the candidates to synthetise. A mixture including calcium hydride powder with the required stoichiometry of the elements or compounds selected was weighed in a glovebox before being ball milled in a planetary ball milling machine for synthesise. The research for all the possible reactions of destabilised calcium hydrides is not comprehensive. Some possible reaction could be determined and discovered in the literature. Reactions such as the one between CaH_2 and Cl may be feasible in the required temperature range. This reaction, for example, has been studied by the HSRG and showed severe limitations due to very slow kinetics. The enthalpy and temperature of each potential reaction can be systematically predicted using the thermodynamic calculation screening tool.

As metal hydrides operating at high temperature is a recent field of research, the equipment for sorption analysis had to be adapted to these specifics working conditions. The analysis of the permeability and diffusion of SiC reactor and stainless-steel materials used for the Sample cell Reactor at high temperature is described in chapter 2.5.3. Also described are the specific parameters and/or procedures compulsory to experiment with hydrogen at high temperatures as well as the correction of the total amount of hydrogen released to avoid error due to diffusion and/or desorption by the SCR walls.

Thanks to international collaboration with several partner laboratories and beamtime for *in situ* X-ray analysis at the Australian Synchrotron, in depth study of the path of the selected system has been conducted. Figure 7-1 highlights the destabilisation of CaH_2 using the 3 different systems chosen. The $2CaH_2$ + Si system (blue lines on Figure 7-1) has been studied in Chapter 4 and although there are limitations, the CaSi-CaH_2 system is shown to be a promising candidate for TES application. Indeed, the high enthalpy of reaction, the low cost of both reactants, and the range of temperature show promising properties for TES application. The gravimetric heat storage capacity estimated based on experimental results and the cost of raw material permit to estimate a cost per electrical kWh stored in a range of 10 and 13 US$.kWh^{-1} for the high temperature metal hydride.

The Sunshot target aim a cost equal 15 US$/kW for the whole TES storage system including the cost of the low temperature hydrogen container and engineering costs. This constraint may limit the use of this system depending on the cyclability of the possible 2 steps of reaction. The cyclability study conducted by the Savannah's River National Laboratory reveals that only 1.2 wt % of hydrogen is desorbed and absorbed reversibly. The price of the paired system HTMH/LTMH using the model develop by Sheppard *et al*. using $NaAlH_4$ as the low temperature metal hydride (LTMH)[24] has been estimated between 16 and 18 US$.kWh^{-1}. This price is > 15 US$.kg^{-1} and engineering cost of the container and the heat transfer system are not included. This system is however is not ruled out. Indeed, a solution less expensive than $NaAlH_4$ may be used as the LTMH and the formation of solid solution observed at high pressure on the PCI measurement on the HTMH might add an extra hydrogen storage capacity to the overall coupled system (HTMH/LTMH) and an extra source of energy during the absorption time.

The system CaH_2 + 2C has been identified as a high gravimetric energy storage material during the theoretical analysis. This system needs further investigation to demonstrate its potential for TES applications. At this stage, it is not possible to confirm its cyclability. Solutions are proposed in the conclusion of chapter 5 such as using catalyst or reducing the gravimetric capacity of the initial material.

The experimental gravimetric heat storage capacity of the system CaH_2 + MgO revealed a storage capacity of 1910 $kJ.kg^{-1}$ (Chapter 6). The experiment results (PCI) show a desorption capacity higher than 80% of the theoretical H_2 wt % and an enthalpy of reaction higher than the predicted one. The cost per kWh stored has been estimated using the experimental results and turns out to be similar than the expected ones: ≈ 1.6 US$/kWh. This system is more than interesting for application. To be useable as TES, an engineering investigation may be required to confine the material in a Mg gas proof canister. The HSRG is working on upscaling experiments for high temperature metal hydrides using a 2 kg reactor. This equipment will be useful to analyse the heat transfer from the metal hydride to the Heat Transfer Fluid (HTF). An idea to consider with this system is to use excess Mg to compensate for the evaporation of Mg and to fill any empty space, and hence due to its high conductivity the Mg will be favourable for better heat conduction.

In parallel, the study of the kinetics of the different materials analysed is required and cycling the material to determine its viability for an industrial application is essential. The actual results are in process of publication.

Figure 7-1: Comparison of CaH_2 with CaH_2 + MgO, CaH_2+2C, 2CaH_2 + Si. TGA -MS curve.

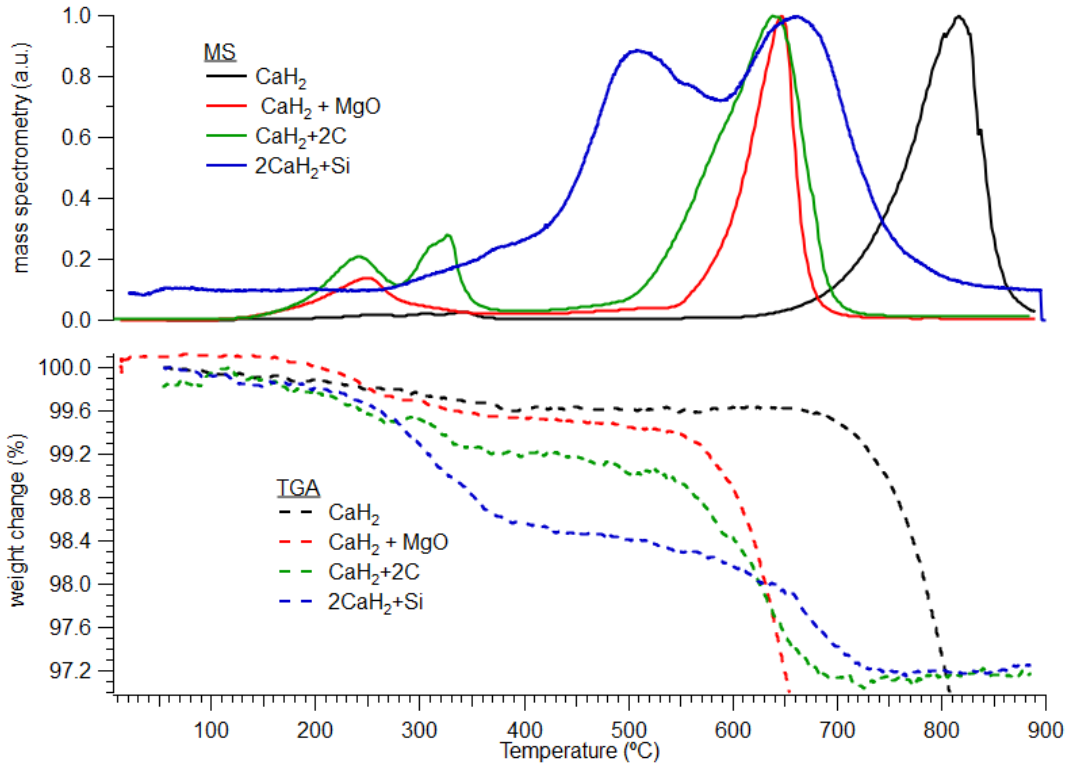

This thesis investigated high temperature metal hydrides operating in the temperature range between 600 °C and 800 °C. Metal hydrides for thermal energy storage are a promising solution for the development of concentrating solar power as a renewable energy source. Destabilised calcium hydrides (especially MgO destabilised CaH_2) have the potential to be competitive concentrating solar thermal energy stores.

Appendices

Figure A- 1: The Ca-Zn phase diagram.[62]

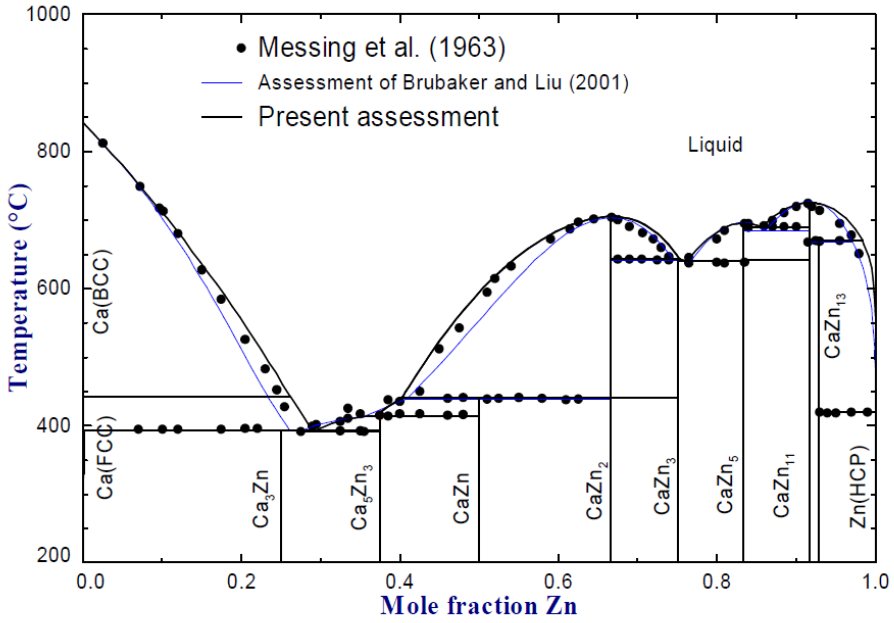

Figure A- 2: Equilibrium composition of CaH_2 + Zn from 0 to 1500 °C.

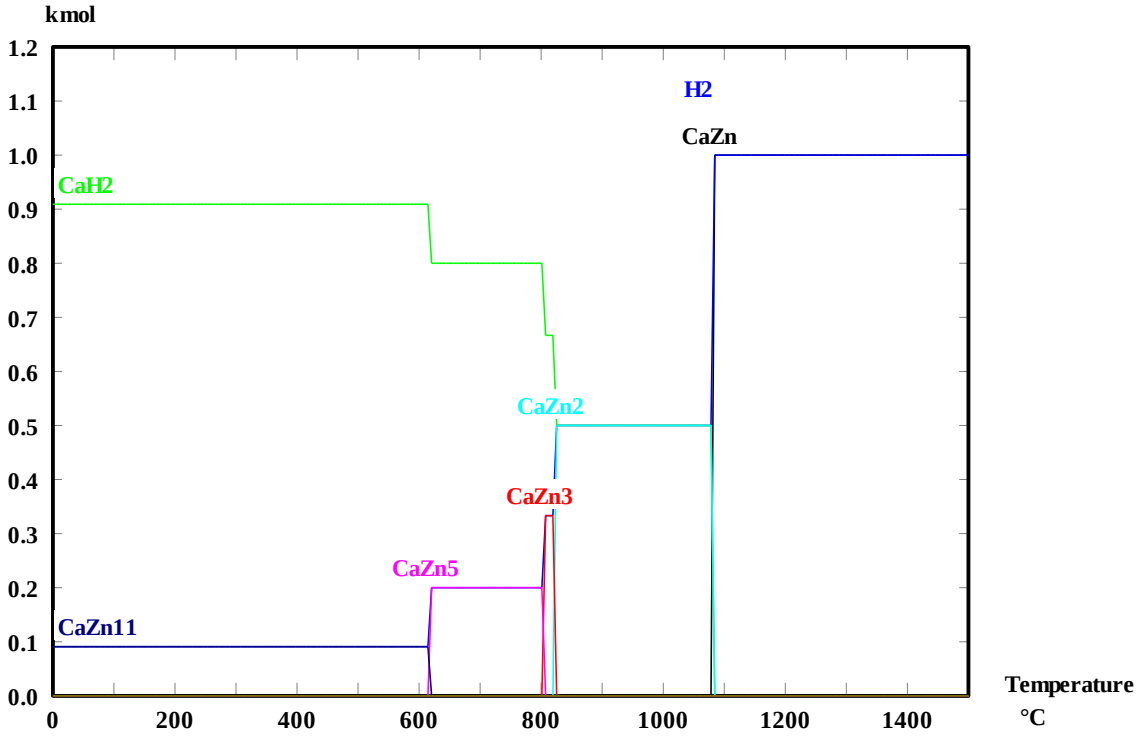

Figure A- 3: Phase diagram Ca-Sn.[98]

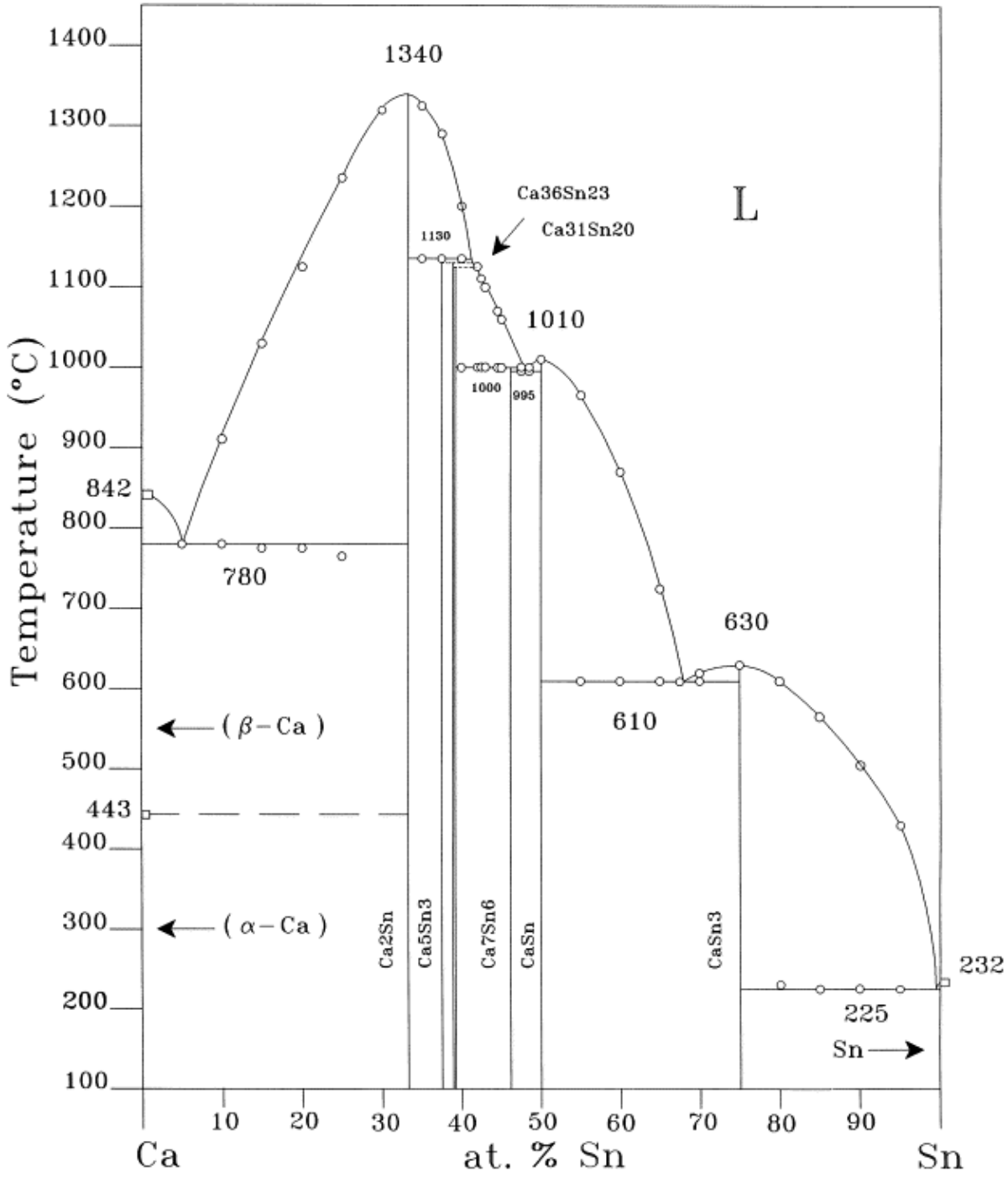

Figure A- 4: Temperature of reaction and enthalpy per mole of hydrogen of every possible reaction for the CaH_2-Sn system.

	Possible reactions between CaH_2 &:	$T_{(1Bar)}$ ^0C	ΔH (kJ·mol^{-1} H_2)	H_2 wt %
	Sn			
1	$2CaH_2 + Sn \rightleftarrows Ca_2Sn + 2H_2$	117	36.4	1.99%
2	$5CaH_2 + 3Sn \rightleftarrows Ca_5Sn_3 + 5H_2$	87	35.2	1.78%
3	$36CaH_2 + 23Sn \rightleftarrows Ca_{36}Sn_{23} + 36H_2$	77	34.7	1.97%
4	$31CaH_2 + 20Sn \rightleftarrows Ca_{31}Sn_{20} + 31H_2$	77	34.6	1.47%
5	$7CaH_2 + 6Sn \rightleftarrows Ca_7Sn_6 + 7H_2$	37	32.1	1.40%
6	$CaH_2 + Sn \rightleftarrows CaSn + H_2$	10	29.8	1.25%
7	$CaH_2 + 3Sn \rightleftarrows CaSn_3 + H_2$	-1534	-154.8	0.51%
	$CaSn_3$			
8	$5CaH_2 + CaSn_3 \rightleftarrows 3Ca_2Sn + 5H_2$	177	39.7	1.66%
9	$4CaH_2 + CaSn_3 \rightleftarrows Ca_5Sn_3 + 4H_2$	157	39.1	1.43%
10	$28.3.CaH_2 + 7.67CaSn_3 \rightleftarrows= Ca_{36}Sn_{23} + 28.33H_2$	147	38.8	1.35%
11	$24.33CaH_2 + 6.67CaSn_3 \rightleftarrows Ca_{31}Sn_{20} + 24.33H_2$	147	38.8	1.34%
12	$5CaH_2 + 2CaSn_3 \rightleftarrows Ca_7Sn_6 + 5H_2$	107	37.1	1.01%
13	**$2CaH_2 + CaSn_3 \rightleftarrows 3CaSn + 2H_2$**	**77**	**35.8**	**0.84%**
	CaSn			
14	$CaH_2 + CaSn \rightleftarrows Ca_2Sn + H_2$	267	42.4	1.00%
15	$2CaH_2 + 3CaSn \rightleftarrows Ca5Sn_3 + 2H_2$	247	42.4	0.72%
16	$13CaH_2 + 23CaSn \rightleftarrows Ca_{36}Sn_{23} + 13H_2$	247	42.4	0.62%
17	$11CaH_2 + 20CaSn \rightleftarrows Ca_{31}Sn_{20} + 11H_2$	247	42.4	0.61%
18	$CaH_2 + 6CaSn \rightleftarrows Ca_7Sn_6 + H_2$	247	42.4	0.20%
	Ca_5Sn_3			
19	$CaH_2 + Ca_5Sn_3 \rightleftarrows 3Ca_2Sn + H_2$	297	42.4	0.34%
	Ca_7Sn_6			
20	$5CaH_2 + Ca_7Sn_6 = 6Ca_2Sn + 5H_2$	267	42.4	0.84%
21	$3CaH_2 + Ca_7Sn_6 \rightleftarrows 2Ca_5Sn_3 + 3H_2$	257	42.4	0.54%
22	$55CaH_2 + 23Ca_7Sn_6 \rightleftarrows 6Ca_{36}Sn_{23} + 55H_2$	247	42.4	0.44%
23	$23CaH_2 + 10Ca_7Sn_6 \rightleftarrows 3Ca_{31}Sn_{20} + 23H_2$	247	42.4	0.43%
	$Ca_{36}Sn_{23}$			
24	$10CaH_2 + Ca_{36}Sn_{23} \rightleftarrows 23Ca_2Sn + 10H_2$	297	42.4	0.44%
25	$7CaH_2 + 3Ca_{36}Sn_{23} \rightleftarrows 23Ca_5Sn_3 + 7H_2$	297	42.4	0.11%
	$Ca_{31}Sn_{20}$			
26	$9CaH_2 + Ca_{31}Sn_{20} \rightleftarrows 20Ca_2Sn + 9H_2$	297	42.4	0.45%
27	$7CaH_2 + 3Ca_{31}Sn_{20} \rightleftarrows 20Ca_5Sn_3 + 7H_2$	287	42.4	0.13%
28	$7CaH_2 + 23Ca_{31}Sn_{20} = 20Ca_{36}Sn_{23} + 7H_2$	287	42.4	0.02%

Figure A- 5: The Ca-Pb phase diagram.[64]

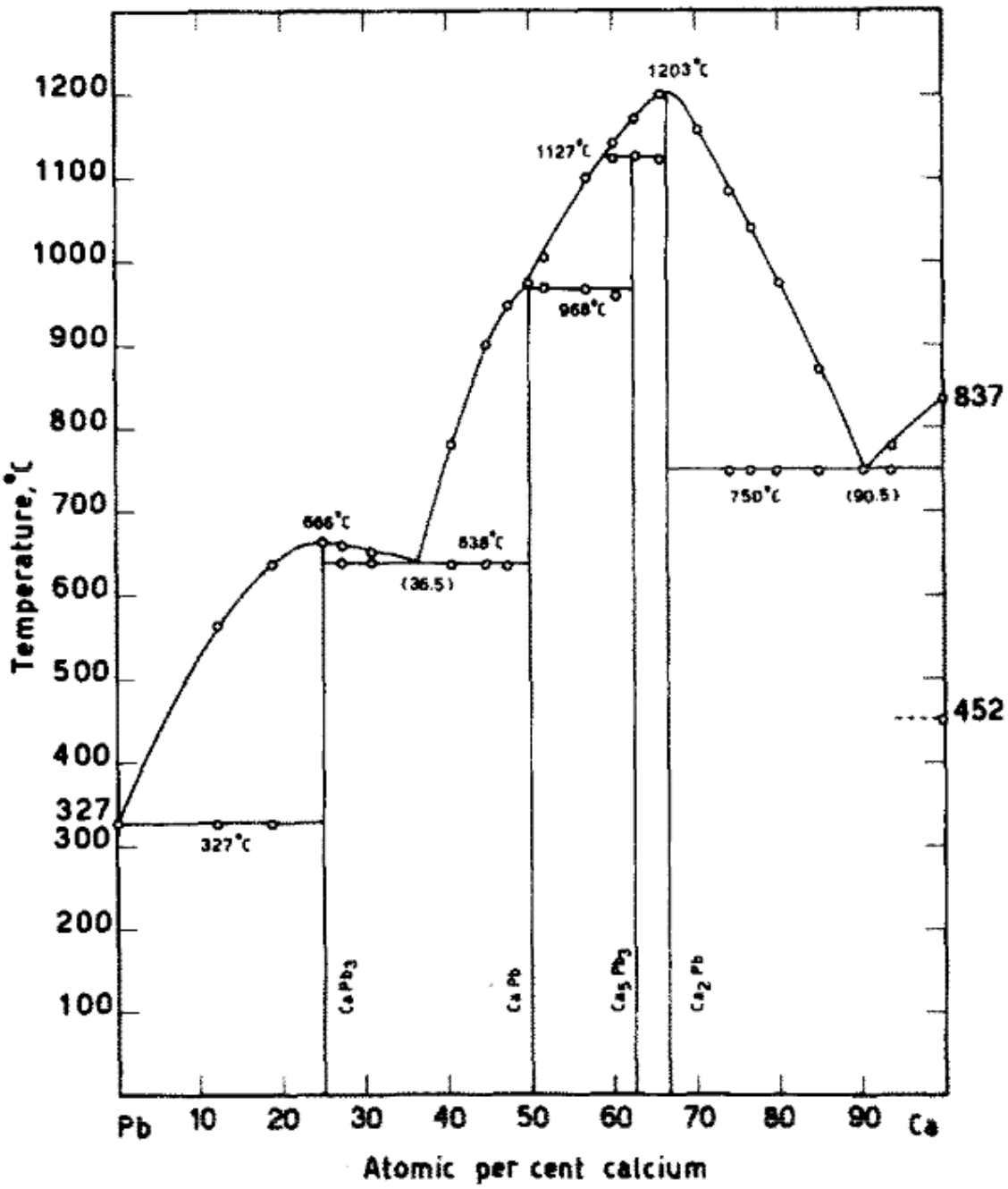

Figure A- 6: Temperature of reaction and enthalpy per mole of hydrogen of every possible reaction for the CaH_2 -Pb system.

	Possible reactions between CaH_2 & :	$T_{(1Bar)}$ °C	ΔH ($kJ \cdot mol^{-1}$ H_2)	H_2 wt %
	Pb			
1	$2CaH_2 + Pb \rightleftarrows Ca_2Pb + 2H_2$	427	83.6	1.38%
2	$5CaH_2 + 3Pb \rightleftarrows Ca_5Pb_3 + 5H_2$	457	82.7	1.21%
3	$CaH_2 + Pb \rightleftarrows CaPb + H_2$	287	82.7	0.81%
4	$CaH_2 + 3Pb \rightleftarrows CaPb_3 + H_2$	237	46.9	0.30%
	$CaPb_3$			
5	$2CaH_2 + CaPb_3 \rightleftarrows 3CaPb + 2H_2$	307	74.5	0.54%
6	$4CaH_2 + CaPb_3 \rightleftarrows Ca_5Pb_3 + 4H_2$	507	91.7	0.97%
7	$5CaH_2 + CaPb_3 \rightleftarrows 3Ca_2Pb + 5H_2$	457	90.9	1.16%
	CaPb			
8	$CaH_2 + CaPb \rightleftarrows Ca_2Pb + H_2$	557	101.7	0.70%
9	$2CaH_2 + 3CaPb \rightleftarrows Ca_5Pb_3 + 2H_2$	757	108.8	0.49%
	Ca_5Pb_3			
10	$CaH_2 + Ca_5Pb_3 \rightleftarrows 3Ca_2Pb + H_2$	287	88.6	0.23%

Figure A- 7: The Ca-Ag phase diagram.[99]

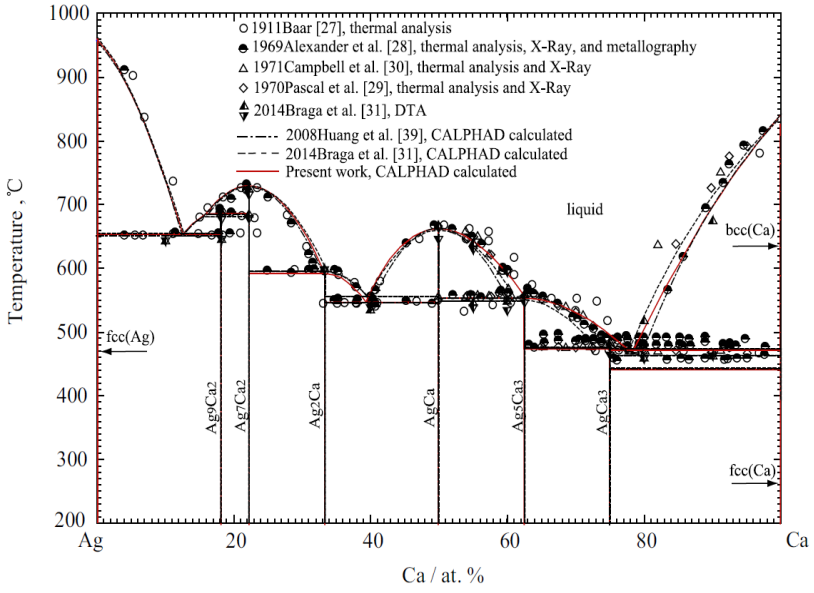

Figure A- 8: Temperature of reaction and enthalpy per mole of hydrogen of every possible reaction for the CaH_2 -Ag system.

		$T_{(1Bar)}$ ^0C	$n(H_2)$ released	H ($kJmol^{-1}$ H_2)	$KJ.Kg^{-1}$ at T(RXN)	H_2 wt %
	Ag					
1	$2CaH_2 + 9Ag \rightleftarrows Ca_2Ag_9 + 2H_2$	397	2	85.2	161	0.38
2	$2CaH_2 + 7Ag \rightleftarrows Ca_2Ag_7 + 2H_2$	407	2	84.3	201	0.48
3	$CaH_2 + 2Ag \rightleftarrows CaAg_2 + H_2$	557	1	105.1	407	0.78
4	$CaH_2 + Ag \rightleftarrows CaAg + H_2$	707	1	123.5	823	1.34
5	$5CaH_2 + 3Ag \rightleftarrows Ca_5Ag_3 + 5H_2$	867	5	135.9	1272	1.89
6	$3CaH_2 + Ag \rightleftarrows Ca_3Ag + 3H_2$	967	3	146.5	1877	2.58
	Ca_2Ag_9					
7	$4CaH_2 + 7Ca_2Ag_9 \rightleftarrows 9Ca_2Ag_7 + 4H_2$	437	4	115.3	61	0.11
8	$5CaH_2 + 2Ca_2Ag_9 \rightleftarrows 9CaAg_2 + 5H_2$	687	5	120.9	261	0.44
9	$7CaH_2 + Ca_2Ag_9 \rightleftarrows 9CaAg + 7H_2$	797	7	134.5	699	1.05
10	$13CaH_2 + Ca_2Ag_9 \rightleftarrows 3Ca_5Ag_3 + 13H_2$	947	13	136.9	1113	1.64
11	$25CaH_2 + Ca_2Ag9 \rightleftarrows 9Ca_3Ag + 25H_2$	1037	25	151.9	1805	2.40
	Ca_2Ag_7					
12	$3CaH_2 + 2Ca_2Ag_7 \rightleftarrows 7CaAg_2 + 3H_2$	757	3	132.6	221	0.34
13	$5CaH_2 + Ca_2Ag_7 \rightleftarrows 7CaAg + 5H_2$	827	5	139.2	665	0.96
14	$29CaH_2 + 3Ca_2Ag_7 \rightleftarrows 7Ca5Ag3 + 29H_2$	977	29	139.2	1083	1.57
15	$19CaH_2 + Ca_2Ag_7 \rightleftarrows 7Ca3Ag + 19H_2$	1047	9	153.7	1139	1.49
	$CaAg_2$					
16	$CaH_2 + CaAg_2 \rightleftarrows 2CaAg + H_2$	857	1	142.6	478	0.67
17	$7CaH_2 + 3CaAg_2 \rightleftarrows 2Ca_5Ag_3 + 7H_2$	1017	7	141.4	932	1.33
18	$5CaH_2 + CaAg_2 \rightleftarrows 2Ca_3Ag + 5H_2$	1077	5	156.1	1673	2.16
	CaAg					
19	$2CaH_2 + 3CaAg \rightleftarrows Ca_5Ag_3 + 2H_2$	1147	2	146.9	556.6	0.76
20	$2CaH_2 + CaAg \rightleftarrows Ca_3Ag + 2H_2$	1127	2	161.1	1388.0	1.74
	Ca_5Ag_3					
21	$4CaH_2 + Ca_5Ag_3 \rightleftarrows 3Ca_3Ag + 4H_2$	1127	4	168.2	971.7	1.16

Figure A- 9: Equilibrium composition of $3CaH_2$ + Ag from 0 °C to 1000 °C.

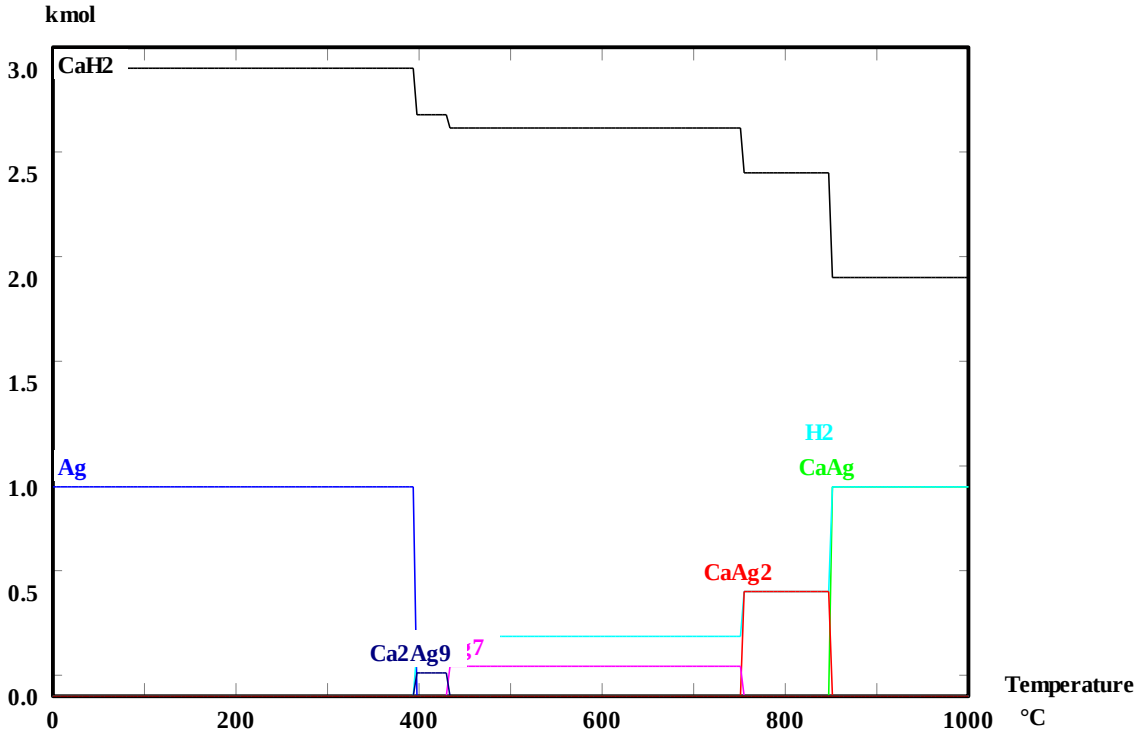

Figure A- 10: Equilibrium composition of CaH_2 + 6B from 0 °C to 500 °C.

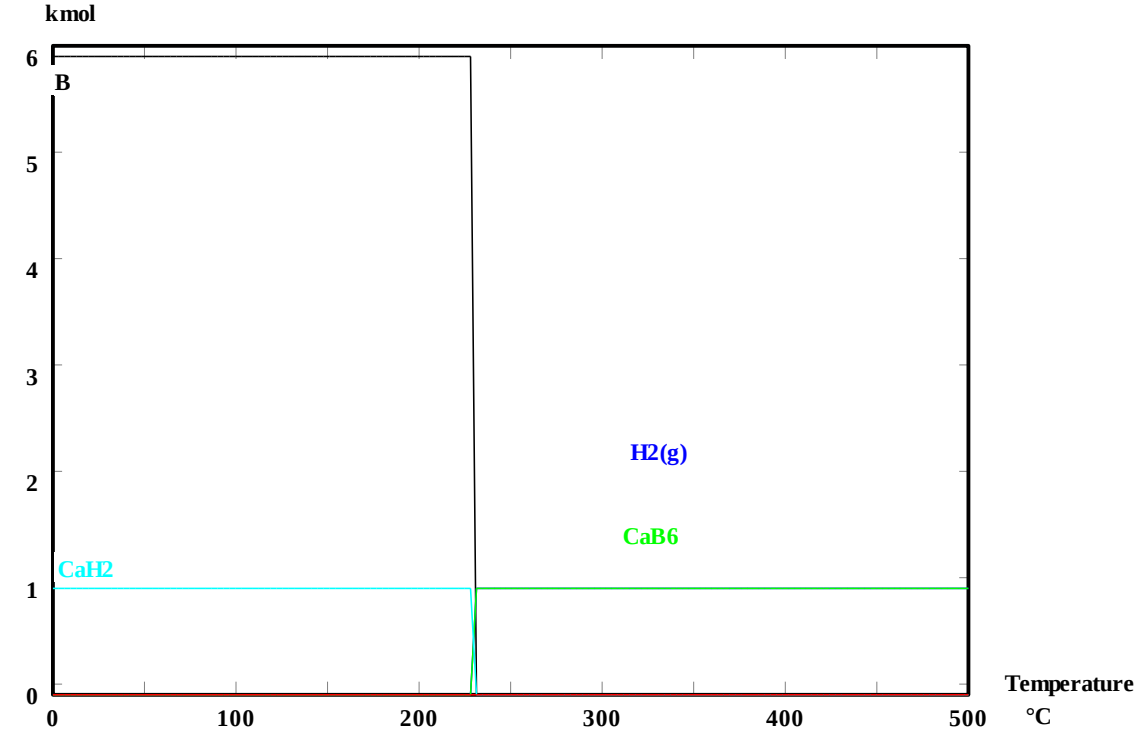

Figure A- 11: The Ca-B phase diagram.[100]

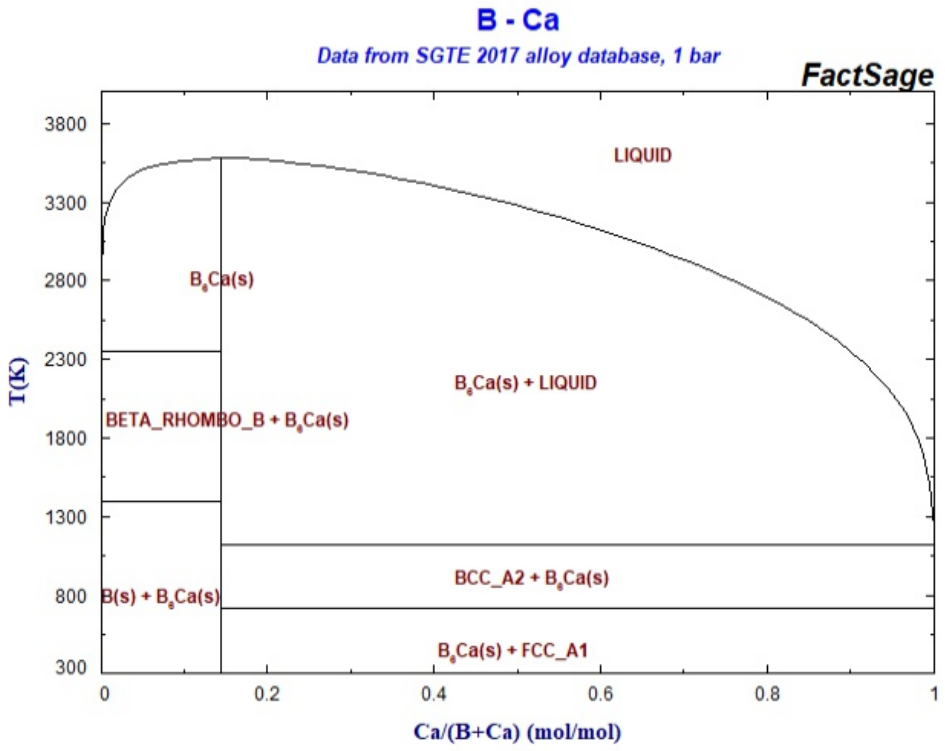

Figure A- 12: Equilibrium composition of $2CaH_2$ + Si.

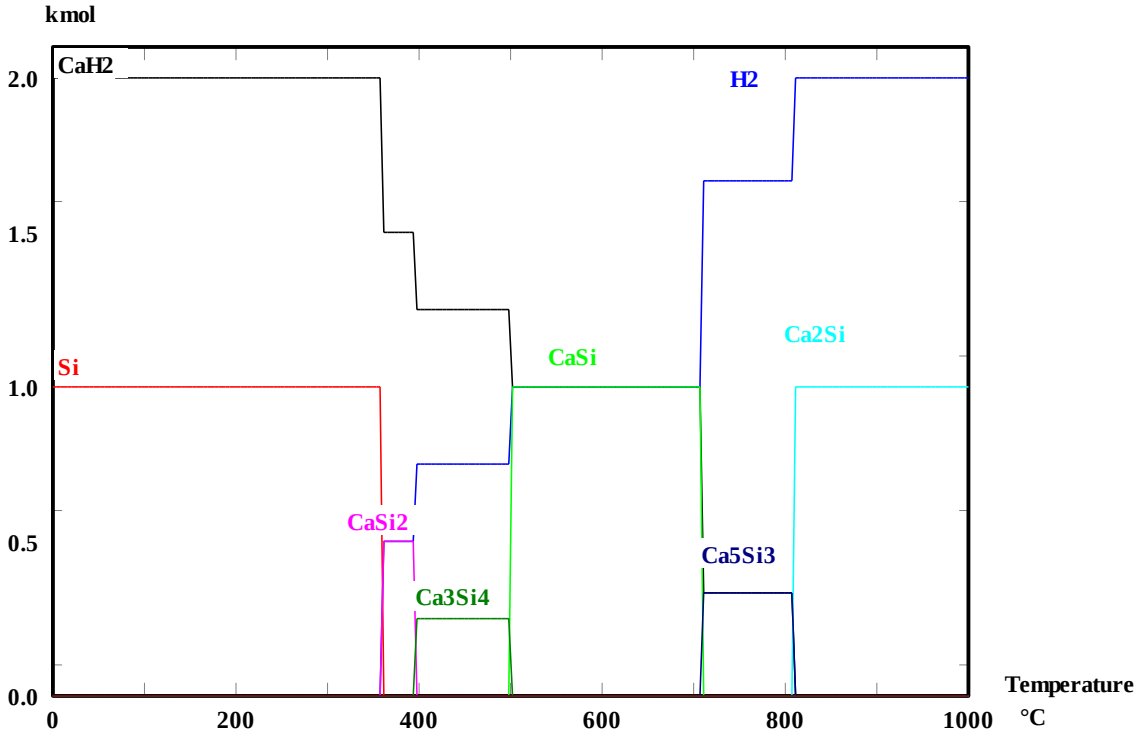

Figure A- 13: The C-Ca phase diagram.[100]

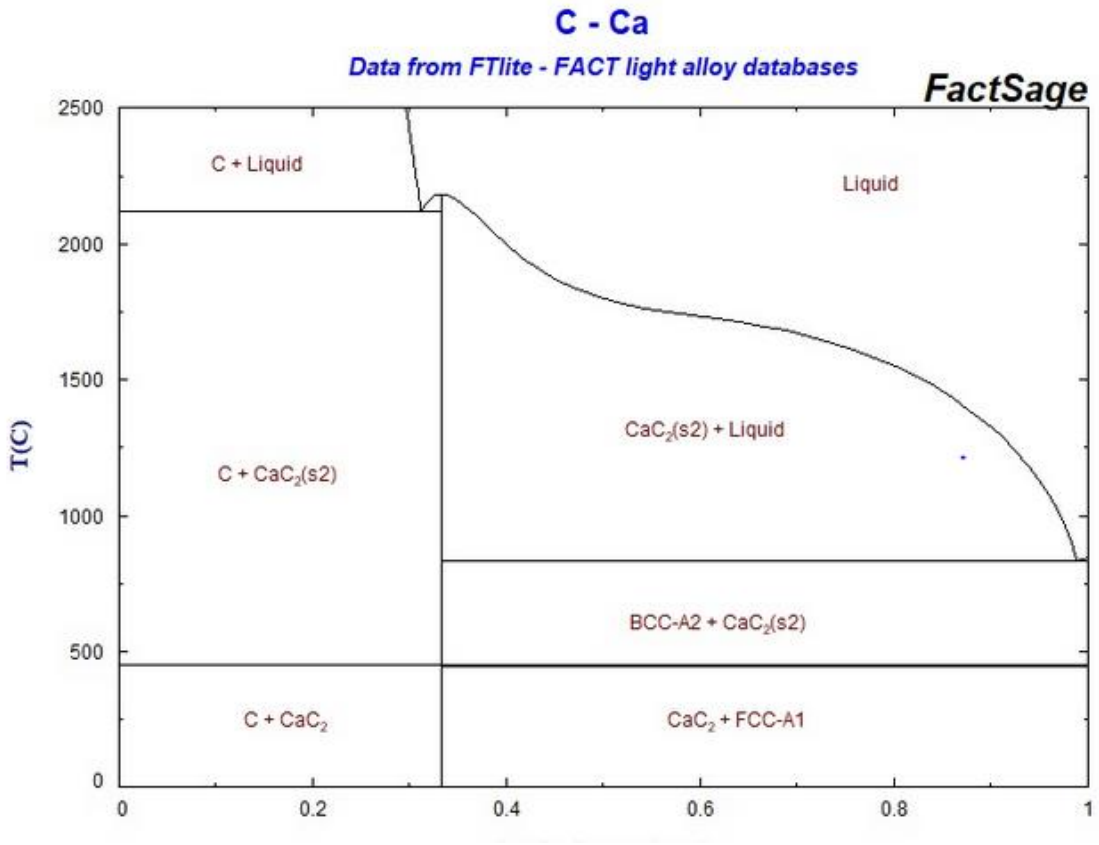

Figure A- 14: Equilibrium composition of CaH_2 + 2C.

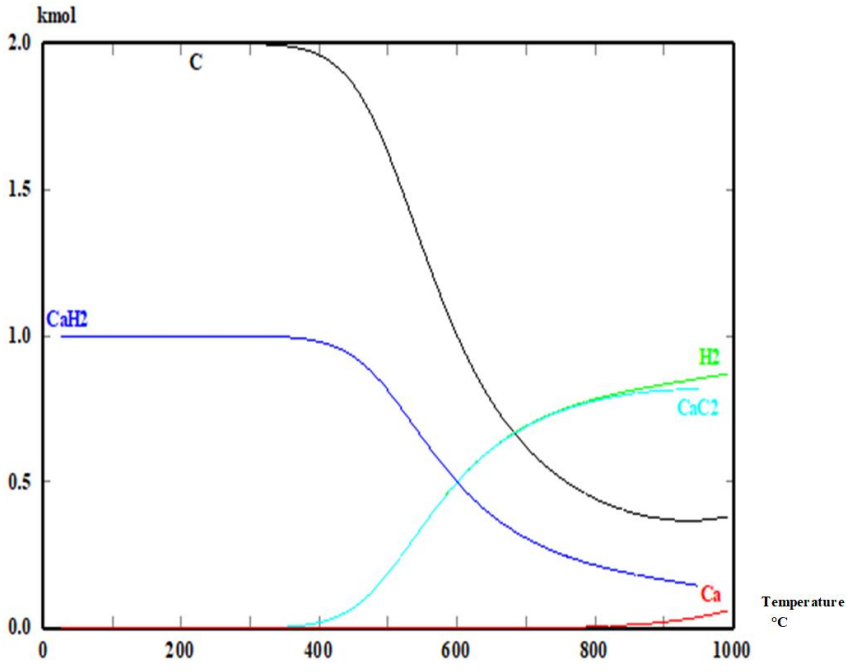

Figure A-15: The CaO-MgO phase diagram.[101]

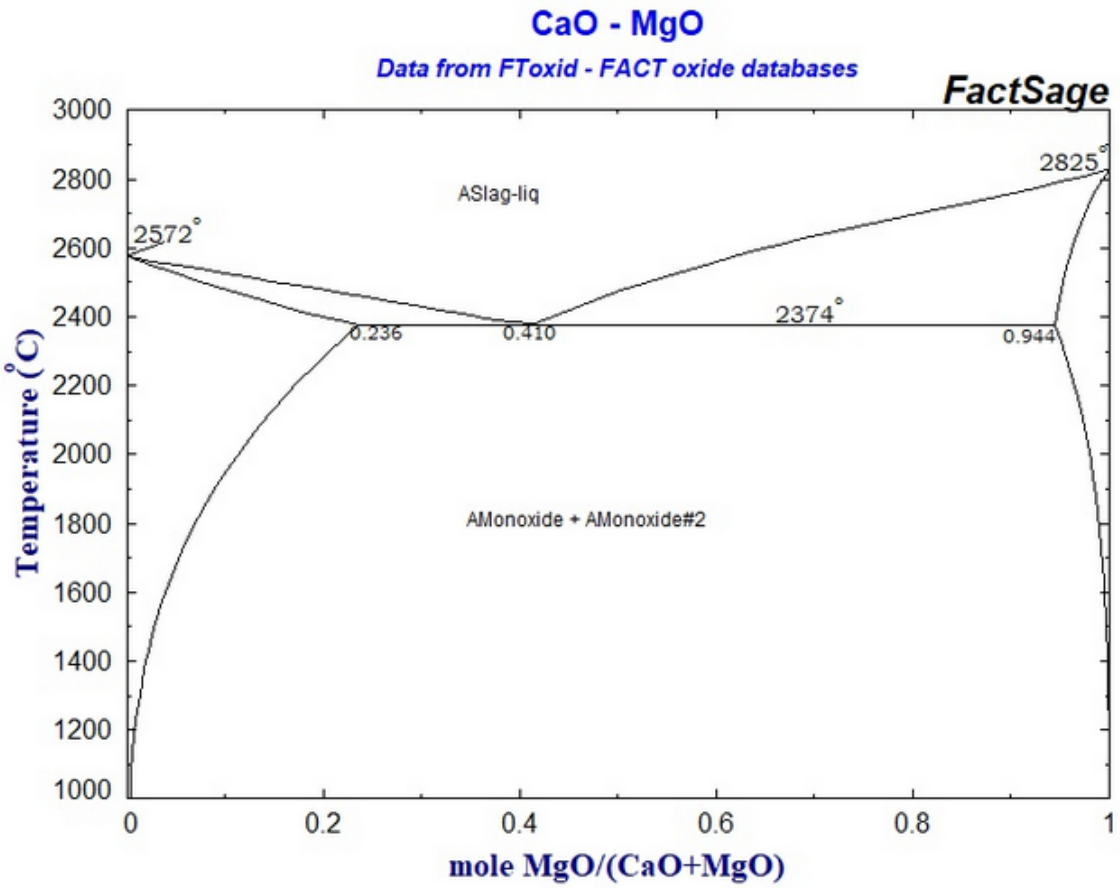

Figure A- 16: PCI at 520 °C on CaH_2 + Si.

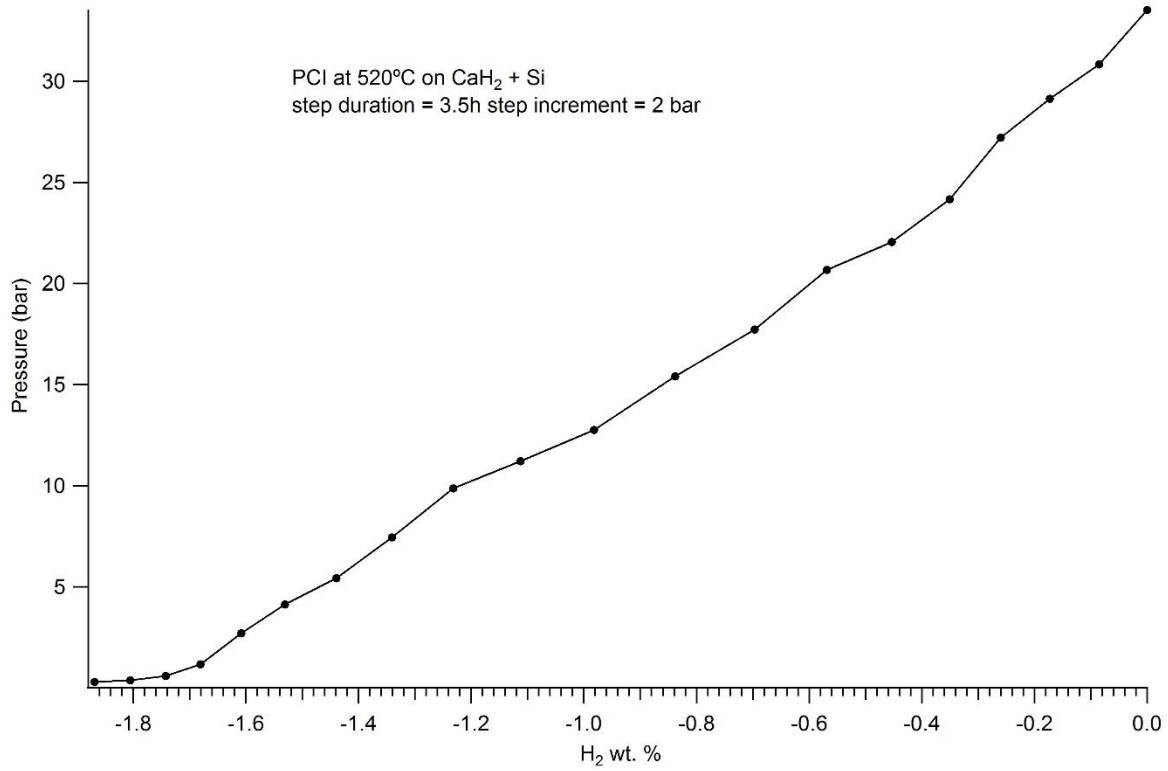

References

1. D. Abbot, *Proceeding of the IEEE* 2010, **98**, 41-66.
2. U. S. D. o. Energy, *SunShot Vision Study*, 2012.
3. J. J. Vajo and G. L. Olson, *Scripta Materialia*, 2007, **56**, 829-834.
4. W. P. Gilbreath, *NASA TECHNICAL NOTE* 1965.
5. I. E. Agency, https://www.iea.org.
6. A. Zuttel, *Naturwissenschaften*, 2004, **91**, 157-172.
7. W. A. Hermann, *Energy*, 2006, **31**, 1685-1702.
8. https://www.irena.org, https://www.irena.org/DocumentDownloads/Publications/Perspectives_for_the_Energy_Transition_2017.pdf.
9. S. Rühle, *Solar Energy*, 2016, **130**, 139-147.
10. *Global Energy & CO2 Status report 2017*, iea, 2017.
11. J. P. Deane, B. P. Ó Gallachóir and E. J. McKeogh, *Renewable and Sustainable Energy Reviews*, 2010, **14**, 1293-1302.
12. M. Skyllas-Kazacos, M. Chakrabarti, S. Hajimolana, F. Mjalli and M. Saleem, *Journal of The Electrochemical Society*, 2011, **158**, R55-R79.
13. I. Dincer, *Thermal energy storage systems and applications,* , John Wiley & Sons Ltd, 2010.
14. S. Kaneff, *Journal De Physique Iv*, 1999, **9**, 195-200.
15. B. Kongtragool and S. Wongwises, *Renewable & Sustainable Energy Reviews*, 2003, **7**, 131-154.
16. L. C. Spencer, *Solar Energy*, 1989, **43**, 191-196.
17. J. L. Sawin, F. Sverrisson, W. Rickerson, C. Lins, L. E. Williamson, R. Adib, H. E. Murdock, E. Musolino, M. Hullin and A. Reith, *Journal*, 2015.
18. W. E. Wentworth and E. Chen, *Solar Energy*, 1976, **18**, 205-214.
19. A. M. Khudhair and M. M. Farid, *Energ Convers Manage*, 2004, **45**, 263-275.
20. M. Paskevicius, D. A. Sheppard, K. Williamson and C. E. Buckley, *Energy*, 2015, **88**, 469-477.
21. D. N. Harris, M. Paskevicius, D. A. Sheppard, T. E. C. Price and C. E. Buckley, *Proceedings of the IEEE*, 2012, **100**, 539-549.
22. Melissae Fellet, C. E. Buckley, M. Paskevicius and D. A. Sheppard, *MRS BULLETIN*, 2013, **38**.
23. C. Corgnale, B. Hardy, T. Motyka, R. Zidan, J. Teprovich and B. Peters, *Renewable and Sustainable Energy Reviews*, 2014, **38**, 821-833.
24. D. A. Sheppard, C. Corgnale, B. Hardy, T. Motyka, R. Zidan, M. Paskevicius and C. E. Buckley, *RSC Adv.*, 2014, **4**, 26552-26562.
25. M. S. Tortoza, T. D. Humphries, D. A. Sheppard, M. Paskevicius, M. R. Rowles, M. V. Sofianos, K.-F. Aguey-Zinsou and C. E. Buckley, *Physical Chemistry Chemical Physics*, 2018, DOI: 10.1039/C7CP07433F.
26. http://www.metalprices.com, 2013.
27. A. Andreasen, *Predicting formation enthalpies of metal hydrides*, 2004.
28. Remy-Gennete, *Ann. chim.*, 1933, **19**.
29. D. T. Peterson and V. G. Fattore, *The Journal of Physical Chemistry*, 1961, **65**, 2062-2064.
30. M. Wang, W. H. Sun, C. S. Sha, B. Hu, Y. Du, L. X. Sun, H. H. Xu, J. C. Wang and S. H. Liu, *Journal of Phase Equilibria and Diffusion*, 2012, **33**, 89-96.
31. R. Curtis and P. Chiotti, *The Journal of Physical Chemistry*, 1963, **67**, 1061-1065.
32. E. Veleckis, *Journal of the Less Common Metals*, 1980, **73**, 49-60.
33. V. V. Louis and H. H. Franck, *Zeitsohrift fiir anorganische und allgemeine Chemie*, 1939, **242**, 117-127.
34. P. Chiotti, R. W. Curtis and P. F. Woerner, *Journal of the Less Common Metals*, 1964, **7**, 120-126.
35. *United States of America Pat.,* 2,082,134, 1935.

36. *United States of America Pat.,* 2,656,268, 1950.
37. S. Reich and H. Serpek, *Helvetica Chimica Acta*, 1920, **3**, 138-144.
38. J. A. Murshidi, M. Paskevicius, D. Sheppard and C. E. Buckley, *Structure, morphology and hydrogen storage properties of a Ti0.97Zr0.019V0.439Fe0.097Cr0.045Al0.026Mn1.5 alloy*, 2011.
39. A. Bulanov, O. Y. Troshin and V. Balabanov, *Russian journal of applied chemistry*, 2004, **77**, 875-877.
40. L. V. Azaroff and M. J. Buerger, *McGrow-Hill Book Company, New York*, 1958.
41. J. D. Dunitz, *X-ray Analysis and the Structure of Organic Molecules*, Verlag Helvetica Chimica Acta Basel, 1995.
42. H. Rietveld, *Journal of Applied Crystallography*, 1969, **2**, 65-71.
43. T. P. Blach and E. M. Gray, *Journal of Alloys and Compounds*, 2007, **446-447**, 692-697.
44. C. S. Marchi, B. P. Somerday and S. L. Robinson, *International Journal of Hydrogen Energy*, 2007, **32**, 100-116.
45. A. Causey R, D. Fowler J, C. Ravanbakht, S. Elleman T and K. Verghese, *Journal of the American Ceramic Society*, 1978, **61**, 221-225.
46. K. S. Forcey, D. K. Ross and C. H. Wu, *Journal of Nuclear Materials*, 1991, **182**, 36-51.
47. R. A. Causey, R. A. Karnesky and C. San Marchi, 2012.
48. M. Backhaus-Ricoult, *Acta metallurgica et materialia*, 1992, **40**, S95-S103.
49. R. Schiepers, J. Van Beek, F. Van Loo and G. De With, *Journal of the European Ceramic Society*, 1993, **11**, 211-218.
50. W. Tang, Z. Zheng, H. Ding and Z. Jin, *Materials chemistry and physics*, 2002, **74**, 258-264.
51. A. T. Dinsdale, *Calphad-Computer Coupling of Phase Diagrams and Thermochemistry*, 1991, **15**, 317-425.
52. C. L. Ozturk K, Lui Z., *Journal of Alloys and Compounds*, 2002, **340**, 199–206.
53. C. Qiu, G. B. Olson, S. M. Opalka and D. L. Anton, *Journal of phase equilibria and diffusion*, 2004, **25**, 520-527.
54. R. O. Outotec, *HSC version 6.12*, Rauhalanpuisto 9, 02230 Espoo, Finland, 1974 – 2007.
55. I. Barin, O. Knacke and O. Kubaschewski, *Thermochemical properties of inorganic substances: supplement*, Springer Science & Business Media, 2013.
56. L. B. Pankratz, J. M. Stuve and N. A. Gokcen, *Thermodynamic data for mineral technology*, 1984.
57. I. Barin, O.Knacke and Kubaschewski, *Thermochemical properties of inorganic substances*, Springer Berlin Heidelberg edn., 1977.
58. Q.-D. Wang, X.-J. Wang, Z.-W. Liu and G.-J. Kang, *Chemical Physics Letters*, 2014, **616-617**, 109-114.
59. E. Veleckis, *Journal of the Less Common Metals*, 1981, **80**, 241-255.
60. C. M. Criss and J. W. Cobble, *Journal of the American Chemical Society*, 1964, **86**, 5390-5393.
61. USGS, https://minerals.usgs.gov.
62. P. J. Spencer, A. D. Pelton, Y.-B. Kang, P. Chartrand and C. D. Fuerst, *Thermodynamic assessment of the Ca–Zn, Sr–Zn, Y–Zn and Ce–Zn systems*, 2008.
63. M. Ohno, A. Kozlov, R. Arróyave, Z. K. Liu and R. Schmid-Fetzer, *Thermodynamic modeling of the Ca–Sn system based on finite temperature quantities from first-principles and experiment*, 2006.
64. M. Notin, J. Mejbar, A. Bouhajib, J. Charles and J. Hertz, *Journal of Alloys and Compounds*, 1995, **220**, 62-75.
65. S. CHIBOUB, *Etude thermodynamique d'alliages binaires a base de calcium, rapport de Magister en Physique* 2009.
66. P. J. Spencer, A. D. Pelton, Y.-B. Kang, P. Chartrand and C. D. Fuerst, *Calphad*, 2008, **32**, 423-431.
67. M. Heyrman and P. Chartrand, *Journal of Phase Equilibria and Diffusion*, 2006, **27**, 220-230.

68. M. Hillert and W. Xizhen, *Calphad*, 1989, **13**, 267-271.
69. D. A. Sheppard, C. Corgnale, B. Hardy, T. Motyka, R. Zidan, M. Paskevicius and C. E. Buckley, *RSC Advances*, 2014, **4**, 26552-26562.
70. L. Wöhler and F. Müller, *Zeitschrift für anorganische und allgemeine Chemie*, 1921, **120**, 49-70.
71. P. Manfrinetti, M. Fornasini and A. Palenzona, *Intermetallics*, 2000, **8**, 223-228.
72. M. Armbruster, M. Wörle, F. Krumeich and R. Nesper, *Zeitschrift für anorganische und allgemeine Chemie*, 2009, **635**, 1758-1766.
73. H. Wu, W. Zhou, T. J. Udovic, J. J. Rush and T. Yildirim, *Chemical Physics Letters*, 2008, **460**, 432-437.
74. A. D. Bulanov, O. Troshin and V. V. Balabanov, *Synthesis of High-Purity Calcium Hydride*, 2004.
75. W. C. Johnson, M. F. Stubbs, A. E. Sidwell and A. Pechukas, *Journal of the American Chemical Society*, 1939, **61**, 318-329.
76. S. Lin, Y. Wang and Y. Suzuki, *Energy & Fuels*, 2009, **23**, 2855-2861.
77. M. J. Styles, W. W. Sun, D. R. East, J. A. Kimpton, M. A. Gibson and C. R. Hutchinson, *Acta Materialia*, 2016, **117**, 170-187.
78. R. Nedumkandathil, D. E. Benson, J. Grins, K. Spektor and U. Häussermann, *Journal of Solid State Chemistry*, 2015, **222**, 18-24.
79. M. Meggouh, D. Grant and G. Walker, *The Journal of Physical Chemistry C*, 2011, **115**, 22054-22061.
80. N. Ohba, M. Aoki, T. Noritake, K. Miwa and S.-i. Towata, *Physical Review B*, 2005, **72**, 075104.
81. H. Wu, W. Zhou, T. J. Udovic, J. J. Rush and T. Yildirim, *Physical Review B*, 2006, **74**, 224101.
82. H. Wu, W. Zhou, T. J. Udovic, J. J. Rush and T. Yildirim, *Chemical Physics Letters*, 2008, **460**, 432-437.
83. M. R. Swain, P. Filoso, E. S. Grilliot and M. N. Swain, *International Journal of Hydrogen Energy*, 2003, **28**, 229-248.
84. M. Martin, C. Gommel, C. Borkhart and E. Fromm, *Journal of Alloys and Compounds*, 1996, **238**, 193-201.
85. M. Aoki, N. Ohba, T. Noritake and S. Towata, *Applied Physics Letters*, 2004, **85**, 387-388.
86. E. Y. Anikina and V. N. Verbetsky, *Journal of Thermal Analysis and Calorimetry*, 2014, **118**, 801-805.
87. B. J. H. R. Zidan, C. Corgnale, J. A. Teprovich and B. P. a. T. M. D. A. Knight, *Low-Cost Metal Hydride Thermal Energy Storage System for Concentrating Solar Power Systems Report*, 2018.
88. P. A. Ward, J. A. Teprovich, Y. Liu, J. He and R. Zidan, *Journal of Alloys and Compounds*, 2018, **735**, 2611-2615.
89. *Germany Pat.,* 1954, DE944487C.
90. L. Ji, Q. Liu and Z. Liu, *Industrial & Engineering Chemistry Research*, 2014, **53**, 2537-2543.
91. S. Konar, J. Nylén, G. Svensson, D. Bernin, M. Edén, U. Ruschewitz and U. Häussermann, *Journal of Solid State Chemistry*, 2016, **239**, 204-213.
92. *United State of America Pat.,* 1937, 2,082,134,.
93. J.-C. Crivello, B. Dam, R. Denys, M. Dornheim, D. Grant, J. Huot, T. R. Jensen, P. De Jongh, M. Latroche and C. Milanese, *Applied Physics A*, 2016, **122**, 97.
94. P. De Rango, P. Marty and D. Fruchart, *Applied Physics A*, 2016, **122**, 126.
95. F. Islam and M. Medraj, presented in part at the CSME 2004 Forum 92, 2004.
96. R. C. DOMAN, J. B. BARR, R. N. McNALLY and A. M. ALPER, *Journal of the American Ceramic Society*, 1963, **46**, 313-316.
97. A. Khandelwal, F. Agresti, G. Capurso, S. L. Russo, A. Maddalena, S. Gialanella and G. Principi, *international journal of hydrogen energy*, 2010, **35**, 3565-3571.
98. A. Palenzona, P. Manfrinetti and M. Fornasini, *Journal of alloys and compounds*, 2000, **312**, 165-171.
99. J. Wang, P. Chartrand and I.-H. Jung, *Calphad*, 2015, **50**, 68-81.

100. SGTE, http://www.crct.polymtl.ca.
101. C. W. Bale, P. Chartrand, S. Degterov, G. Eriksson, K. Hack, R. B. Mahfoud, J. Melançon, A. Pelton and S. Petersen, *Calphad*, 2002, **26**, 189-228.